SPATIAL TRANSCRIPTOMIC PROFILING OF ADVANCED OVARIAN CLEAR CELL CARCINOMA REVEALS INTRA-TUMOR HETEROGENEITY IN EPITHELIAL-MESENCHYMAL GRADIENT

Thang Truong Le[1,2*], Duncan Yi-Te Wang[2*], Ko-Chen Chen[2], Sebastian Rui-Gu Yan[2], Pei-Yu Chu[3], Tuan Zea Tan[4], Yi-Chia Chiu[2], Jia-Yuh Sheu[5], Chen-Hao Huang[6], Jieru Ye[2], Ya-Ting Tai[2,7], Hsueh-Fen Juan[6,8], Feng-Chiao Tsai[3], Wei-Chou Lin[9], Lin-Hung Wei[6,10] and Ruby Yun-Ju Huang[1,2,8,11,12]

[1] Smart Medicine and Health Informatics Program, International College, National Taiwan University, Taipei, Taiwan

[2] School of Medicine, College of Medicine, National Taiwan University, Taipei, Taiwan

[3] Graduate Institute of Pharmacology, College of Medicine, National Taiwan University, Taipei, Taiwan

[4] Cancer Science Institute of Singapore, National University of Singapore, Center for Translational Medicine, Singapore 117599

[5] Department of Urology, National Taiwan University Hospital, Taipei, Taiwan

[6] Graduate Institute of Biomedical Electronics and Bioinformatics, National Taiwan University, Taipei 106, Taiwan

[7] Department of Obstetrics & Gynecology, National Taiwan University Hospital, Taipei, Taiwan

[8] Center for Computational and Systems Biology, National Taiwan University, Taipei 106, Taiwan

[9] Department of Pathology, National Taiwan University Hospital, Taipei, Taiwan

[10] Department of Obstetrics & Gynecology, College of Medicine, National Taiwan University, Taipei, Taiwan

[11] Graduate Institute of Oncology, College of Medicine, National Taiwan University, Taipei, Taiwan

[12] Department of Obstetrics & Gynaecology, Yong Loo Lin School of Medicine, National University of Singapore, Singapore 119077

* Equal contributions; Corresponding Author: Professor Ruby Yun-Ju Huang

Affiliations: School of Medicine, College of Medicine, National Taiwan University

Address: No. 1, Ren-Ai Road Section I, Taipei, 10051, Taiwan

Tel: +886-2312-3456 ext 88399; E-mail: rubyhuang@ntu.edu.tw

Abstract

Intratumoral heterogeneity is intrinsically comprised of molecular alterations of tumor cells and extrinsically from interconnections with microenvironments. This study explores the spatial heterogeneity of ovarian clear cell carcinoma (OCCC), a rare cancer with significance to East Asian women. We profiled 21 tumors from matched ovarian and metastatic sites with spatial transcriptomic (ST) platforms including GeoMx and Visium CytAssist. Three subclusters of OCCC tumor cells enriched in oxidative phosphorylation, epithelial-mesenchymal transition, and inflammation pathways were identified with preferential geospatial localizations in tumor centers and invasive margins/tumor-stromal interfaces. These ST subclusters correlated with epithelial-mesenchymal gradients and prognostic features in larger cohorts. Single-cell ST in CosMx identified 9 cancer cell populations with organ-specific tropism. Trajectory analysis indicated a NEAT1-high subclone having founder characteristics, progressively dominating the metastatic niche, displaying mesenchymal traits. This founder feature correlated with clinical outcomes in PanCancer datasets. Our findings highlight the adaptive and context-specific interactions between cancer cells and microenvironments within spatial complexities.

Introduction

Intra-tumor heterogeneity (ITH) reflects the presence of genetically- and molecularly-diverse tumor cells coexisting within a complex tumor microenvironment (TME), which also contains immune and stromal cells in varying compositions[1,2]. The interaction between tumor cells and non-tumor cells is driven by a complex and dynamic network of signalings via intercellular communications. This complexity is caused by the intrinsic presence of diverse clones of tumor cells harboring alterations at the multi-omics level. The clonal evolution of these multi-omics alterations results into multiple spatial and temporal patterns, in which the subclones acquire distinct alterations in the same gene, protein complex, or signal transduction pathways[3-9], and the resident non-tumor cells within the TME are conventionally distinguished by cell-type-specific markers at the cell surface. Therefore, the elucidation of the intercellular connections between tumor cells and the TME components is heavily dependent on how well these players in the field are deconvoluted.

The degree of ITH complexity has been further elucidated with advanced technological platforms such as CITE-seq, Abseq, and Slide-seq. CITE-seq combines single-cell RNA sequencing with protein marker detection, allowing for simultaneous measurement of transcriptomes and surface proteins, thus offering deeper cellular characterization[10]. Abseq similarly enables the profiling of proteins and RNA at a single-cell level using DNA-barcoded antibodies, providing high-dimensional phenotypic data[11]. Slide-seq, on the other hand, spatially maps RNA transcripts at near-single-cell resolution, preserving spatial information while maintaining transcriptomic detail[12]. However, despite these advances, single-cell sequencing methods still lack spatial context, complicating the understanding of neighborhood effects within ITH.

Therefore, the advancement of spatially-resolved technologies[13-15] allows researchers to decipher ITH while preserving geospatial information, improving the resolution of complexity within tumors to a greater extent. In the context of high-dimensional -omics, "geospatial" is defined as that which involves analyzing and visualizing expression data at specific tissue locations to understand spatial structures and cell interactions in the local tissue microenvironment. The preservation and addition of geospatial information in the analysis of ITH could potentially unravel the complexities presented by the diverse internal environment of carcinomas and their interactions with the local microenvironment. Spatial transcriptomics is an emerging field that preserves spatial information of molecular data, addressing the limitations of single-cell technologies[16]. The field has rapidly developed various spatial multi-omics technologies, each with different strengths in sensitivity, dynamic range, and cell segmentation and providing insights into the interactions at different cell locations[17,18]. Spatial transcriptomics has been applied to cancer research, including initiation, progression, and metastasis studies[16], tumor heterogeneity and microenvironment[19], and biomarker identification[17]. The integration of multiple omics data with spatial context has revealed much about disease mechanisms, spatial heterogeneity, and tumor immunology[20,21]. Despite ongoing technical challenges[17], the field continues to evolve with improvements in throughput, resolution, and accuracy[20]. Spatial transcriptomics is poised to become a powerful tool for unraveling tumor biology and advancing precision medicine in oncology[16].

Several studies have utilized spatial transcriptomics to dissect ITH within TME across various caner types[22-15]. Spatial profiling is particularly important for cancer types harboring high levels of heterogeneity and has been very useful in identifying potential therapeutic vulnerabilities for cancer types with unmet needs. Ovarian clear cell carcinoma (OCCC) is one such cancer subtype, having tremendously complex molecular features with limited therapeutic options[26]. Chemoresistance is particularly prominent in OCCC[21,22], resulting into comparatively poorer prognosis when compared to other subtypes, such as

high-grade serous ovarian carcinoma (HGSC)[23-25]. The distinct molecular and genetic heterogeneity in OCCC tumors[26,27] is known to involve mechanisms such as epithelial-mesenchymal transition (EMT)[26], cysteine-dependent metabolic changes[28], hypoxia[27,29,30], and interactions between the tumor and its immune microenvironment[20,21,29-33]. However, detailed and in-depth profiling of ITH in OCCC has not been fully addressed at high spatial resolutions.

Accumulating evidence is pointing to the notion that certain spatially-resolved neighborhood features have impact on therapeutic responses and disease outcomes[31]. Herein, we report the workflow of a comprehensive cross-platform spatial transcriptomic profiling study focusing on paired-tumor samples from the primary versus multiple metastatic sites in advanced-stage OCCC patients. Our results showed a spatially-correlated gradient in the distribution of epithelial- and mesenchymal-like features. This gradient exhibited differential functional and cell-type enrichments between subclones of tumor cells from both the primary and metastatic sites, suggesting clonal diversity during tumor progression. We further identified unique niches at the invasion sites within both the primary and metastatic tumors where plausible founder clones reside suggesting a neighborhood effect during the metastasis and adaptation process of OCCC cells in different microenvironments. Our study provides further knowledge of the mechanisms and molecular events contributing to the aggressiveness of OCCC and could be provide the keys to developing novel treatments.

RESULTS

Spatial profiling using the GeoMx Cancer Transcriptome Atlas (CTA) panel was performed in 207 transcriptomic areas of illumination (AOI) from 13 formalin-fixed paraffin-embedded (FFPE) sections of paired primary and metastatic tumors from 2 advanced stage OCCC patients (Patient 1 and Patient 2). These OCCC AOIs were annotated and collected based on their organ sites, geospatial locations within the tumor or the surrounding microenvironment, and segmentation subgroups (Fig. 1a; S. Table 1-2). Unsupervised hierarchical clustering of these AOIs showed 2 clades and 4 subclusters.

The "C1" clade featured Gene Ontology biological process (GO: BP) terms of chemotaxis- (*CXCL10*, *CXCL14*, *S100A8*, etc.), cell adhesion- (*CD24*, *CDH1*, *EPCAM*, etc.), cell migration- (*CD47*, *ITGB3*, *LGALS3*, etc.), and angiogenesis-related (*EFNA1*, *HIF1A*, *ITGB8*, etc.) (Fig. 1b; S. Table 3). This clade was divided into two subclusters, labeled "C1a" and "C1b". Subcluster C1a consisted of 83.9% PanCK-pos and 16.1% PanCK-neg/CD45-pos AOIs, enriched in oxidative phosphorylation (OXPHOS)-related hallmark (Fig. 1c, S. Fig. 1a, S. Table 4). Subcluster C1b consisted of 100% PanCK-pos AOIs, enriched in TNF-α/NF-κB signaling- and apoptosis-related hallmarks (Fig. 1d, S. Fig. 1b, S. Table 4).

The other clade featured GO: BP terms of immune response- (*C3*, *IL7R*, *TNFAIP3*, etc.) and antigen processing/presentation-related (*CD74*, *HLA-DRB3*, *THBS1*, etc.) (Fig. 1b, S. Table 3). This clade was divided into the "C2" and "TME" ("tumor microenvironment") subclusters. Subcluster C2 consisted of 95% PanCK-pos and 5% PanCK-neg/CD45-pos AOIs, enriched in DNA repair-related and E2F targets-related hallmarks (Fig. 1e, S. Fig. 1c, S. Table 4). Subcluster TME, which was enriched in allograft rejection-, IFN-γ response-, KRAS signaling-, epithelial-mesenchymal transition- (EMT), and complement-related hallmarks, consisted of 100% PanCK-neg/CD45-pos AOIs, indicating this subgroup was composed entirely of cells in TME (Fig. 1f, S. Fig. 1d, S. Table 4).

Preferential subcluster distribution of PanCK-pos tumor cells among organ sites and geospatial locations

PanCK-pos AOIs (which indicated tumor cells) were distributed into subclusters C1a, C1b, and C2 (S. Table 4). OCCC tumor cells from ovarian primary sites were mainly distributed into C1a and C1b; those from recurrent sites (breast and neck lymph nodes from Patient 2) were distributed only into C2 (Fig. 1g; *Chi*-square test, P = 2.91E-4). Based on organ sites, the PanCK-pos AOIs showed preferential distributions of subcluster patterns for certain organ sites (Fig. 1h; *Chi*-square test, P = 7.86E-17) (S. Table 4). Tumor cells from the ovaries and colon showed with low frequency in C2, while those from bladder rarely showed in C1a. Tumor cells from the lymph nodes were exclusively clustered in C1a, and those from the omentum only showed in C1a and C1b. Tumor cells from the uterus and peritoneum both distributed in C1b and C2; however, those from the uterus showed with higher frequency in C1b, whereas those from the peritoneum showed with higher frequency in C2 (Fig. 1h).

PanCK-pos AOIs also showed preferential distribution patterns for certain geospatial locations (Fig. 1i; *Chi*-square test, P = 3.19E-11; S. Table 2 and 5) (S. Fig. 1e, f). About 70% of the PanCK-pos AOIs in C1a were in the tumor center, while those in C1b and C2 were mainly in the tumor periphery, stroma (invasion), and necrotic/hemorrhagic area. Based on geospatial locations, 65.5% of the PanCK-pos AOIs from the tumor center were clustered into C1a and 68.4% of the PanCK-pos AOIs from the tumor periphery were clustered into C1b; in contrast, over 50% of the tumor cells in the stroma and necrotic/hemorrhagic areas were clustered into C2 (Fig. 1i) (S. Fig. 1e, f) (S. Table 5). By projecting the annotation back into a two-dimensional UMAP space, we further confirmed distinct compositions of AOI segmentations and geospatial annotations between subclusters (Fig. 1j-m), reflecting the close relationships between the subclusters and geospatial annotations for the PanCK-pos AOIs.

GSVA score reflected the functional gradients of PanCK-pos GeoMx tumor subclusters

Gene set variation analysis (GSVA) was performed to assess the enrichment scores of different hallmarks for each AOI (Fig. 2a-h). The GSVA results suggested that EMT-, cell proliferation-, and cell metabolism-related hallmarks were differentially enriched between the PanCK-pos AOIs (S. Fig. 2a; outlined with black rectangles) (S. Table 6). The interconnectedness of the hallmarks for the tumor cells revealed links between cellular functions (S. Fig. 2b; Spearman's correlation). Furthermore, we found differential hallmark gradients between geospatial locations and the tumor cell subclusters (S. Fig. 2c-i).

Significant gradients were observed between the geospatial tumor cell subgroups in the OXPHOS-, adipogenesis-, MYC targeting-, EMT-, and mitotic spindle-related hallmarks. Interestingly, when comparing the subclusters, similar patterns were also observed in the abovementioned hallmarks except for MYC-targeting; marked gradients in mTORC1 signaling-, ROS-, and DNA repair-related pathways were revealed using this comparison. Meanwhile, Spearman's correlation analyses showed interweaving links between cellular functions, featuring EMT-, inflammation-, OXPHOS-, and DNA repair-related hallmarks. Differential correlation patterns between EMT-related hallmarks and others, including glycolysis, coagulation, and MTORC1 signaling, were also noted. (Fig. 2i-k; S. Fig. 2j-m). These highly correlated hallmark gradients collectively expanded the characteristics found in the aforementioned GSVA results (Fig. 1c-e), supporting the unique gradient observed in the GSVA enrichment score (S. Fig. 2c-i). When comparing tumor cells from primary ovarian and metastatic sites, the patterns of differences between several hallmarks were similar (Fig.2l-q).

The differential gradients and unique distribution patterns of the GSVA hallmark enrichment scores illustrated the characteristics of the tumor cell heterogeneity and tumor cell geospatial locations in detail. It also revealed the interconnectedness between EMT, cell metabolism, cell proliferation, cellular response to inner and outer environmental signals.

Generic EMT scores revealed geospatial and inter-subcluster EM gradients

To further assess the extent of epithelial-mesenchymal transition, we computed a generic EMT score as per Tan *et al.* for each AOI, wherein higher scores indicated more "mesenchymal" characteristics while lower scores were more "epithelial"[34]. The PanCK-neg TME cells were more mesenchymal when compared with the PanCK-pos C1 and C2 tumor cells ($P < 0.0001$) (Fig. 3a). In terms of tumor cell subclusters, those in C1 were more epithelial compared to those in C2 ($P < 0.0001$) (Fig. 3b, c). In terms of their geospatial locations, the tumor cells in ovarian primary sites were more epithelial than those collected from the metastatic and recurrent sites ($P < 0.0001$); metastatic tumor cells were more mesenchymal than cells from the primary and recurrent sites ($P < 0.0001$); and comparing recurrent tumor cells to the other two types showed no statistical significance between them ($P = 0.8397$) (Fig. 3d). Among the metastatic sites, statistically significant EMT scores were only found in tumor cells from the lymph nodes, bladder, and peritoneum: the first was more epithelial ($P = 0.0125$), whereas the latter two were more mesenchymal ($P = 0.0233$ and 0.0002, respectively) (S. Fig. 3a). Metastatic tumor cells within C1b ($P < 0.0001$) and C2 ($P = 0.0001$) were more mesenchymal when compared to the rest of the tumor cells, while those in C1a showed no significant difference either way (Fig. 3e-g).

Albeit with inter-patient differences, TME cells had higher EMT scores (i.e., were more mesenchymal) compared to tumor cells for both patients, as were the tumor cells in C2 when compared to those in C1 (Fig. 3h) (S. Fig. 3b-d). Differences in tumor progression were observed in Patient 2's ovarian ($P = 0.0011$) and recurrent ($P = 0.0058$) tumor cells; however the difference observed in her metastatic tumor cells was not statistically significant ($P = 0.0924$) (S. Fig. 3e, f).

With regards to the correlation between geospatial distribution patterns and EM (epithelial-mesenchymal) gradients, we found that tumor cells in the tumor centers were more epithelial ($P = 0.0002$),

while those in necrotic/hemorrhagic areas were more mesenchymal (P = 0.0020) (Fig. 3i); patient-wise analyses further indicated that tumor cells in tumor centers were more epithelial (P = 0.0021 and P = 0.0026 for Patients 1 and 2, respectively), whereas those invading into the surrounding stroma were more mesenchymal (P = 0.0130 and P < 0.0001, respectively) (Fig. 3j, k). Combined with GSVA results, our results showed that EM gradients correlated with functional changes across tumor cell subclusters, tumor progression, and geospatial locations.

TME exhibited "neighborhood-dependent" EMT scores and biological functional differences

We next explored the relationship between the EMT scores of cells in the TME and adjacent tumor cells within the same ROIs. Only 31 of the collected ROIs were TME / tumor-cell-paired, and the adjacent tumor cells were all from the C1 clade (9 from the C1a subcluster and 22 from C1b) (S. Table 7). Compared to TME cells adjacent to C1a tumor cells (TME_C1a), those paired with C1b tumor cells (TME_C1b) showed more mesenchymal scores (P = 0.0102) (Fig. 4a). Moreover, there were geospatial preferential distribution patterns between TME_C1a and TME_C1b, as well as preferential adjacent tumor cell patterns between TMEs within the tumor nest (TME_Nest) and at the tumor-stroma interface (TME_TSI) (Fisher's exact test, P = 0.0166) (Fig. 4b, c). The EMT scores suggested that TME_TSI cells were more mesenchymal than those in the TME_Nest (P < 0.0001) (Fig. 4d). When stratified by organ, similar patterns were observed in the TMEs of the ovaries (P = 0.0012) (S. Fig. 4a) and the colon (P = 0.0303) (S. Fig. 4b); when stratified by adjacent tumor cell subcluster, the same trend was also observed in C1b (P = 0.0104) (S. Fig. 4c).

GSVA results (Fig. 4e-i) suggested that these tumor-cell-paired TMEs with different geospatial relationships (aka "neighborhoods") were functionally distinct from each other (S. Fig. 4d-g). Enrichment of TGF-β signaling-, mTORC1 signaling-, glycolysis-, and apical junction-related hallmarks, and

sprouting angiogenesis-related pathways all were noted in TME_Nest; whereas enrichment of the allograft rejection-related hallmark was noted in TME_TSI (S. Fig. 4d). By contrast, enrichment of the myogenesis-related hallmark was noted in TME_C1a, while enrichment of the IL-6/JAK/STAT3- and allograft rejection-related hallmarks were noted in TME_C1b (S. Fig. 4e-g).

Differentially expressed genes (DEG) (S. Table 8) and GO: BP analyses (S. Table 9) further revealed enriched expressions in several different pathways. In TME_Nest, these included ameboidal-type cell migration (*WNT7A*, *LAMA5*, *STC1*, *GPX1*, *S100A9*); cell adhesion mediated by integrin (*MUC1*, *ITGA1*, *ITGB8*, *ITGA3*, *EFNA1*, *DPP4*); cell-substrate adhesion (*CD34*, *NID2*, *RHOA*), pyruvate metabolic process (*LDHB*, *ALDOA*, *GPI*, *APP*, *PKM*), and monosaccharide metabolic process pathways (*IGFBP3*, *SLC2A1*, *RBP4*). In TME_TSI, it showed enriched expression of the humoral immune response (*POU2AF1*, *LYZ*, *CXCL13*), complement activation (*C1S*, *C1R*, *C3*), mononuclear cell differentiation (*JUN*, *JUNB*, *FOS*, *CD79A*, *PRDM1*), and regulation of angiogenesis pathways (*SFRP2*, *CXCR4*).

Focusing on adjacent tumor cell subgroups, TME_C1a showed enriched expressions in MAPK cascade (*MAP3K5*, *GADD45A*) and cell projection organization (*SPP1*, *EFNA1*, *ITGA3*) pathways, accompanied by pathway enrichment like that of TME_Nest, among others. TME_C1b showed enriched expression, including antigen processing and presentation (*CD74*, *HLA-DRA*, *HLA-DRB3*, *HLA-DRB4*, *HLA-DQA1*), T cell activation (*IL7R*, *PTPRC*), and cytokine-mediated signaling pathway (*TNFAIP3*, *NFKBIA*, *CXCL13*) (S. Fig. 4h, i) (S. Table 8 and 9).

These results suggested that adjacent tumor cell subclusters and their geospatial relationships with tumor cells may collectively change the transcriptomic programs of TME. The heterogeneity of the tumor cell subclusters and their adjacent TMEs shared similar molecular features in EMT score and functional pathways and formed unique neighborhoods.

Enrichment of GeoMx tumor cell subcluster signatures across ovarian cancer gene expression molecular subtypes (OC_GEMS)

To validate whether the GeoMx tumor cell subclusters would show enrichments among known OC_GEMS with different known EMT statuses or with histological characteristics, we generated tumor cells subcluster signatures (S. Fig. 4j, S. Table 10 and 11) and projected them onto the OC transcriptomic microarray database of the Cancer Science Institute Singapore (aka "CSIOVDB"), which consists of 3,431 OC bulk expression profiles[17]. Comparisons between epithelial-like (EpiCC) and mesenchymal-like (MesCC) subtypes[11] showed that the signature of C1a tumor cells (GeoMx_C1a_Feature) was more enriched in EpiCC ($P < 0.0001$) (Fig. 4j), while those of C1b (GeoMx_C1b_Feature) and C2 tumor cells (GeoMx_C2_Feature) were more enriched in MesCC ($P = 0.0056$ and $P < 0.0001$, respectively) (Fig. 4k, l). Analyses on OC with different molecular subtypes[30] further linked GeoMx_C2_Feature with one other known MesCC subtype with poorer clinical prognosis (S. Fig. 4k). Stratification by histological OC subtypes[35] revealed enriched expression of GeoMx_C1a_Feature in OCCC when compared to other OC subtypes (Fig. 4m-o). Therefore, the data supported that GeoMx_C1a_Feature contains OCCC-specific signatures with comparatively low EMT. In contrast, GeoMx_C1b_Feature and GeoMx_C2_Feature may contain shared molecular program changes involving EMT or in response to microenvironmental stimuli across different OC histological and molecular subtypes.

Comparison between OCCC and HGSC

With GeoMx_C1a_Feature being more OCCC-specific in mind, we then included 175 QC-passed AOIs (166 PanCK-pos AOIs and 9 PanCK-neg/CD45-pos AOIs) from 1 patient (Patient 3) with advanced high-grade serous carcinoma (HGSC) together with the OCCC AOIs in the clustering analysis (Fig 1a). The co-clustered AOIs were subdivided into 2 clades (HGSC-C1 and HGSC-C2) and 3 subclusters

(HGSC-C1a, HGSC-C1b, and HGSC-C2) (S. Fig. 4l). HGSC-C1a was comprised of 93.75% PanCK-pos and 6.25% PanCK-neg/CD45-pos AOIs; HGSC-C1b was purely comprised of PanCK-pos AOIs; and HGSC-C2 was comprised of 43.52% PanCK-pos and 56.48% PanCK-neg/CD45-pos AOIs (S. Table 12). For OCCC, almost all the PanCK-pos AOIs kept the same subgroup annotations as in the prior analysis; for HGSC, all of the PanCK-pos AOIs were exclusively clustered in the HGSC-C1 clade (HGSC-C1a and HGSC-C1b subgroups), suggesting the stability of the previous clustering structure (S. Table 12).

GSEA results revealed that OCCC tumor cells possessed distinctively different molecular traits when compared with those of HGSC even within the same clade/subcluster (S. Fig. 4m). Within their C1 clades, OCCC tumor cells were more enriched in OXPHOS, EMT, apoptosis, hypoxia, inflammatory response, adipogenesis, and glycolysis, while HGSC tumor cells were more enriched in mitotic spindle and E2F targets. Within their C1a subclusters, OCCC tumor cells were more enriched in OXPHOS, hypoxia, glycolysis, and mTORC1 signaling, while HGSC tumor cells were more enriched in Wnt/beta-catenin pathway; and within their C1b subclustesr, OCCC tumor cells were more enriched in EMT, TGF-beta signaling, coagulation, and myogenesis, while HGSC tumor cells were more enriched in E2F targets and MYC targets V1 (S. Fig. 4m). An assessment of the generic EMT scores of both the OCCC and HGSC tumor cells from C1 suggested that the HGSC-C1 tumor cells were more mesenchymal than the C1 OCCC cells ($P < 0.0001$), and the same trend was observed when the tumor cells were stratified into C1a ($P\ p = 0.0025$) and C1b ($P = 0.0073$) (S. Fig. 4n).

Cell signatures from three published datasets[36-38] were used to perform cell-type superimpositions on both OCCC and HGSC tumor cells to explore and depict the unique enrichment of cell types in OCCC tumor cells (S. Table 13 and 14). These reference signatures derived from one HGSC-, one endometrium-, and one endometriosis-related scRNA-seq data were chosen to assess the most dominant cell types for each PanCK-pos AOI, since OCCC is often linked with endometriosis and may originate from endometrial

cells undergoing malignant transformation. Using HGSC reference signatures from Vázquez-García *et al.*[37], enrichments in the cancer.cell.6 (hypoxia) and ciliated.cell.1 (microtubule-based movement) signatures were revealed in C1a OCCC tumor cells, and cancer.cell.4 (TGF-β signaling) in C1b OCCC tumor cells (Fig. 4p). With endometrium reference signatures from Garcia-Alonso *et al.*[38], enrichment in the lumenal_2 (response to xenobiotic response) signature was shown in C1b OCCC tumor cells, while low enrichment in SOX9_prolif (DNA replication) was noted in the same cells (Fig. 4q). With endometriosis reference signatures from Fonseca *et al.*[36], enrichments in glandular.secretory (regulation of apoptotic pathway) and IHH+/SPDEF+ (OXPHOS-related) were found in C1a OCCC tumor cells and in ciliated (microtubule-based movement) were found in C1b OCCC tumor cells (Fig. 4r). Taken altogether, these results validated the hypothesis that features such as OXPHOS were unique for OCCC and that changes in functional enrichment during tumor progression may differ between OCCC and HGSC.

Visium spatial transcriptomic analysis deconvoluted the landscape of primary and metastatic OCCC

To confirm the abovementioned findings were not due to selection bias of the ROIs, we then performed array-based Visium whole transcriptomic spatial analysis on one ovarian primary tumor sample and one colonic metastatic sample from Patient 1 (Fig. 5a). By projecting Visium UMAP unsupervised clustering results back onto the tissue images, we found that different subclusters of cells were more regionally-distributed than sporadically-intermixed with each other, for both ovarian and colonic samples. Cell type deconvolution analyses then revealed differential cell type compositions across the subclusters (Fig. 5b). Accordingly, the tumor bulk, tumor-stroma interface, and stroma regions showed a consistent decreasing trend in the fraction of cancer cells within each cluster. Interestingly, the enrichment of several hallmarks, including OXPHOS-, adipogenesis-, hypoxia-, glycolysis-, inflammation-, and TNF-α/NF-κB

signaling-related pathways, depicted the clusters well and may imply inter-cluster functional differences (Fig. 5c). Inverse expression patterns, such as the negative correlation between OXPHOS and TNF-α/NF-κB signaling, were observed and were consistent with the previous GeoMx GSVA results (Fig. 2) (S. Fig. 2a-m).

We next assessed the enrichment of GeoMx subcluster features and EMT score for these two Visium objects (Fig. 5d) and found that GeoMx subcluster features more finely delineated between the tumor bulk, tumor-stroma interface, and stroma. Focusing on the tumor cell subclusters near the tumor-stroma interface for both samples, we found that tumor cells within the tumor bulk were generally more enriched in OXPHOS- and adipogenesis-related pathways, while those located at the interface or invaded into the stroma were generally more enriched in hypoxia-, inflammation-, and TNF-α/NF-κB signaling-related pathways. Moreover, when compared to the tumor bulk, the latter were less enriched in GeoMx_C1a_Feature; more enriched in GeoMx_C1b_Feature, GeoMx_C2_Feature, and GeoMx_TME_Feature; and more mesenchymal, which further validated the previous GeoMx geospatial analysis results (Figs. 2 and 3i-k). The correlation between the EMT scores with the patterns of the GeoMx cluster features could also be observed from the projection in Visium data from OCCC tumor pairs of Patient 2, two OCCC tumors from a Japanese cohort[32], one endometrial adenocarcinoma_ovary, one invasive lobular carcinoma_breast, and one glioblastoma_brain (S. Fig. 5). The spatial patterns of Mes scores, GeoMx_C2_Feature, and GeoMx_TME_Feature showed high degree of concordance, confirming that these features might be cancer-agnostic and could help identify specific neighborhoods that would exhibit EMT across various cancer types.

Metabolic shifts and *in ovo* tumor biology in an EMT gradient model of OCCC cells

The observation of gradient enrichment for EMT and OXPHOS across different tumor subclusters (Fig. 2a, b and S. Fig. 2c) raised the possibility that their correlation could manifest in cancer cell phenotypes and influence tumor behavior. To verify this, we utilized OCCC cell lines as a model of EMT gradients, investigating not only their bioenergetic profiles through *in vitro* real-time cell-based energy metabolism assays but also tumor growth and dissemination using an *in vivo* chorioallantoic membrane (CAM) model in chick embryos, a well-validated system for studying cancer angiogenesis and metastasis [39,40], as is the case of ovarian cancer[41,42].

JHOC9 and RMG2, both OCCC cell lines with generic EMT scores[34] of less than zero, were identified as EpiCC prototypes[26]. To reproduce EMT gradients, the well-studied EMT suppressor, GRHL2 [43-46], was further knocked down in both JHOC9 and RMG2, shifting them toward less-epithelial states (S. Fig. 5a-d). Using luciferase knockdown as a control, we established a small-scale EMT spectrum comprising four stable clones: JHOC9_shLuc, JHOC9_sh*GRHL2*, RMG2_shLuc, RMG2_sh*GRHL2* with EMT scores of −0.42, −0.41, −0.15, and −0.12, respectively (Fig. 6a). Morphologically, RMG2_sh*GRHL2* exhibited a more mesenchymal/spindle-shaped appearance relative to RMG2_shLuc, while both JHOC9 clones retained their epithelial traits with adherent and concentrated cellular morphology (S. Fig. 5a), indicating of a less-EpiCC phenotypic gradient.

To delve into the potential association between EMT and cellular metabolism in OCCC, we assessed mitochondrial function and glycolytic capacity using an extracellular flux analyzer, measuring oxygen consumption rates (OCR) and extracellular acidification rates (ECAR). Inherent metabolic heterogeneity was observed between the two cell lines, as OCR readings revealed that JHOC9 cells had intrinsically higher OXPHOS activity, compared to RMG2 (Fig. 6b). Upon being challenged with the mitochondrial uncoupler FCCP, all cell clones responded by maximizing OXPHOS activity (Fig. 6b). Notably, respiratory reserve capacity, which is the additional ATP produced by OXPHOS at maximal

capacity, dropped drastically following *GRHL2* knockdown only in JHOC9 (Fig. 6b). This finding suggests that JHOC9_sh*GRHL2* heavily relies on mitochondrial respiration under standard culture conditions, with limited spare capacity to ramp up OXPHOS when required, and GO analysis supported this deduction (S. Table 15).

However, both *GRHL2* knockdown clones exhibited significantly higher glycolytic reserves (difference between maximal and basal ECARs) compared to their respective luciferase knockdown controls (Fig. 6c). After the addition of oligomycin A, which hampers ATP-linked respiration and prompts cells to shift bioenergetics from OXPHOS to glycolysis, ECAR largely increased in all stable clones. To achieve a comprehensive overview of the metabolic characteristics of the stable clones studied, we plotted basal OCR against basal ECAR (Fig. 6d). The JHOC9 clones were highly energetic with robust OXPHOS and glycolysis, whereas the RMG2 cells were less energetic, requiring less respiratory and glycolytic activity to sustain basic cellular functions. While *GRHL2* knockdown decreased the reliance on glycolysis in OCCC cells, neither JHOC9 nor RMG2 shifted in a compensatory manner towards OXPHOS, as indicated by unchanged basal OCR. The reduction in basal ECAR, combined with enhanced glycolytic reserve, suggests that glycolysis operates less extensively when OCCC cells exhibit a less epithelial phenotype following *GRHL2* knockdown. Taken together, the data indicated that JHOC9 and RMG2 underwent similar metabolic changes in response to EMT despite having different intrinsic levels of bioenergetic demands.

This EMT gradient established by *GRHL2* knockdown also showed a corresponding increase in tumor growth in the CAM model (Fig. 6e), suggesting a potential positive correlation between EMT scores and tumor proliferation. Using Alu-PCR to assess cellular dissemination, there was a gradual increase of overall metastatic potential as OCCC cells transitioned away from the epithelial phenotype (Fig. 6f), despite having no significant correlation between EMT gradients and metastasis to either the liver or lower

LCAM alone. Intriguingly, a similar decreasing trend was noted in basal ECAR (Fig. 6c). In addition, FFPE sections of the CAM tumors were further profiled by using the GeoMx CTA panel (S. Fig 7). Compared to JHOC9_shLuc, JHOC9_sh*GRHL2* showed significant down-regulation of *LCN2* (Fig. 6g), the gene coding for the iron transport and metabolism protein lipocalin-2, suggesting that *in ovo* tumors formed by the partial EMT OCCC cells also had shifts in metabolic gene expressions. LCN2 has been reported to attenuate iron-related oxidative stress and DNA damage in OCCC[47]. The downregulation of *LCN2* in these less-epithelial OCCC cells *in vivo* could render the tumors towards further metabolic challenges leading to DNA damages. Taken together, these findings suggested possible relationships between EMT gradients, metabolic profiles, and tumor behavior in OCCC.

Single-cell spatial transcriptomics analysis revealed organ-specific OCCC cell populations

To comprehensively characterize the cellular landscape of OCCC in-depth, we applied CosMx SMI technology on 144 selected fields of view (FOVs) in tumor samples from the ovarian, peritoneal, and colonic sites of Patient 1 (S. Table 17). Unsupervised hierarchical clustering analysis identified 25 distinct single cell clusters, including 9 cancer cell subtypes (labeled “a” through “i"), 10 immune cell subtypes (B cells, T cells, macrophages, etc.), and 6 stromal cell subtypes (endothelial cells and fibroblasts of various subtypes) (Fig. 7a).

Quantification of cell subtype proportions (Fig. 7b) revealed site-specific differences in cellular composition. Among these FOVs, cancer cells constituted the dominant population (64.32%) in the primary ovarian tumor, whereas in the metastatic peritoneal and colonic tumors, the summed proportions of immune cells (41.03%) and stromal cells (37.50%) outweighed those of the cancer cells, respectively. Moreover, the distribution of prominent cancer cell subtypes varied across the different organ sites. The primary ovarian tumor site displayed a diverse cellular composition, with 8 out of the 9 cancer cell

subtypes (all except cancer h) represented and predominantly characterized by cancer cells a, c, d, and g (17.54%, 28.82%, 24.38%, and 17.63%, respectively). The peritoneal tumor was more commonly associated with cancer cell f (53.91%) and the colonic tumor with cancer cells b and e (48.79% and 35.79%). Similarly, the subtype mixes of immune cells and stromal cells were also different between these three sites (S. Fig. 8a).

Certain cancer cell types showed high exclusivity in the organ sites (S. Table 19). For instance, cancers c, d, g, and i are highly enriched in the ovary (98.70%, 95.43%, 94.96%, and 96.63%, respectively) while cancer b was similarly enriched in the colon (96.27%). Cancer h was exclusive to the peritoneum. Cancer e was mainly found in the colon (86.47%), with a moderate presence in the peritoneum (13.32%) and very low levels in the ovary (0.21%). Similarly, cancer f was predominantly in the peritoneum (74.03%) and notably present in the colon (8.70%) and ovary (17.27%). This suggested that cancer clones with different molecular features might prefer specific microenvironment niches for clonal selection, expansion, and conversion.

DEG analysis uncovered cell type-specific markers and functional signatures (Fig. 7c, S. Table 18). Cancer cell populations exhibited distinct expression patterns, with *VEGFA*, *NDRG1*, *GDF15*, *MECOM*, *UBE2C*, *LEFTY1*, and *EPCAM* being highly expressed. Immune cells showed expected lineage-specific markers (e.g., *C1QA* and *C1QC* for macrophages). Stromal populations were characterized by the expression of extracellular matrix genes, such as *JUN*, *FN1*, *COL1A1*, and *COL1A2*.

Further geospatial analysis of the cancer cell subtypes revealed site-specific variations in tumor-cell distributions and heterogeneity (Fig. 7d, e). Most interestingly, cancer cells of subtype f, though accounting for only a small proportion (3.8%) of the tumor center in the ovary, became more prevalent at ovarian invasion sites (11%) and increased to become the most dominant cell type (56%) in the metastatic site - i.e., the peritoneum. Similarly, cancer cell e only accounted for a minor proportion (11%) of the

invasion/stroma region of the peritoneum but emerged as one of the dominant cell types (35.79%) in the colonic metastasis, indicating the role of the stromal microenvironment in supporting tumour development and progression. These findings spuured our further investigation into the origin of cancer cell lineages in OCCC was crucial.

Geospatial localization of OCCC cancer cell types showed unique trajectory patterns

Unsupervised hierarchical clustering and UMAP visualization revealed nine distinct cancer cell types with varying distributions across anatomical locations in advanced OCCC. The trajectory analysis of all three sites suggested a complex evolutionary landscape in which cancer cells of subtype f could be the founder for the other cancer cell lineages (Fig. 8a). To validate this, we performed trajectory analyses for each organ site. In the ovary (Fig. 8b), the cancer cell f cluster showed the shortest pseudotime path (i.e., the "oldest"), while subtypes c, d, and g had the longest pseudotime paths (i.e., the "youngest"). The latter result indicated that subtypes c, d, and g were terminal states at this primary site, potentially representing fully adapted ovarian tumor cells. Taken together, these results implied that cancer f cells might represent an early founder state from which the other subtypes emerged.

The metastasic peritoneal site showed a shift in cellular composition from the ovarian primary site, with a pronounced enrichment of subtype f and a higher level of enrichment of subtype e (Fig. 7b). The trajectory analysis suggested that the cancer cell f cluster in the peritoneum had a shorter pseudotime path compared to other cells (Fig. 8c). This implied that cancer subtype f in the primary tumor might have evolved into a new state in this metastatic site, possibly representing a peritoneum-specific adaptation.

The metastasic colonic site exhibited a dramatically different shift in composition from the primary site, with cancer b and e cells as the dominant clones (Fig. 7b). The trajectory analysis revealed two pseudotime clusters showing different origins (Fig. 8d). First, cancer b cells appeared to originate from

cancer f, according to the pseudotime path values, whereas cancer e cells did not share a common origin with other cancer cell lineages in the colon. Since cancer e cells also existed in the peritoneum, one possibility is that the cancer e cells in the colonic site were derived from the cancer e cells in the peritoneal site, particularly from the invasion/stroma regions. Trajectory analysis from the peritoneal invasion/stroma regions (Fig S. 8b) and the colonic site lent weight to the hypothesis that it is possible that the cancer e cells in the peritoneal invasion/stroma regions could have originated from either a group cancer f cells with a different origin or a distinct TME from the cancer f cells in the seen colonic site.

Cancer cell f with an intermediate EMT state was the plausible founder clone

To further characterize the potential founder cancer f cells, we evaluated the EM scores of all cancer cells (Fig. 8e). In all three sites, cancer cells a and f consistently exhibited the lowest epithelial scores and the highest mesenchymal scores, indicating a strong mesenchymal phenotype. In contrast, the remaining cell subtypes all showed intermediate values of EM states, suggesting a more mixed or transitional phenotype. We also compared the EM scores according to the geospatial locations, focusing on the tumor center versus the invasion front and surrounding stromal area (Fig. 8f). In the ovary, subtype f cells at the invasion sites exhibited significantly higher mesenchymal scores compared to those in the tumor center ($P < 0.0001$), without significant differences in the epithelial scores. In the peritoneal metastases, subtype f cells at the invasion sites displayed lower epithelial scores ($P < 0.0001$) and higher mesenchymal scores ($P < 0.0001$) compared to subtype e cells. These findings indicated distinct patterns of epithelial and mesenchymal characteristics among different cancer cell clones in different TMEs, which could have implications in tumor progression and metastatic potential.

The nature of cancer f cells was further explored by DEG analysis of subtype-specific signatures of the cancer cell populations (Fig. 8g) (S. Table 20). In particular, the cancer f signature showed notably

high expressions of *JUN*, *LIFR*, *MALAT1*, *NTRK2*, *IL6*, *ZFP36*, *RPS4Y1*, *FOS*, *STAT4, TAGLN, NEAT1, ACKR3, COL1A1, BCL2 and POU5F1*. The trajectory analysis for cancer f across the three organ sites (Figure 8h) confirmed again that the pseudotime distances for cancer f cells in the ovary were the shortest (and therefore the "oldest") while those in the peritoneum and the colon were longer (and were therefore "younger"), which provided insight into the role cancer f cells play in metastasis.

Overall, the data indicated that there might exist a clonal hierarchy among cancer cell subtypes during progression. At the ovarian invasion sites, cancer f cells showed the lowest pseudotime values compared to the rest of the cancer cells (Fig. 7i) and had higher mesenchymal than epithelial scores (S. Fig. 8d). Taken together, these results supported the hypothesis (S. Fig. 8c) that cancer f cells with intermediate EM states were the founder subtype for the other subtype lineages, with a tendency to metastasize from the tumor center to the invasion/stroma region of the ovary, then to the peritoneum, and then finally to the colon.

Microenvironmental interactions of OCCC cancer f cells across primary and metastatic sites

To better understand the community effect of cancer f cells on the TME, we focused on the ligand-receptor interactions between cancer f cells and their neighborhoods in specific geospatial areas (Fig. 9a-c). In the primary ovarian site, cancer f cells consistently interacted with cancer c, d, g, and i cells, as well as NK, dendritic, and T cells from across the tumor center to invasion/stroma sites (Fig. 9d). At the ovarian invasion sites, cancer f cells showed additional interactions with fibroblast b cells, indicating a potential role in promoting invasion and metastasis. Neighborhood analysis (Fig. 9g) further suggested that at the ovarian invasion/stroma sites, cancer f tended to co-localize with other types of cancer cells (a, c, d, g, and h), none of which were seen in the tumor center.

At the tumor center of the peritoneum (Fig. 9e), cancer f cells still interacted with cancer a, b, d, g, and i cells, but not with cancer c cells, likely due to the shift in the composition of cancer cells within the TME. This observation was consistent with the results of the neighborhood analysis (Fig. 9h). In contrast, at the peritoneum invasion site, cancer f cells formed new interactions with cancer c, e, and h cells (also Fig. 9e). Cancer f cells in both regions maintained stable interactions with NK cells, macrophages, fibroblast c cells, endothelial a cells, and T cells. At the colonic metastatic site, the interactions between cancer f cells with other cancer cells were less pronounced. At the tumor center and periphery, cancer f cells mainly interacted with cancer b and e cells (Fig. 9f), while at the invasion and stroma regions, they additionally engaged with cancer a cells (Fig. 9i). However, cancer f cells in the colonic metastasis exhibited more complex interactions with immune and stromal cells, including NK cells, neutrophils, macrophages, fibroblast b and c cells, endothelial a and b cells, dendritic cells, and T cells, compared to the peritoneum and ovary.

Interestingly, cancer f cells exhibited autocrine signaling only in the peritoneal and colonic metastases but not in the ovary. In particular, the autocrine loop of cancer f cells in the peritoneum exhibited consistent SPP1 signaling from the tumor center to the invasion/stroma regions (S. Fig. 8e). In contrast, the autocrine loop of cancer f cells in the colon displayed consistent LIFR signaling throughout the same regions (S. Fig. 7e). The development of autocrine loops in metastatic sites might underscore the plasticity and adaptability of cancer f cells.

Projection of GeoMx clusters onto CosMx cancer cell types revealed a unique lineage of cancer f cells in OCCC

To integrate all the various spatial profiling data into context, we subsequently projected the GeoMx OCCCC clusters (C1a, C1b, C2, TME) onto selected CosMx OCCC cancer cell subtypes in their

respective geospatial localizations by GSVA. Correlation analysis between GeoMx clusters and the dominant cancer clones identified in the ovarian, peritoneal, and colonic sites revealsed how specific molecular signatures are associated with particular cancer cell populations across different tumour sites emphasizing the heterogeneity present in these cancer clones (Fig. 10a). In the ovary, the selected cancer cells correlated with 27.05% - 64.34% of the cluster signatures of C1a; 2.87% - 8.37% to C1b; 6.20% - 10.13% to C2; and 0.19% - 0.90% to TME. In the peritoneum, the correlations were 28.44% - 84.67% to cluster C1a; 2.78% - 6.95% to C1b, 2.93% - 8.52% to C2, and 0.23% - 0.87% to TME. The results indicated that a significant proportion of cancer cells in the ovary and peritoneum (22.08 - 56.39%) exhibited gene expression patterns that did not correlate with the GeoMx clusters and were marked as having negative scores. In contrast, only a relatively small proportion of cells (3.51-15.00%) in the colon had negative scores. At the colonic site, the selected cancer cells correlated with 70.00% - 90.13% to the signature of cluster C1a, 1.87% - 5.03% to C1b, 1.24% - 10% to C2, and 0.00% - 0.87% to TME. This suggested that OCCC cancer cells residing in the colonic site tended to be highly committed in terms of cellular identity.

Of note, 55.28% of the cancer f cells in the tumor center and and 40.12% of those in invasion regions of the peritoneum were marked with negative scores, the highest percentage of any negative-scoring subtype. This was in contrast to the other cancer cell types – for example cancer e cells comprised only a very small proportion of negative scores from the peritoneum (9.36%) to the colon (4.26 -15.00%). This indicated that within cancer f cells, there might exist further subsets with different characteristics, further emphasizing their potential in plasticity.

This plasticity of cancer f cells was further implied by the trajectory analysis in the peritoneum, which revealed that cancer f cells with negative GeoMx cluster scores appeared to be the origin of the cancer f and cancer e with positive scores (Figure 10b). The signatures of cancer f cells with negative

scores (S. Table 21) showed increased expression of *JUN*, *MALAT1*, *COL1A1*, *LIFR*, *NEAT1*, *TAGLN*, *ZFP36*, *ACKR3*, *RPS4Y1* and decreased expression of *TGFB1*, *KRT8*, *SOX9*, *KRT18*, *KRT19*, *MMP7*, *KRT23*, *LEFTY1*, *CD48*, *IGFBP3*, *CXCL12*, *TLR2*, *CCL2*, *CRP* (Figure 10c). This gene expression pattern suggested that negative-scoring cancer f cells could be more mesenchymal. In the peritoneum, we observed that the negative-scoring cancer f cells indeed had higher mesenchymal scores, compared to the cancer f and cancer e cells with positive GeoMx cluster scores ($P < 0.0001$) (Figure 10d, S. Fig. 8f). Intriguingly, compared to the cancer f cells with positive GeoMx cluster scores, the negative-scoring cancer f cells did not have significantly upregulated genes, only downregulated genes instead (S. Fig. 8g). This suggested that the plasticity between these 2 states of cancer f cells might be regulated through transcription suppression via mechanisms such as epigenetic dysregulation[48]. This set of downregulated genes indicated an immune evasion phenotype (*CCL2*, *CD48*, *CD74*, *CRP*, *HLA-DRB*, *TLR2*) which could lead to reduced immune activation, antigen presentation, and immune cell recruitment. In the negative scoring cancer f cells, the significant downregulation of *LCN2* also implied metabolic changes intrinsic to these founder cells. The downregulated *IGFBP3* and *TNF* expression also suggested the promotion of cell survival and proliferation by reducing apoptotic signals and inflammatory responses. Taken together, cancer f cells with negative GeoMx scores harbored intrinsic gene expression profiles shifting toward immune evasion and enhanced cell survival that would favor the growth of the OCCC cells.

Cancer f cells resided in specific neighborhood niche

We then examined adjacent FOVs at the peritoneal invasion site (FOVs 8 through 14) to further explore the neighborhoods of cancer f cells. Cancer f cells with negative scores were predominantly located in FOVs 13 and 14. In the neighboring FOVs (FOVs 8 through 12), we observed a small number of negative-scoring cancer f cells and an increase in positive-scoring cancer f cells, with the latter often

positioned next to cancer e cells (Fig 10e). The negative-scoring cancer f cells also showed shorter pseudotime path values compared to the rest of the cancer cells within these FOVs (Fig 10e). The cancer f cells in FOVs 13 and14 exhibited a more mesenchymal than epithelial characteristic by GSVA score, which was similar to those found at the ovarian invasion sites. This suggested that the cancer f cells that did not correlate with the GeoMx cluster geneset (i.e., the ones with negative scores) might represent an unique lineage within a niche TME, which were both more mesenchymal and "older" during the clonal progression trajectory. To answer the question of whether cancer f could also be identified in other cancer types, we examined the presence of OCCC cancer cells (types a to i) identified by CosMx in tissue samples in various cancer types profiled by Visium (Fig 11). Overall, the samples demonstrated a heterogeneous presence of different cancer cell populations. However, when focusing on cancer f cells, we observed that their niche-specific distributions in the OCCC and glioblastoma samples were as a minority population. This feature was absent in the endometrial adenocarcinoma_ovary and invasive lobular carcinoma_breast samples.

Since cancer f cells expressed significantly high levels of *NEAT1* compared to rest of the cancer cells (Fig. 8g, 10c), we asked whether *NEAT1* expression could be a prognostic marker for survival outcomes. High *NEAT1* expression (either above median or top 25%) was associated with poorer 5-year progression-free survival (PFS) (Hazard ratio = 0.7337, 95% CI: 0.4392 - 1.226, $P = 0.0853$) and overall survival (OS) (Hazard ratio = 0.6365, 95% CI: 0.3143 to 1.289, $P = 0.2100$) in an OCCC cohort[49] but not in the The Cancer Genome Atlas (TCGA) HGSC cohort[50] (Fig. 12). The association of *NEAT1* expression with PFS and OS varied among different cancer types in the TCGA PanCancer dataset[50] (Table 1). Intriguingly, high *NEAT1* expression was significantly associated with worse PFS and OS in lower-grade gliomas and glioblastomas ("GBMLGG"). Given that the distribution of cancer f cells was restricted to specific niches in both OCCC and GBM (Fig. 11), it was plausible that rapidly progressing tumors might

have higher proportions of *NEAT1*-expressing cells residing inside specific neighborhood niches. Unfortunately, *NEAT1* distribution patterns could not be further assessed in the Visium dataset, since this long non-coding RNA was not included.

Discussion

Our understanding of intra-tumor heterogeneity (ITH) and clonal evolution has been greatly enhanced by studies such as TRAcking renal cell Cancer Evolution through Therapy (TRACERx Renal)[51], which detailed how genetic diversity and chromosome complexity within tumor macro-subregions result in evolutionary subtypes that correlate with clinical phenotypes and patient outcomes. The matched primary/metastasis pairs of the TRACERx Renal cohort[52] further demonstrated varying metastatic phenotypes and the common fitness for metastasis. Metastatic subclones preferentially originate in harsh environments such as hypoxic regions within the tumor interior[53] via the acceleration of clonal evolution associated with spatial dynamics. This indicates that the *intrinsic* heterogeneity that arises from molecular alterations of tumor cells interconnects with the *extrinsic* heterogeneity within tumor microenvironments (TME), the latter of which is location-dependent[54] and exhibits significant spatial inequality[55].

In this current study, we adopted a small-scale study design (compared to a large-scale study like TRACERx) to explore the spatial ITH of ovarian clear cell carcinoma (OCCC), a rare cancer type with significant relevance to East Asian women compared to the most common high grade serous carcinoma (HGSC) subtype. For discovery, we profiled 382 spatial transcriptomic (ST) GeoMx segments in 21 matched OCCC and HGSC tumor sections from the primary ovarian and various metastatic sites followed by projecting to both in-house and public OCCC cohorts with available bulk gene expression data. Single cell CosMx ST profiling further identified novel OCCC cancer subclones which were partially linked to the GeoMx ST subclusters. The identified GeoMx subclusters and CosMx subclones were subsequently tested in the Visium ST platform across various cancer types to confirm generalizability. One specific CosMx subclone feature with founder niche potential was then further validated for its correlation with clinical outcomes in the PanCancer dataset.

OCCC has been shown to exhibit both epithelial (EpiCC) and mesenchymal (MesCC) subtypes, based on bulk transcriptomic profiles[26]. However, it is unclear whether there is an intrinsic ITH of these epithelial and mesenchymal gene expression subtypes within OCCC. Herein, by using various ST profiling methods, we reported that OCCC tumor cells exhibited significant heterogeneity in terms of functional spectra along epithelial-mesenchymal (EM) gradients associated with differential geospatial distributions. This comprehensive ST study revealed both ITH and site-specific adaptations within OCCC. Our findings elucidated the complex interplay between cancer cells, immune components, and stromal elements across primary and metastatic sites of OCCC. The identification of three GeoMx cancer cell clusters together with nine distinct SMI cancer cell subtypes, each with unique gene expression profiles and geospatial distributions, underscored the remarkable plasticity and complexity of OCCC.

EMT has been suggested to contribute to carcinoma progression[72] and it may be the first step for the metastasis of ovarian cancer cells to the peritoneum through the passive movement of ascitic fluid[56]. However, from the clinicopathological perspective, the changes inherent to EMT are often not visually discernable by routine histopathological examinations. This is because EMT usually only occurs in a selected tumor cell population either at the invasive fronts or close to the hypoxic region[73]. In addition, the detection methods for EMT in the clinicopathological settings have not been optimally established. Various EMT scoring schema have been proposed[74], but none have yet reached clinical use. In view of all these, our study was able to decode the nature of tumoral heterogeneity interlinked with EM phenotypes. Through the discovery of a geospatial distribution of an EM gradient associated with functional changes, we were able to decipher OCCC more precisely while preserving spatial details.

In addition, OCCC is known to possess metabolic features distinctly different from the other subtypes of epithelial ovarian cancer, such as abundant glycogen storage and high OXPHOS activity[35,54,59]. Our results suggested an inverse relationship between the enrichment of OXPHOS and EMT within

OCCC tumor cells, accompanied with functional changes in gradient. In the GeoMx C1a OCCC tumor cells, we observed high OXPHOS and glycolysis activity and low EMT enrichment, particularly in those located in tumor center. Similarly, in C1b tumor cells, we observed intermediate OXPHOS and glycolysis activity and high EMT enrichment, this time accompanied by enhanced inflammation-related signals like TNF-α/NF-κB and IL-6/JAK/STAT3 signaling, which were particularly significant in cells at the tumor periphery. In C2 tumor cells, high EMT states were even more apparent with hypoxic and DNA damage signals, particularly in those at the tumor invasion and necrotic regions. This interconnectedness between EMT and metabolism in OCCC cells was further explored in the isogenic partial EMT (pEMT) model using two distinct OCCC cell lines, from which four stable clones with varying EMT statuses were developed. The *in vitro* findings aligned with observations derived from GSVA projection onto patient tumor samples, revealing a decreasing trend in glycolytic activity as EMT gradients increased. Guerra *et al.* reported that dysfunction in OXPHOS may contribute to the initiation of EMT[59], and Mori *et al.* reported on the importance of crosstalk between EMT and cell metabolism to the stability of cells in hybrid states[32]. It is known that cellular heterogeneity leads to metabolic heterogeneity because metabolic programs within the tumor are dependent not only on the TME cellular composition but also on cell states, location, and nutrient availability[54]. By associating metabolic profiles with tumor behavior, we observed trends indicating that both basal glycolytic rate and metastatic potential may inversely correlate with EMT gradients. Furthermore, our data provides evidence that this interconnectivity exists even in cancer cells displaying intermediate EM states without histologically apparent morphological changes, highlighting the need to adopt sophisticated tools such as ST profiling to uncover EM heterogeneity with granularity. Nonetheless, in our pEMT model, the metabolic phenotype alone may not sufficiently predict tumor dynamics. Heterogeneity of inherent bioenergetics profiles of OCCC cells may also exist, since the mitochondrial activity showed substantial differences between different cell lines[33]. Therefore,

establishing a more comprehensive EMT spectrum with additional cell lines or patient samples could further elucidate the interplay between EMT and metabolism in OCCC.

Inflammation has also been reported to alter tumor cell metabolic traits[60], while, EMT has been linked to the release of pro-inflammatory cytokines from tumor cells, and inflammation itself is also known to be a trigger of EMT in tumor cells[61]. Overall, when compared to the other tumor cells, OCCC C1b tumor cells may present early a hybrid-EM cell state undergoing invasion and EMT. Previous research has demonstrated that ovarian cancer cells in the intermediate mesenchymal state are more aggressive compared to those with other EMT phenotypes[62]. Moreover, the enrichment of the mitotic spindle hallmark showed nadirs in C1b tumor cells and the tumor cells at the tumor periphery, suggesting a trade-off between migration and proliferation which may contribute to quiescence-related chemoresistance as well[63,64]. Interestingly, mesenchymal-like characteristics with enrichment in DNA repair and mitotic spindle were found in C2 OCCC tumor cells, revealing a possible relationship between EMT and DNA damage response[65]. In brief, our results may have deconvoluted the intricate connectedness between EMT, metabolism, and inflammation within OCCC tumor cells.

Furthermore, information about tumor microenvironment (TME) is crucial for deciphering the behaviors of and changes in the molecular signaling programs of tumor cells[66-68]. By assessing the EMT scores of the tumor cell-paired TME, we found that TME_Nest (within the tumor nest) and TME_C1a cells were more epithelial-like, while TME_TSI (at the tumor/stroma interface) and TME_C1b cells were more mesenchymal-like. Spatially speaking, in TME_Nest compared to TME_TSI, more enrichment of epithelial-like traits in mTORC1 signaling and enrichment in TGF-β signaling, glycolysis, apical junction, and angiogenesis-related biological process implied a more immunosuppressive, metabolically-altered, and angiogenetic microenvironment[69-72]. For the adjacent tumor cell aspect, the enrichemnt of myogenesis in TME_C1a might imply recruitment of cancer-associated fibroblasts (CAFs)[73], and enriched IL-

6/JAK/STAT3 signaling in TME_C1b echoed inflammation-related characteristics of C1b OCCC tumor cells, indicating the possible existence IL-6 related autocrine and paracrine circuits between or within C1b tumor cells and the surrounding TME[70,71]. However, limited by the number of accessible tumor cell-paired TMEs and the subcellular resolution of NanoString DSP, we were unable to directly infer possible cell-cell interactions between tumor cells and TME. Therefore, the single cell spatial transcriptomic profiling data derived from SMI provided a more comprehensive description of the TME neighborhoods.

Notably, the emergence of cancer cell f as a potential founder population, capable of giving rise to other lineages and demonstrating enhanced metastatic potential, provides crucial insights into the mechanisms of OCCC progression and dissemination. The observed organotropism in cellular-composition and gene-expression patterns between the primary ovarian tumors and the metastatic sites in the peritoneum and colon highlights the adaptive nature of OCCC. This adaptability is further exemplified by the dynamic changes in the EM characteristics of cancer cells, particularly subtype f, as they transitioned from the primary to the metastatic sites. The distinct microenvironmental interactions observed for cancer f across different anatomical locations underscores the importance of context-specific cellular communication in shaping tumor behavior. The development of autocrine signaling loops in metastatic sites, particularly involving SPP1 and LIFR, highlights potential mechanisms of adaptive resistance and survival in OCCC metastases. In previous research, SPP1 was identified as a marker for the protumor subpopulation of tumor-associated macrophages (TAMs) in lung adenocarcinomas[76] and was also associated with a shorter overall survival time in glioma patients[77]. Furthermore, the heterogeneity observed in fibroblast populations and their tissue-specific distributions emphasizes the critical role of the TME in modulating cancer cell behavior[78]. The dynamic interplay between cancer cells and stromal elements likely contributes to the aggressive nature of OCCC and its propensity for peritoneal and colonic metastasis.

The results from the TRACERx Renal study are particularly relevant to the current OCCC study. It is known that OCCC bears a higher molecular resemblance to the clear cell renal cell carcinoma (ccRCC) than other ovarian cancer subtypes[51]. A recent finding from analyzing the spatial patterns of transcriptional and TME heterogeneity in TRACERx Renal tumors has shown that their transcriptional evolution followed a conserved path through increasing cell proliferation and oxidative phosphorylation and downregulating DNA repair from earlier to later clones[79]. This notion mirrors with the inverse relationships between OXPHOS, inflammation, and DNA damage response along the EMT gradient we identified; functionally, the less epithelial the clone, the faster its tumor grew, although its metastatic potential was reduced. The latter finding reflect a "go or grow" trade-off faced by tumor cells *in vivo*[86]. The hypoxic and necrotic subregions within the TRACERx Renal tumors also had higher clonal diversity[53]. Another study on 17 ccRCC samples using 37 protein targets for GeoMx profiling also revealed that tumor periphery was a highly active biological niche[80]. These data collectively suggest that the tumor clonal structure identified in OCCC might be generalizable in tumors with similar molecular features. It is therefore very interesting to note that in Ren *et al.'s* series, glioblastomas showed a highly similar niche feature of the OCCC cancer cell f subclones, with *NEAT1* showing significance in the survival outcomes of the GBMLGG (lower grade glioma and glioblastoma) cohort. Although our finding was limited by the very small and selective number of samples analyzed, it will be intriguing to see whether the cancer cell f niche bears similar overlaps with the invasive niche-specific ecosystems and regulatory programs identified in glioma[81].

Conclusion

This study provides unprecedented insights into the cellular and molecular heterogeneity landscape of OCCC progression and metastasis. An inverse relationship among OXPHOS, inflammation, DNA

damage response along the EMT gradient has been revealed via spatial transcriptomic profiling. The identification of specific cancer cell subclones with high *NEAT1* expression and intermediate EM states as a key player in the evolutionary process will open new avenues to design early intervention strategies. Future research should focus on the functional significance of the observed cellular interactions and spatially-distinct gene expression patterns.

Materials and Methods

NanoString GeoMx Digital Spatial Profiling Cancer Transcriptomic Atlas analyses

The study was approved by the Institutional Review Board (IRB) of National Taiwan University Hospital (NTUH, No. 202005080RIND). Tumor tissue sections (5 μm) were obtained from archived formalin-fixed paraffin-embedded (FFPE) blocks. The cut FFPE sections were then baked at 60 °C for 1 hour, followed by sequential deparaffinization and rehydration with 100% and 95% ethanol. After washing with PBS, the tissue sections were incubated in 100 °C Tris EDTA for 15 min and in 37 °C Proteinase K (1 mg/mL) PBS solution for 15 min respectively to retrieve and expose RNA targets. The tissue sections were then incubated overnight in a hybridization solution, containing 1,812-plexed GeoMx Cancer Transcriptomic Atlas panel (NanoString, Seattle, WA, USA) at 37 °C and covered with HybriSlip Hybridization Covers (Grace BioLabs, 714022). The sections were then soaked in 2X SSC with 0.1% Tween-20 to remove the HybriSlip covers, and two rounds of stringent washes at 37 °C were performed.

Tissue sections were next placed in a humidity chamber and incubated in blocking buffer for 30 min at room temperature. Incubation of visualization markers, including SYTO 13 (1:10) (Thermo Fischer, Waltham, MA, USA), PanCK-Cy3 (1:40) nucleic stain and CD45-Texas Red (1:40) fluorescently labeled

antibodies, was performed for 1 hour. The stained sections were loaded into a GeoMx DSP system, followed by the selection of region of interests (ROIs). All the OCCC and HGSC samples in the study were annotated by a pathologist on the H&E slides. The ROI selections were based on the annotation of their respective H&E slides. The ROI sizes ranged from 200 μm to 700 μm in diameter. The ROIs were further compartmentalized into PanCK-positive (PanCK-pos, tumor cell) and PanCK-negative/CD45-positive (PanCK-neg/CD45-pos, tumor microenvironment) areas of illumination. UV light was projected onto each defined segment., and UV-photocleavable oligonucleotide barcodes were collected and dispensed into the corresponding wells of a microtiter plate for each AOI. Library preparation was performed with NanoString SeqCode primers (NanoString, Seattle, WA, USA), and AMPure XP beads (Beckman Coulter, Fischer Scientific, Waltham, MA, USA) were used for the pooling and purification of the polymerase chain reaction products. The constructed libraries were sequenced on a NextSeq 550 System (Illumina, San Diego, CA, USA), and the generated FASTQ files were then converted to raw counts with NanoString NGS Pipeline (Version 2.3.3.10, NanoString, Seattle, WA, USA).

10x Genomics CytAssist Visium Spatial Gene Expression analyses

Cut tumor tissue FFPE sections (5 μm) were baked at 42 °C for 3 hours and stored in a desiccated condition. Deparaffinization and H&E staining were both performed according to the manufacturer's instructions. H&E tissue images were obtained using an Imager Z2 (Zeiss) at 10x objective magnification. RNA targets were released from the tissue samples by decrosslinking, and further probe hybridization, probe ligation, probe release and extension, and library construction were performed; all were performed according to the manufacturers' instructions. Quantification of the pooled libraries was assessed with KAPA SYBR FAST qPCR Master Mix (KAPA Biosystems). Sample index PCR was performed with proper cycles suggested by qPCR amplification plot. The constructed libraries were sequenced by Illumina

NovaSeq 6000, with a dual-indexed setup for 150 base-pair paired-end. Both samples were sequenced with the recommended depth of approximately 50,000 reads per spot.

Cell culture and establishment of OCCC stable clones

The ovarian cancer cell lines JHOC9 and RMG2 were cultured in RPMI1640 containing 10% fetal bovine serum (FBS). For generating GRHL2 knockdown clones and their controls, plasmids carrying GRHL2 targeting stable short hairpin RNA (pLKO.1-shGRHL2, Sigma #TRCN0000015812) and control vectors (pLKO.1-shLuciferase, Sigma-Aldrich Cat.# SHC007) were utilized respectively. Plasmids were first mixed with MISSION® Lentiviral Packaging Mix (Sigma-Aldrich Cat.# SHP001) and transfection reagent X-tremeGENE ™ HP DNA Transfection Reagent (Roche Cat.# 06366236001) and were then added to 293T cells after 15-minute incubation under room temperature. 48 and 72 hours after transfection, virus-containing supernatants were harvested, filtered, and added to JHOC9 and RMG2 cells, along with 8 μg/ml polybrene (SigmaAldrich). 24 hours after infection, cells were subjected to puromycin selection at a concentration of 5 μg/ml. Concentrations of puromycin were determined according to kill curves of each cell line. JHOC9 and RMG2 stable clones were all maintained with 3-5 μg/ml of puromycin. Cellular phase-contrast images were obtained with Olympus CKX53 at 10x objective magnification.

Quantitative reverse transcription polymerase chain reaction (RT-qPCR)

Total RNA was extracted by RNeasy Mini Kit (Qiagen) according to the manufacturer's protocol. Five hundred nanograms of RNA were reverse-transcribed using RT2 First Strand Kit (Qiagen) and mixed with RT2 SYBR Green ROX qPCR Mastermix (SAbiosciences, Qiagen) for qPCR, for which QuantStudio 5 Real-Time PCR System was utilized. The thermocycling protocol consisted of a hold stage (95℃ for 10 min), a PCR stage (40 cycles of 95℃ for 15 sec and 60℃ for 1 min), and a melt curve stage

(95℃ for 15 sec, then 60℃ for 1 min, lastly 95℃ for 15 sec). The sequences of primers used are listed in S. Table 15. Two housekeeping gene expressions (ACTB, GAPDH) were used for normalization. For data interpretation, mRNA expression level was normalized to the average of housekeeping genes' expressions and presented as relative mRNA levels ($2-\Delta Ct$) or average fold change ($2^{-\Delta\Delta Ct}$) relative to its respective vector control.

Western blotting

Cell pellets were lysed with 1x RIPA buffer (Thermo Fisher Scientific) supplemented with a protease inhibitor cocktail (#539131, EMD Millipore, Billerica MA, USA) and a phosphatase inhibitor cocktail (#524625, EMD Millipore, Billerica MA, USA). Protein concentration was quantitated using the BCA Protein Assay Kit (#23227, Thermo Fisher Scientific). For each stable clone, thirty micrograms of collected protein mixed with loading dye were loaded into the wells of electrophoresis gel, and SDS-Polyacrylamide Gel Electrophoresis was carried out, with the concentration of stacking gel and resolving gel both 10%. After electrophoresis, the protein bands were transferred to a polyvinylidene difluoride (PVDF) membrane. After 2 hours, the PVDF membrane was blocked by 5% bovine serum albumin (BSA) in 1x Tris-buffered saline (TBS) and headed to overnight primary antibody incubation. The next day after washing the blot with 1x Tris-buffered saline with Tween® 20 (TBST), infrared dye-conjugated secondary antibody incubation was performed, followed by blot washing with 1x TBST. Finally, the blots were scanned using the Odyssey Infrared Imaging System (Li-COR).

For western blotting, primary antibodies were diluted in 1x TBST with 5% BSA. The primary antibodies used included: Purified Mouse Anti-E-Cadherin Clone 36/E-Cadherin (BD Bioscience Cat. # (421)610182; 1:1000); Anti-GRHL2 antibody produced in rabbits (Sigma-Aldrich Cat. # HPA004820; 1:500); Vimentin, Clone Vim 3B4 (Dako Cat.# M702001-2; 1:1000); Anti-β-Actin antibody, Mouse

monoclonal (Sigma-Aldrich Cat. # A1978; 1:5000). The secondary antibodies used included: Goat anti-Mouse IRDye 800CW (Li-COR Cat. # 926-32210); Goat anti-Rabbit IRDye 680RD (Li-COR Cat. # 926-68071) diluted at 1:10000 in 1x TBST.

MTS assay

In vitro cell proliferation was assessed by the colorimetric MTS assay (#G5430, CellTiter 96® Aqueous NonRad Proliferation Assay; Promega, Fitchburg, WI, USA) according to the manufacturer's protocol. Briefly, 1000 JHOC9 cells or 1500 RMG2 cells were seeded per well in 96-well plates one day prior to the assay. The assay was performed over a period of 5 days by measuring absorbance at 490 nm after 1 hour of incubation with CellTiter 96® Aqueous reagent. All values were corrected for background by subtracting the blank, and the relative ratios of the corrected absorbances were calculated.

Chorioallantoic Membrane-xenograft (CAM-X) assay

S. Fig. 6f summarizes the overall workflow of our CAM-X assay. Fertilized SPF (specific pathogen free) eggs from a local commercial hatchery were purchased and designated as "embryonic day 0" (ED0). Eggs were wiped with dry paper towels moistened with ddH2O to remove dirt. Then eggs were set horizontally and incubated in an automatic incubator at 37.8 °C and 70% humidity. On ED3, an 18G needle was inserted at the apex of the egg to remove 4 ml of albumin to lower the level of CAM to prevent sticking of the CAM on the shell. Then a 3MTM TegadermTM transparent film dressing was applied to prevent shell particles from falling onto the CAM. A window of 1cm*1cm was cut in the shell serving for follow-up observation, and the window was sealed using a 3MTM TegadermTM transparent film dressing.

On ED7, OCCC cells were inoculated onto the CAM. To optimize the number of engrafted cells, a gradient with 0.5, 1, 2 and 4 million RMG2 parental cells was tested. A trend indicating that tumor

growth becomes more pronounced with increasing cell concentration was observed (Chu et al., 2022; Fang et al., 2007). To minimize potential adverse effects of the inoculated tumor cells on the chick's normal physiological conditions, we ultimately chose 2 million tumor cells per egg as the experimental condition, as this was the minimum concentration that led to positive tumor growth. Briefly, the cancer cells were first trypsinized and centrifuged at 400 rpm for 3 minutes, and the media was removed. Then the cell pellet was mixed with Matrigel (#354234, Corning). Two million stable clone cells were mixed with 50 microliters of Matrigel for each egg. To prevent the Matrigel from solidifying, the mixture was kept on ice until inoculation. The CAM was gently tapped with an autoclaved glass rod prior to inoculation, and the cell-Matrigel mixture was grafted onto the CAM near the "Y" bifurcation of a blood vessel. The window was then sealed using a 3MTM TegadermTM transparent film dressing[39,40]. On ED11, tumor volume was measured via a Visualsonics Vevo® 2100 Imaging System or FUJIFILM Sonosite SII with a HSL25x transducer. The transparent film dressing was removed and a clean piece of cling wrap was placed over the exposed tumor. Ultrasound transducer gel was applied over the cling wrap and the transducer was lowered until it made contact with the gel. Ultrasound images were taken at two vertical cross sections at low 2D gain (5Hz). Then the width and depth of tumors from each cross section were measured. Tumor volume was calculated by multiplying the width from the two vertical cross sections and the average depth from the two sections. Later, the window was sealed again using a TegadermTM transparent film dressing.

On ED14, tumor volume was measured by ultrasound again. Tumor growth was defined by tumor volume change from ED11 to ED14 divided by the ED11 tumor volume. Later, the host chick embryo was swiftly sacrificed by decapitation, and CAM with engrafted tumors was removed for preparing formalin-fixed paraffin-embedded (FFPE) tissues. In addition, the chick liver and lower CAM were harvested and frozen in liquid nitrogen for further molecular analysis.

Human Alu sequence-based polymerase chain reaction (hAlu-PCR)

On ED14, the liver and lower CAM of chick embryos were harvested to perform human Alu-PCR, which detects human cells in chick tissues. Genomic DNA from the harvested liver and lower CAM tissues was prepared and purified using PureLink® Genomic DNA Kits. Thirty nanograms of purified genomic DNA was mixed with RT2 SYBR Green ROX qPCR Mastermix (SAbiosciences, Qiagen) and individual primer pairs (S. Table 16) for qPCR, conducted using the QuantStudio 5 Real-Time PCR System. The thermocycling protocol consisted of hold stage (95℃ for 2 min), PCR stage (35 cycles of 95℃ for 30 sec, 63℃ for 30 sec, and then 72℃ for 30 sec), and melt curve stage (95℃ for 15 sec, then 60℃ for 1 min, lastly 95℃ for 15 sec). Chick GAPDH (cGAPDH) served as a housekeeping gene for normalization, and ΔCt was defined as Ct(hAlu) − Ct(cGAPDH). To normalize tumor volume, metastasis level in each genomic DNA sample was presented as 2^−ΔCt/ED14 tumor volume.

Tumors with Ct(hAlu) less than the Ct(hAlu) of the negative control (nuclease-free H2O) were defined as having perceptible metastases. Only the CAMs with perceptible metastases were included in the above-mentioned calculation and data presentation. Meanwhile, metastatic penetrance was calculated by dividing the number of eggs with perceptible metastases by the total number of eggs in the group. In the present study, the penetrance reached nearly 100% in all groups (JHOC9_shLuc, JHOC9_shGRHL2, RMG2_shLuc, RMG2_shGRHL2), suggesting that the CAM model is a robust *in vivo* model for studying metastasis[39,40].

Gene Ontology (GO) analysis in OCCC cell lines

RNAs from KOC7C and JHOC9 stable clones were subjected to RNA-paired-end sequencing. The quality of RNA-seq data was assessed using FastQC v0.11.5 (http://www.bioinformatics.babraham.ac.uk/projects/fastqc/) and RNASeQC v1.1.861. Quality metrics

were within an acceptable range. Sequences were mapped to the human genome hg19 using STAR v2.5.3a[82] and transcripts were quantified using RSEM v1.3[83] with GENCODE v38 annotation. Each sample had an average read length of 150 and a unique mapping rate greater than 90% (average 60 million unique reads). EBseq v1.20.064 was used for differential expression analysis[84].

Statistical analysis of RNA-sequencing was conducted using Matlab® R2016b version 9.1.0.960167, statistics and machine learning toolbox version 11.0 (MathWorks; Natick, MA, USA). Differentially expressed genes (including those upregulated or downregulated) in the GRHL2 knockdown clones with PPEE (posterior probability of equal expression) < 0.05 were selected and formed numerous gene lists. These gene lists were then submitted for gene ontology (GO) analysis, a powerful tool to explore the relationships between gene products[85,86]. We performed the PANTHER Overrepresentation Test based on the Gene Ontology database[87]. Fisher's Exact Test with false discovery rate (FDR) correction was applied to each test. Only GO terms with FDR-adjusted p-value < 0.05 were selected.

Seahorse XFe24 Mito Stress assay

The Seahorse XFe24 Extracellular Flux Analyzer (Seahorse Bioscience, North Billerica, MA) was utilized to evaluate the bioenergetic profiles of OCCC cell lines. The outputs were recorded as oxygen consumption rate (OCR) and extracellular acidification rate (ECAR), indicating mitochondrial respiration and glycolytic activity, respectively. Firstly, cells were evenly seeded into the XFe24 cell culture plate (25,000 cells/well for JHOC9, 48,000 cells/well for RMG2; following optimization of cell seeding number) and maintained for adhering within 24 hours. Cell culture media was replaced with XF RPMI Medium (Agilent, 103576-100) supplemented with 2% FBS, 2 mM glutamine, and 11 mM glucose. The cells were then incubated for 1 hour at 37°C without CO2 prior to the experiment.

An Agilent Seahorse XF cell mito stress test kit was used to measure key parameters of mitochondrial function. After establishing the baseline readings, various drugs were injected, starting with 1μM oligomycin, followed by FCCP (1.5μM for JHOC9, 2.0μM for RMG2) and lastly 0.5μM rotenone/antimycin A. Oligomycin was added to inhibit proton (H+) flow through ATP synthase, effectively blocking all ATP-linked oxygen consumption. Maximal respiration was induced by adding carbonyl cyanide-4-(trifluoromethoxy)phenylhydrazone (FCCP), an uncoupler which disrupts mitochondrial membrane potential by transporting protons across the mitochondrial membrane. Rotenone/antimycin A was used to halt all mitochondrial respiration by blocking complex I and III. OCR and ECAR measurements were taken three times after each compound injection and drug concentrations were optimized for each cell line prior to experiments. Dose response curves (0.8μM-2μM) were performed before these experiments to determine the FCCP concentration needed for maximal OCR. JHOC9 reached a plateau of maximal OCR at 1.5μM FCCP, with inhibition observed at 2μM, whereas RMG2 cells achieved a plateau at 2μM FCCP.

Final OCR and ECAR readings were normalized to cell numbers in each well using ImageXpress Nano (Molecular Devices, San Jose, CA). Basal respiration was calculated by subtracting the non-mitochondrial OCR (the OCR remaining after rotenone/antimycin A addition) from the OCR measured before oligomycin addition. Maximal respiration was determined by subtracting the non-mitochondrial OCR from the OCR stimulated by FCCP addition. Respiratory reserve was defined as the difference between maximal and basal respiration. Basal ECAR was derived directly from the first three ECAR readings before any drug injection. Maximal ECAR was triggered by oligomycin (O, 1μM) addition. Glycolytic reserve was defined as the difference between maximal and basal ECAR.

NanoString CosMx Spatial Molecular Imaging Analysis

CosMx SMI Sample Preparation: FFPE sections (5 μm) were prepared and fixed, followed by a series of ethanol dehydration steps. Heat-induced epitope retrieval and proteinase K digestion were performed, and fiducials were added for alignment. *In situ* hybridization (ISH) was done with NanoString ISH probes, and the tissue was placed in a hybridization chamber for overnight incubation. After washing and blocking, a flow cell was affixed for RNA readout on the CosMx SMI instrument.

CosMx SMI Instrument Run: The flow cell was loaded onto the instrument, and RNA target readouts were performed with multiple rounds of reporter hybridization and imaging. After RNA readout, tissue samples were stained with antibodies and DAPI, and images were captured.

Image Processing and Feature Extraction: Raw images were processed using a pipeline that included registration, feature detection, and localization. RNA image analysis was used to identify reporter signatures, and their locations were recorded.

Cell Segmentation: Immunostaining and DAPI images were used for cell boundary drawing. The Cellpose algorithm was used to assign transcripts to cell locations and generate profiles for 193,619 cells, which were used for downstream analysis.

GeoMx Data normalization, analysis, and visualization

Analyses were performed under R version 4.3.3 with RStudio version 2024.04.1+748. Libraries, including NanoStringNCTools (version 1.8.0), GeomxTool (version 3.4.0), and GeoMxWorkflows (version 1.6.0), were used for the normalization of NanoString GeoMx DSP CTA data[3]. In brief, QC-passed AOIs and probes were included in the analyses. Limits of quantification (LOQ) were constructed based on geometric means and standard deviations of the raw counts of negative probes and were then used to filter AOIs.

The gene detection rate was used to filter genes. Afterwards, Q3 normalization with ComBat-seq[88] batch effect correction was performed. Heatmap and unsupervised hierarchical clustering by the top 20% of high-covariance genes, with Pearson correlation and average linkage, were conducted with the R pheatmap package (version 1.0.12). GSEA_4.2.2[89,90] with gene set permutation was used for gene set enrichment analysis. GSVA (version 1.48.3)[91]was used for the enrichment analysis of hallmarks[92] and cell type superimposition[36-38], with Poisson kernels for kernel estimation of the cumulative density function (kcdf). Dominant cell types of cell type superimposition results were defined with the cell type with highest GSVA enrichment score compared with the other cell types. Analyses of hallmark enrichment correlation matrix were conducted using corrplot (version 0.92), using its default hierarchical clustering settings and its addrect parameter set to 3. DESeq2 (version 1.40.2)[93] was used for differentially-expressed gene analysis.

The cell type signatures of C1a, C1b, C2 tumor cells were defined first by adjusted p-value < 0.05, and then by log2foldchange > 0.25 by comparing between PanCK-positive AOIs within these clusters. GO:BP terms of genes were determined with the function enrichGO[94,95]. Seurat v4 and standard sequencing-based spatial analysis pipeline were utilized for the analyses of 10x Visium data[96,97]. SCTransform 10x Visium data were used for assessment of enrichment of hallmarks and GeoMx_CellType_Feature with GSVA. Prism version 10.2.2 was used for data visualization.

CosMx Data normalization, analysis, and visualization

The NanoString CosMx SMI data for 1 advanced OCCC patient was processed using Seurat, following a vignette from the Satija Lab website. The LoadNanoString function in R was used to load the data, including cell boundary coordinates. Cells with fewer than 20 features were excluded. The data were combined into a single Seurat object, normalized using SCTransform, and analyzed with PCA and

clustering. Gene markers for UMAP clusters were identified using the FindAllMarkers function, and cell identities were manually assigned based on those known markers[37]. GSVA analysis was performed using the enrichment function[91] to calculate the correlation of gene expression of cosMx data with the TME signature[34] and GeoMx cluster. Trajectory analysis for the cancer cell population and fibroblast population was estimated by the Monocle3 package[98]. Gene markers for heatmaps were identified with the FindAllMarkers/ FindMarker function in Seurat. Cell-chat analysis[99] was used for single-cell interaction in specific histological areas. Neighbourhood enrichment analysis was calculated by Squidpy, using code by inspired Denisenko *et al.*[100]. The cellular composition of each spot was determined through the use of robust cell type decomposition (RCTD)[101].

Statistical analysis

For the OCCC cell lines study, unpaired Student's t-tests were conducted to examine the differences between groups for statistical significance using the Prism version 10.2.1. A p-value or adjusted p-value <0.05 was considered significant. Data visualization was also performed using the Prism version 10.2.1. If p-value or adjusted p-value <0.05, * was marked. Similarly, if p-value or adjusted p-value <0.01, <0.001, <0.0001, **, ***, **** were marked respectively. Error bars indicate the standard error of the mean (s.e.m.).

For statistical analysis, Chi-square tests were conducted using Microsoft Excel for Mac version 16.78.3; statistical significance of hallmark enrichment was evaluated with either the Mann-Whitney test or Kruskal-Wallis test using Prism version 10.2.2. Significance of Spearman's correlation of hallmark enrichment was evaluated with function cor in R environment. Statistical significance of generic EMT score was evaluated with Mann-Whitney test. Cell type deconvolution analysis was performed using

SpaCET[102]; assessment of generic EMT score[34]; and cell type superimposition analyses were also performed.

Disclosure Statement

The authors have no conflicts of interest to declare.

Funding Sources

This work was supported by the Yushan Scholar Program by the Ministry of Education, Taiwan (NTU-110V0402, 111V0402, 112V0402) and the Excellent Translational Medicine Research Projects (NTU CM and NTUH- 110C101-033 and 111C101-23) to R.Y.-J.H and (111C101-21) to Lin-Hung Wei; the NSTC Research Project (MOST 111-2314-B-002-128 and NSTC 112-2314-B-002-050) and the NTU Core Consortiums (NTUCC-109L893001, 110L891101, and 111L890501) to R.Y.-J.H and (MOST 111-2314-B-002-129) to Lin-Hung Wei. We thank the staff of the Sequencing Core, Department of Medical Research, National Taiwan University Hospital for their excellent technical support.

Author Contributions

Conceptualization, R.Y.-J.H. and Lin-Hung Wei; writing, Thang Truong Le, Duncan Yi-Te Wang, Ya-Ting Tai and R.Y.-J.H.; GeoMx and CosMx data acquisition, Jieru Ye, Ko-Chen Chen, Yi-Chia Chiu, and Duncan Yi-Te Wang; spatial data analysis and interpretation, Thang Truong Le, Duncan Yi-Te Wang, and Tuan Zea Tan, Jia-Yuh Sheu, Chen-Hao Huang, Hsueh-Fen Juan; pathology annotation and review, Wei-Chou Lin; clinical review, Lin-Hung Wei and Ya-Ting Tai; cell line study, RG Sebastian Yan, Pei-Yu Chu, Feng-Chiao Tsai. All authors have read and agreed to the published version of the manuscript.

Reference

[1] V. Bernard *et al.*, "Single-Cell Transcriptomics of Pancreatic Cancer Precursors Demonstrates Epithelial and Microenvironmental Heterogeneity as an Early Event in Neoplastic Progression," *Clin. Cancer Res. Off. J. Am. Assoc. Cancer Res.*, vol. 25, no. 7, pp. 2194–2205, Apr. 2019, doi: 10.1158/1078-0432.CCR-18-1955.

[2] L. C. Collins, M. L. Botero, and S. J. Schnitt, "Bimodal frequency distribution of estrogen receptor immunohistochemical staining results in breast cancer: an analysis of 825 cases," *Am. J. Clin. Pathol.*, vol. 123, no. 1, pp. 16–20, Jan. 2005, doi: 10.1309/hcf035n9wk40etj0.

[3] A. Kreso *et al.*, "Variable clonal repopulation dynamics influence chemotherapy response in colorectal cancer," *Science*, vol. 339, no. 6119, pp. 543–548, Feb. 2013, doi: 10.1126/science.1227670.

[4] K. Crouch *et al.*, "Humoral immune response of the small-spotted catshark, Scyliorhinus canicula," *Fish Shellfish Immunol.*, vol. 34, no. 5, Art. no. 5, May 2013, doi: 10.1016/j.fsi.2013.01.025.

[5] A. Pribluda, C. C. de la Cruz, and E. L. Jackson, "Intratumoral Heterogeneity: From Diversity Comes Resistance," *Clin. Cancer Res. Off. J. Am. Assoc. Cancer Res.*, vol. 21, no. 13, pp. 2916–2923, Jul. 2015, doi: 10.1158/1078-0432.CCR-14-1213.

[6] J. Goveia *et al.*, "An Integrated Gene Expression Landscape Profiling Approach to Identify Lung Tumor Endothelial Cell Heterogeneity and Angiogenic Candidates," *Cancer Cell*, vol. 37, no. 1, pp. 21-36.e13, Jan. 2020, doi: 10.1016/j.ccell.2019.12.001.

[7] I. Vitale, E. Shema, S. Loi, and L. Galluzzi, "Intratumoral heterogeneity in cancer progression and response to immunotherapy," *Nat. Med.*, vol. 27, no. 2, pp. 212–224, Feb. 2021, doi: 10.1038/s41591-021-01233-9.

[8] C.-H. Yun *et al.*, "The T790M mutation in EGFR kinase causes drug resistance by increasing the affinity for ATP," *Proc. Natl. Acad. Sci. U. S. A.*, vol. 105, no. 6, pp. 2070–2075, Feb. 2008, doi: 10.1073/pnas.0709662105.

[9] N. A. Saunders *et al.*, "Role of intratumoural heterogeneity in cancer drug resistance: molecular and clinical perspectives," *EMBO Mol. Med.*, vol. 4, no. 8, pp. 675–684, Aug. 2012, doi: 10.1002/emmm.201101131.

[10] M. Stoeckius *et al.*, "Simultaneous epitope and transcriptome measurement in single cells," *Nat. Methods*, vol. 14, no. 9, pp. 865–868, Sep. 2017, doi: 10.1038/nmeth.4380.

[11] P. Shahi, S. C. Kim, J. R. Haliburton, Z. J. Gartner, and A. R. Abate, "Abseq: Ultrahigh-throughput single cell protein profiling with droplet microfluidic barcoding," *Sci. Rep.*, vol. 7, 2017, doi: 10.1038/srep44447.

[12] R. Sg *et al.*, "Slide-seq: A scalable technology for measuring genome-wide expression at high spatial resolution," *Science*, vol. 363, no. 6434, Mar. 2019, doi: 10.1126/science.aaw1219.

[13] V. Marx, "Method of the Year: spatially resolved transcriptomics," *Nat. Methods*, vol. 18, no. 1, pp. 9–14, Jan. 2021, doi: 10.1038/s41592-020-01033-y.

[14] H. S *et al.*, "High-plex imaging of RNA and proteins at subcellular resolution in fixed tissue by spatial molecular imaging," *Nat. Biotechnol.*, vol. 40, no. 12, Dec. 2022, doi: 10.1038/s41587-022-01483-z.

[15] M. Cr *et al.*, "Multiplex digital spatial profiling of proteins and RNA in fixed tissue," *Nat. Biotechnol.*, vol. 38, no. 5, May 2020, doi: 10.1038/s41587-020-0472-9.

[16] S. Huang *et al.*, "Spatial transcriptomics: a new frontier in cancer research," *Clin. Cancer Bull.*, vol. 3, no. 1, p. 13, Jun. 2024, doi: 10.1007/s44272-024-00018-8.

[17] W.-C. Hsieh *et al.*, “Spatial multi-omics analyses of the tumor immune microenvironment,” *J. Biomed. Sci.*, vol. 29, no. 1, p. 96, Nov. 2022, doi: 10.1186/s12929-022-00879-y.
[18] D. P. Cook *et al.*, “A Comparative Analysis of Imaging-Based Spatial Transcriptomics Platforms,” Dec. 14, 2023, *bioRxiv*. doi: 10.1101/2023.12.13.571385.
[19] S. Lee, G. Kim, J. Lee, A. C. Lee, and S. Kwon, “Mapping cancer biology in space: applications and perspectives on spatial omics for oncology,” *Mol. Cancer*, vol. 23, no. 1, p. 26, Jan. 2024, doi: 10.1186/s12943-024-01941-z.
[20] X. Liu *et al.*, “Spatial multi-omics: deciphering technological landscape of integration of multi-omics and its applications,” *J. Hematol. Oncol.J Hematol Oncol*, vol. 17, no. 1, p. 72, Aug. 2024, doi: 10.1186/s13045-024-01596-9.
[21] Y.-T. Tai *et al.*, “Spatial profiling of ovarian clear cell carcinoma reveals immune-hot features,” *Mod. Pathol. Off. J. U. S. Can. Acad. Pathol. Inc*, p. 100630, Oct. 2024, doi: 10.1016/j.modpat.2024.100630.
[22] F. Wang *et al.*, “Single-cell and spatial transcriptome analysis reveals the cellular heterogeneity of liver metastatic colorectal cancer,” *Sci. Adv.*, vol. 9, no. 24, p. eadf5464, Jun. 2023, doi: 10.1126/sciadv.adf5464.
[23] C. Zuo, J. Xia, and L. Chen, “Dissecting tumor microenvironment from spatially resolved transcriptomics data by heterogeneous graph learning,” *Nat. Commun.*, vol. 15, no. 1, p. 5057, Jun. 2024, doi: 10.1038/s41467-024-49171-7.
[24] C. Y. Yeh *et al.*, “Mapping spatial organization and genetic cell-state regulators to target immune evasion in ovarian cancer,” *Nat. Immunol.*, pp. 1–16, Aug. 2024, doi: 10.1038/s41590-024-01943-5.
[25] Z. Li *et al.*, “Presence of onco-fetal neighborhoods in hepatocellular carcinoma is associated with relapse and response to immunotherapy,” *Nat. Cancer*, vol. 5, no. 1, pp. 167–186, Jan. 2024, doi: 10.1038/s43018-023-00672-2.
[26] T. Z. Tan *et al.*, “Analysis of gene expression signatures identifies prognostic and functionally distinct ovarian clear cell carcinoma subtypes,” *eBioMedicine*, vol. 50, pp. 203–210, Dec. 2019, doi: 10.1016/j.ebiom.2019.11.017.
[27] P. S and Q. Ma, “Clear-cell cancer of the ovary-is it chemosensitive?,” *Int. J. Gynecol. Cancer Off. J. Int. Gynecol. Cancer Soc.*, vol. 15, no. 3, Jun. 2005, doi: 10.1111/j.1525-1438.2005.15305.x.
[28] W. Novera *et al.*, “Cysteine Deprivation Targets Ovarian Clear Cell Carcinoma Via Oxidative Stress and Iron−Sulfur Cluster Biogenesis Deficit,” *Antioxid. Redox Signal.*, vol. 33, no. 17, p. 1191, Dec. 2020, doi: 10.1089/ars.2019.7850.
[29] Y. Iida *et al.*, “Hypoxia promotes glycogen synthesis and accumulation in human ovarian clear cell carcinoma,” *Int. J. Oncol.*, vol. 40, no. 6, pp. 2122–2130, Jun. 2012, doi: 10.3892/ijo.2012.1406.
[30] T. Tz *et al.*, “Decoding transcriptomic intra-tumour heterogeneity to guide personalised medicine in ovarian cancer,” *J. Pathol.*, vol. 247, no. 3, Mar. 2019, doi: 10.1002/path.5191.
[31] M. Cheng *et al.*, “Spatially resolved transcriptomics: a comprehensive review of their technological advances, applications, and challenges,” *J. Genet. Genomics*, vol. 50, no. 9, pp. 625–640, Sep. 2023, doi: 10.1016/j.jgg.2023.03.011.
[32] Y. Mori *et al.*, “Targeting PDGF signaling of cancer-associated fibroblasts blocks feedback activation of HIF-1α and tumor progression of clear cell ovarian cancer,” *Cell Rep. Med.*, vol. 5, no. 5, p. 101532, May 2024, doi: 10.1016/j.xcrm.2024.101532.
[33] M.-J. Devlin *et al.*, “The Tumor Microenvironment of Clear-Cell Ovarian Cancer,” *Cancer Immunol. Res.*, vol. 10, no. 11, p. 1326, Nov. 2022, doi: 10.1158/2326-6066.CIR-22-0407.

[34] T. Tz *et al.*, “Epithelial-mesenchymal transition spectrum quantification and its efficacy in deciphering survival and drug responses of cancer patients,” *EMBO Mol. Med.*, vol. 6, no. 10, Oct. 2014, doi: 10.15252/emmm.201404208.
[35] T. Z. Tan *et al.*, “CSIOVDB: a microarray gene expression database of epithelial ovarian cancer subtype,” *Oncotarget*, vol. 6, no. 41, pp. 43843–43852, Nov. 2015.
[36] M. A. S. Fonseca *et al.*, “Single-cell transcriptomic analysis of endometriosis,” *Nat. Genet.*, vol. 55, no. 2, pp. 255–267, Feb. 2023, doi: 10.1038/s41588-022-01254-1.
[37] V.-G. I *et al.*, “Ovarian cancer mutational processes drive site-specific immune evasion,” *Nature*, vol. 612, no. 7941, Dec. 2022, doi: 10.1038/s41586-022-05496-1.
[38] “Mapping the temporal and spatial dynamics of the human endometrium in vivo and in vitro | Nature Genetics.” Accessed: Sep. 18, 2024. [Online]. Available: https://www.nature.com/articles/s41588-021-00972-2
[39] P.-Y. Chu, A. P.-F. Koh, J. Antony, and R. Y.-J. Huang, “Applications of the Chick Chorioallantoic Membrane as an Alternative Model for Cancer Studies,” *Cells Tissues Organs*, vol. 211, no. 2, pp. 222–237, 2022, doi: 10.1159/000513039.
[40] E. I. Deryugina and J. P. Quigley, “Chick embryo chorioallantoic membrane model systems to study and visualize human tumor cell metastasis,” *Histochem. Cell Biol.*, vol. 130, no. 6, pp. 1119–1130, Dec. 2008, doi: 10.1007/s00418-008-0536-2.
[41] L.-Z. Liu *et al.*, “Acacetin inhibits VEGF expression, tumor angiogenesis and growth through AKT/HIF-1α pathway,” *Biochem. Biophys. Res. Commun.*, vol. 413, no. 2, pp. 299–305, Sep. 2011, doi: 10.1016/j.bbrc.2011.08.091.
[42] J. Fang *et al.*, “Apigenin inhibits tumor angiogenesis through decreasing HIF-1alpha and VEGF expression,” *Carcinogenesis*, vol. 28, no. 4, pp. 858–864, Apr. 2007, doi: 10.1093/carcin/bgl205.
[43] S. M. Frisch, J. C. Farris, and P. M. Pifer, “Roles of Grainyhead-like transcription factors in cancer,” *Oncogene*, vol. 36, no. 44, pp. 6067–6073, Nov. 2017, doi: 10.1038/onc.2017.178.
[44] V. Y. Chung *et al.*, “GRHL2-miR-200-ZEB1 maintains the epithelial status of ovarian cancer through transcriptional regulation and histone modification,” *Sci. Rep.*, vol. 6, p. 19943, Feb. 2016, doi: 10.1038/srep19943.
[45] B. Cieply, J. Farris, J. Denvir, H. L. Ford, and S. M. Frisch, “Epithelial-mesenchymal transition and tumor suppression are controlled by a reciprocal feedback loop between ZEB1 and Grainyhead-like-2,” *Cancer Res.*, vol. 73, no. 20, pp. 6299–6309, Oct. 2013, doi: 10.1158/0008-5472.CAN-12-4082.
[46] B. Cieply *et al.*, “Suppression of the epithelial-mesenchymal transition by Grainyhead-like-2,” *Cancer Res.*, vol. 72, no. 9, pp. 2440–2453, May 2012, doi: 10.1158/0008-5472.CAN-11-4038.
[47] Y. Yamada *et al.*, “Lipocalin 2 attenuates iron-related oxidative stress and prolongs the survival of ovarian clear cell carcinoma cells by up-regulating the CD44 variant,” *Free Radic. Res.*, vol. 50, no. 4, pp. 414–425, Apr. 2016, doi: 10.3109/10715762.2015.1134795.
[48] E. Ghorani, C. Swanton, and S. A. Quezada, “Cancer cell-intrinsic mechanisms driving acquired immune tolerance,” *Immunity*, vol. 56, no. 10, pp. 2270–2295, Oct. 2023, doi: 10.1016/j.immuni.2023.09.004.
[49] K. L. Bolton *et al.*, “Molecular Subclasses of Clear Cell Ovarian Carcinoma and Their Impact on Disease Behavior and Outcomes,” *Clin. Cancer Res.*, vol. 28, no. 22, pp. 4947–4956, Nov. 2022, doi: 10.1158/1078-0432.CCR-21-3817.
[50] J. N. Weinstein *et al.*, “The Cancer Genome Atlas Pan-Cancer Analysis Project,” *Nat. Genet.*, vol. 45, no. 10, pp. 1113–1120, Oct. 2013, doi: 10.1038/ng.2764.

[51] S. Turajlic *et al.*, "Deterministic Evolutionary Trajectories Influence Primary Tumor Growth: TRACERx Renal," *Cell*, vol. 173, no. 3, pp. 595-610.e11, Apr. 2018, doi: 10.1016/j.cell.2018.03.043.
[52] S. Turajlic *et al.*, "Tracking Cancer Evolution Reveals Constrained Routes to Metastases: TRACERx Renal," *Cell*, vol. 173, no. 3, pp. 581-594.e12, Apr. 2018, doi: 10.1016/j.cell.2018.03.057.
[53] Y. Zhao *et al.*, "Selection of metastasis competent subclones in the tumour interior," *Nat. Ecol. Evol.*, vol. 5, no. 7, pp. 1033–1045, Jul. 2021, doi: 10.1038/s41559-021-01456-6.
[54] E. N. Arner and J. C. Rathmell, "Metabolic programming and immune suppression in the tumor microenvironment," *Cancer Cell*, vol. 41, no. 3, pp. 421–433, Mar. 2023, doi: 10.1016/j.ccell.2023.01.009.
[55] X. Sun and Q. Yu, "Intra-tumor heterogeneity of cancer cells and its implications for cancer treatment," *Acta Pharmacol. Sin.*, vol. 36, no. 10, pp. 1219–1227, Oct. 2015, doi: 10.1038/aps.2015.92.
[56] G. Y, B. I, W. H, Z. W, R. Jm, and Z. Xh, "Metastasis Organotropism: Redefining the Congenial Soil," *Dev. Cell*, vol. 49, no. 3, May 2019, doi: 10.1016/j.devcel.2019.04.012.
[57] U. Dier, D.-H. Shin, L. P. M. P. Hemachandra, L. M. Uusitalo, and N. Hempel, "Bioenergetic Analysis of Ovarian Cancer Cell Lines: Profiling of Histological Subtypes and Identification of a Mitochondria-Defective Cell Line," *PLOS ONE*, vol. 9, no. 5, p. e98479, May 2014, doi: 10.1371/journal.pone.0098479.
[58] M. Mandai, Y. Amano, K. Yamaguchi, N. Matsumura, T. Baba, and I. Konishi, "Ovarian clear cell carcinoma meets metabolism; HNF-1β confers survival benefits through the Warburg effect and ROS reduction," *Oncotarget*, vol. 6, no. 31, p. 30704, Oct. 2015, doi: 10.18632/oncotarget.5228.
[59] G. F, G. N, A. Aa, B. C, G. S, and M. L, "Mitochondrial Dysfunction: A Novel Potential Driver of Epithelial-to-Mesenchymal Transition in Cancer," *Front. Oncol.*, vol. 7, Dec. 2017, doi: 10.3389/fonc.2017.00295.
[60] N. M *et al.*, "Inflammation and Metabolism in Cancer Cell-Mitochondria Key Player," *Front. Oncol.*, vol. 9, May 2019, doi: 10.3389/fonc.2019.00348.
[61] M. Suarez-Carmona, J. Lesage, D. Cataldo, and C. Gilles, "EMT and inflammation: inseparable actors of cancer progression," *Mol. Oncol.*, vol. 11, no. 7, pp. 805–823, Jul. 2017, doi: 10.1002/1878-0261.12095.
[62] R. Y.-J. Huang *et al.*, "An EMT spectrum defines an anoikis-resistant and spheroidogenic intermediate mesenchymal state that is sensitive to e-cadherin restoration by a src-kinase inhibitor, saracatinib (AZD0530)," *Cell Death Dis.*, vol. 4, no. 11, p. e915, Nov. 2013, doi: 10.1038/cddis.2013.442.
[63] A. Akhmetkaliyev, N. Alibrahim, D. Shafiee, and E. Tulchinsky, "EMT/MET plasticity in cancer and Go-or-Grow decisions in quiescence: the two sides of the same coin?," *Mol. Cancer*, vol. 22, no. 1, p. 90, May 2023, doi: 10.1186/s12943-023-01793-z.
[64] T. Celià-Terrassa and Y. Kang, "Distinctive properties of metastasis-initiating cells," *Genes Dev.*, vol. 30, no. 8, p. 892, Apr. 2016, doi: 10.1101/gad.277681.116.
[65] M.-L. C *et al.*, "Role of EMT in the DNA damage response, double-strand break repair pathway choice and its implications in cancer treatment," *Cancer Sci.*, vol. 113, no. 7, Jul. 2022, doi: 10.1111/cas.15389.
[66] H. Jm, C. Rl, and S. Ak, "Targeting the tumour microenvironment in ovarian cancer," *Eur. J. Cancer Oxf. Engl. 1990*, vol. 56, Mar. 2016, doi: 10.1016/j.ejca.2015.12.016.

[67] G. M, L. H, O. Jn, and J. D, "Decoding the coupled decision-making of the epithelial-mesenchymal transition and metabolic reprogramming in cancer," *iScience*, vol. 26, no. 1, Dec. 2022, doi: 10.1016/j.isci.2022.105719.
[68] D. Baci *et al.*, "The Ovarian Cancer Tumor Immune Microenvironment (TIME) as Target for Therapy: A Focus on Innate Immunity Cells as Therapeutic Effectors," *Int. J. Mol. Sci.*, vol. 21, no. 9, May 2020, doi: 10.3390/ijms21093125.
[69] M.-J. Goumans, Z. Liu, and P. ten Dijke, "TGF-β signaling in vascular biology and dysfunction," *Cell Res.*, vol. 19, no. 1, pp. 116–127, Jan. 2009, doi: 10.1038/cr.2008.326.
[70] N. M. Anderson and M. C. Simon, "The tumor microenvironment," *Curr. Biol. CB*, vol. 30, no. 16, pp. R921–R925, Aug. 2020, doi: 10.1016/j.cub.2020.06.081.
[71] S. Mafi *et al.*, "mTOR-Mediated Regulation of Immune Responses in Cancer and Tumor Microenvironment," *Front. Immunol.*, vol. 12, Feb. 2022, doi: 10.3389/fimmu.2021.774103.
[72] X. Shi *et al.*, "TGF-β signaling in the tumor metabolic microenvironment and targeted therapies," *J. Hematol. Oncol.J Hematol Oncol*, vol. 15, no. 1, p. 135, Sep. 2022, doi: 10.1186/s13045-022-01349-6.
[73] "Gastric cancer with enhanced myogenesis is associated with less cell proliferation, enriched epithelial-to-mesenchymal transition and angiogenesis, and poor clinical outcomes - PubMed." Accessed: Sep. 18, 2024. [Online]. Available: https://pubmed.ncbi.nlm.nih.gov/38323295/
[74] D. C. Chonov, M. M. K. Ignatova, J. R. Ananiev, and M. V. Gulubova, "IL-6 Activities in the Tumour Microenvironment. Part 1," *Open Access Maced. J. Med. Sci.*, vol. 7, no. 14, p. 2391, Jul. 2019, doi: 10.3889/oamjms.2019.589.
[75] D. Briukhovetska, J. Dörr, S. Endres, P. Libby, C. A. Dinarello, and S. Kobold, "Interleukins in cancer: from biology to therapy," *Nat. Rev. Cancer*, vol. 21, no. 8, pp. 481–499, Aug. 2021, doi: 10.1038/s41568-021-00363-z.
[76] M. E *et al.*, "The Significance of SPP1 in Lung Cancers and Its Impact as a Marker for Protumor Tumor-Associated Macrophages," *Cancers*, vol. 15, no. 8, Apr. 2023, doi: 10.3390/cancers15082250.
[77] C. He *et al.*, "Single-Cell Transcriptomic Analysis Revealed a Critical Role of SPP1/CD44-Mediated Crosstalk Between Macrophages and Cancer Cells in Glioma," *Front. Cell Dev. Biol.*, vol. 9, p. 779319, 2021, doi: 10.3389/fcell.2021.779319.
[78] K. E. de Visser and J. A. Joyce, "The evolving tumor microenvironment: From cancer initiation to metastatic outgrowth," *Cancer Cell*, vol. 41, no. 3, pp. 374–403, Mar. 2023, doi: 10.1016/j.ccell.2023.02.016.
[79] Á. Sanromán *et al.*, "Abstract 1621: Integrated analysis of genetic, transcriptional and TME evolution of ccRCC: TRACERx Renal," *Cancer Res.*, vol. 84, pp. 1621–1621, Mar. 2024, doi: 10.1158/1538-7445.AM2024-1621.
[80] F. Schneider *et al.*, "Digital Spatial Profiling Identifies the Tumor Periphery as a Highly Active Biological Niche in Clear Cell Renal Cell Carcinoma," *Cancers*, vol. 15, no. 20, Art. no. 20, Jan. 2023, doi: 10.3390/cancers15205050.
[81] Y. Ren *et al.*, "Spatial transcriptomics reveals niche-specific enrichment and vulnerabilities of radial glial stem-like cells in malignant gliomas," *Nat. Commun.*, vol. 14, no. 1, p. 1028, Feb. 2023, doi: 10.1038/s41467-023-36707-6.
[82] A. Dobin *et al.*, "STAR: ultrafast universal RNA-seq aligner," *Bioinforma. Oxf. Engl.*, vol. 29, no. 1, pp. 15–21, Jan. 2013, doi: 10.1093/bioinformatics/bts635.

[83] B. Li and C. N. Dewey, "RSEM: accurate transcript quantification from RNA-Seq data with or without a reference genome," *BMC Bioinformatics*, vol. 12, no. 1, p. 323, Aug. 2011, doi: 10.1186/1471-2105-12-323.
[84] N. Leng *et al.*, "EBSeq: an empirical Bayes hierarchical model for inference in RNA-seq experiments," *Bioinforma. Oxf. Engl.*, vol. 29, no. 8, pp. 1035–1043, Apr. 2013, doi: 10.1093/bioinformatics/btt087.
[85] Gene Ontology Consortium, "The Gene Ontology resource: enriching a GOld mine," *Nucleic Acids Res.*, vol. 49, no. D1, pp. D325–D334, Jan. 2021, doi: 10.1093/nar/gkaa1113.
[86] M. Ashburner *et al.*, "Gene ontology: tool for the unification of biology. The Gene Ontology Consortium," *Nat. Genet.*, vol. 25, no. 1, pp. 25–29, May 2000, doi: 10.1038/75556.
[87] H. Mi, A. Muruganujan, D. Ebert, X. Huang, and P. D. Thomas, "PANTHER version 14: more genomes, a new PANTHER GO-slim and improvements in enrichment analysis tools," *Nucleic Acids Res.*, vol. 47, no. Database issue, pp. D419–D426, Jan. 2019, doi: 10.1093/nar/gky1038.
[88] Z. Y, P. G, and J. We, "ComBat-seq: batch effect adjustment for RNA-seq count data," *NAR Genomics Bioinforma.*, vol. 2, no. 3, Sep. 2020, doi: 10.1093/nargab/lqaa078.
[89] V. K. Mootha *et al.*, "PGC-1alpha-responsive genes involved in oxidative phosphorylation are coordinately downregulated in human diabetes," *Nat. Genet.*, vol. 34, no. 3, pp. 267–273, Jul. 2003, doi: 10.1038/ng1180.
[90] A. Subramanian *et al.*, "Gene set enrichment analysis: A knowledge-based approach for interpreting genome-wide expression profiles," *Proc. Natl. Acad. Sci.*, vol. 102, no. 43, pp. 15545–15550, Oct. 2005, doi: 10.1073/pnas.0506580102.
[91] S. Hänzelmann, R. Castelo, and J. Guinney, "GSVA: gene set variation analysis for microarray and RNA-Seq data," *BMC Bioinformatics*, vol. 14, no. 1, p. 7, Jan. 2013, doi: 10.1186/1471-2105-14-7.
[92] L. A, B. C, T. H, G. M, M. Jp, and T. P, "The Molecular Signatures Database (MSigDB) hallmark gene set collection," *Cell Syst.*, vol. 1, no. 6, Dec. 2015, doi: 10.1016/j.cels.2015.12.004.
[93] M. I. Love, W. Huber, and S. Anders, "Moderated estimation of fold change and dispersion for RNA-seq data with DESeq2," *Genome Biol.*, vol. 15, no. 12, p. 550, Dec. 2014, doi: 10.1186/s13059-014-0550-8.
[94] A. Sa *et al.*, "The Gene Ontology knowledgebase in 2023," *Genetics*, vol. 224, no. 1, May 2023, doi: 10.1093/genetics/iyad031.
[95] M. Ashburner *et al.*, "Gene Ontology: tool for the unification of biology," *Nat. Genet.*, vol. 25, no. 1, pp. 25–29, May 2000, doi: 10.1038/75556.
[96] Y. Hao *et al.*, "Dictionary learning for integrative, multimodal and scalable single-cell analysis," *Nat. Biotechnol.*, vol. 42, no. 2, pp. 293–304, Feb. 2024, doi: 10.1038/s41587-023-01767-y.
[97] H. Y *et al.*, "Integrated analysis of multimodal single-cell data," *Cell*, vol. 184, no. 13, Jun. 2021, doi: 10.1016/j.cell.2021.04.048.
[98] C. J, S. Gk, and C. Y, "Unraveling the timeline of gene expression: A pseudotemporal trajectory analysis of single-cell RNA sequencing data," *F1000Research*, vol. 12, Nov. 2023, doi: 10.12688/f1000research.134078.2.
[99] S. Jin *et al.*, "Inference and analysis of cell-cell communication using CellChat," *Nat. Commun.*, vol. 12, no. 1, p. 1088, Feb. 2021, doi: 10.1038/s41467-021-21246-9.
[100] E. Denisenko *et al.*, "Spatial transcriptomics reveals discrete tumour microenvironments and autocrine loops within ovarian cancer subclones," *Nat. Commun.*, vol. 15, no. 1, p. 2860, Apr. 2024, doi: 10.1038/s41467-024-47271-y.
[101] D. M. Cable *et al.*, "Robust decomposition of cell type mixtures in spatial transcriptomics," *Nat. Biotechnol.*, vol. 40, no. 4, pp. 517–526, Apr. 2022, doi: 10.1038/s41587-021-00830-w.

[102] B. Ru, J. Huang, Y. Zhang, K. Aldape, and P. Jiang, "Estimation of cell lineages in tumors from spatial transcriptomics data," *Nat. Commun.*, vol. 14, no. 1, p. 568, Feb. 2023, doi: 10.1038/s41467-023-36062-6.

Figure Legends

Figure 1: Study design and Digital Spatial Profiling (DSP) results

a, Study design and workflow of ovarian clear cell carcinoma (OCCC) samples. **b,** Unsupervised hierarchical clustering of CTA RNA expression data of PanCK-pos (black) and PanCK-neg/CD45-pos (white) AOIs with top 20% high-covariance genes. Gene ontology biological process (GO:BP) terms are annotated on the left-hand side; subclusters on top; and the names of the representative genes on the right-hand side. Heatmap color code: yellow = high expression, purple = low expression **c-f,** Gene Set Enrichment Analysis (GSEA) results revealing positive correlations for each subclusters. **c,** C1a. **d,** C1b. **e,** C2. **f,** TME. **g-i,** Frequency of distribution plots of PanCK-pos AOIs for each subclusters in terms of different annotations. **g,** Stage of progression. **h,** Organ site. **i,** Spatial locations. **j-m,** Distribution of all AOIs based on different annotations in UMAP space. **j,** Segmentation. **k,** Organ site. **l,** Spatial location. **m,** Unsupervised clustering subcluster. ;

Figure 2: Gene Set Variation Analysis (GSVA) revealing differential enrichment in hallmarks between tumor cell subgroups

a-h, GSVA results showing the extent of enrichment of the representative hallmarks in UMAP space, and violin plots based on spatial locations and unsupervised tumor cell subgroups. P-values were calculated using the Kruskal-Wallis test. **i-k,** Spearman correlation matrix of GSVA enrichment score between hallmarks by unsupervised tumor cell subgroups. Hierarchical clustering results of hallmarks based on Spearman's correlation were annotated with black rectangles. **l-m,** Violin plots revealing differential enrichment of hallmarks between primary and metastatic tumor cells. P-values were calculated from Mann-Whitney test. *Abbreviations*: see S. Table 6. For all subfigures, *: $p < 0.05$, **: $p < 0.01$, ***: $p < 0.001$, ****: $p < 0.0001$.

Figure 3: Epithelial-mesenchymal (EM) gradients between tumor cell subgroups

a-k, Assessment of generic EMT scores using violin plots, showing differential gradients between: **a,** tumor cells from C1, C2, and AOIs from TME subclusters; **b,** tumor cells from C1 and C2; **c,** subtypes C1a, C1b, and C2; **d,** different stages of progression; **e,** C1a tumor cells in primary and metastatic sites; **f,** C1b tumor cells in primary and metastatic sites; **g,** C2 tumor cells in metastatic and the other (primary and recurrent) sites; **h,** Patients 1 and 2; **i,** different spatial locations for tumor cells from both OCCC patients. **j-k,** different spatial locations for tumor cells from Patients 1 and 2, respectively. P-values calculated by Mann-Whitney test, n.s.: not significant, *p <0.05, **p <0.01, ***p <0.001, ****p <0.0001. Statistical significance of one vs. the rest comparison was shown in a table below each violin plot.

Figure 4: Differences in neighboring TME, cell type signatures, and superimposition results between tumor cell subgroups

a, Generic EMT scores between TME adjacent to C1a tumor cells (TME_C1a) and C1b tumor cells (TME_C1b). **b,** Frequency of distribution comparing between TME_C1a and TME_C1b in terms of geospaital locations. **c,** Frequency of distribution comparing between TME within TME_Nest and at TME_TSI in terms of adjacent tumor cell subgroups. P-values calculated by Fisher's exact test. **d,** Generic EMT scores between TME_Nest and TME_TSI.). P**e-i,** Violin plots showing functional differences in enrichement scores of hallmarks between TME_Nest and TME_TSI. **j-l,** Enrichment of GeoMx CTA cell subtype features of EpiCC and MesCC OCCC from CSIOVDB, as per Tan *et al.* (2019), repsectively.). **m-o,** Enrichment of GeoMx CTA cell subtype features of different histological subtypes of ovarian tumors. OCCC: ovarian clear cell carcinoma. ENDO: endometrioid carcinoma of the ovary. MUCI: mucinous ovarian carcinoma. MUCI-LMP: mucinous ovarian tumor of low malignant potential. HGSOC: high-

grade serous ovarian carcinoma (HGSC). LGSOC: low-grade serous ovarian carcinoma.. **p-r,** Frequency of distribution of OCCC and HGSC GeoMx CTA tumor cell (PanCK-pos AOI) data cell type superimposition results using scRNA-seq cell type marker lists from HGSC-, endometrium-, and endometriosis-related papers. **p,** HGSC as per Vázquez-García *et al.* (2022). **q,** Endometrium as per Garcia-Alonso*et al.* (2021). **r,** Endometriosis as per Fonseca *et al.* (2023). Functional enrichment for GO:BP terms of the published signature lists (S. Table 7). P-values calculated by Mann-Whitney test for **a**, **d-l**; by Fisher's Exact test for **c**; and by Chi-square test for **p – r**. For all subfigures, *: p <0.05, **: p <0.01, ***: p <0.001, ****: p <0.0001

Figure 5: Differential enrichment of hallmarks and cell types depicting the landscape of OCCC tissues with EM gradients

a, UMAP embeddings and clustering results of Visium data of the primary and colonic metastatic samples from OCCC Patient 1. **b,** Cell type deconvolution analysis results. **c,** Enrichment of representative hallmarks projected back to Visium spatial space. Violin plots were used to visualize the results by clusters. **d,** Assessment of generic EMT score sv enrichment of GeoMx_CTA_CellType_Features, consisting of C1a, C1b, and C2 tumor cells, and TME. P-values calculatued by Mann-Whitney test, n.s.: not significant, *p <0.05, ***p <0.001, ****p <0.0001.

Figure 6: EMT model constructed by OCCC cell lines depicting tumor metabolism and behavior along EMT gradients

a, Visualization of the cell clones studied along the EMT spectrum **b-c,** Mitochondrial oxidative phosphorylation (OXPHOS) and glycolytic activity in OCCC clones. **b** (left) = real time oxygen consumption rate (OCR) measurements. with oligomycin (O, 1μM), FCCP (F, 1.5μM for JHOC9, 2.0μM

for RMG2), and rotenone/antimycin A (R/A, 0.5μM) added at the indicated time points. x-axis: measurement order, P-values calculated by Unpaired t test, *p<0.05, ****p<0.0001, comparing shGRHL2 to their respective shLuc clones. **B,** OXPHOS (y-axis: OCR, pmol/min/1000 cells); **c,** Glycolysis (y-axis: ECAR, mpH/min/1000 cells). **d,** Bioenergetics profiles of OCCC clones. **e-f**, Tumor dynamics manifested in the CAM model. **e,** *T*umor growth. **f,** Metastasis assessed by human Alu PCR. Unpaired t tests showed no significant differences in tumor growth or metastasis between GRHL2 knockdown and their respective control clones. In **b-f**, data represents the means ±SEM.

Figure 7: Single-cell spatial transcriptomics uncovers specific organ-targeting tendencies

a, The UMAP visualisations highlight the clustering of 25 distinct single cell clusters identified from the cosMx spatial transcriptomics, with each cluster representing a unique cell type based on transcriptional profiles. **b,** Detailed characterisation of cellular components across ovarian, peritoneal, and colonic sites includes an overall breakdown of the total identified cell types. **c,** Heatmap visualizations of the most significantly-expressed marker genes for the 25 identified single cell clusters, highlighting gene expression patterns defining cellular identities. **d,** Comparative analysis of cancer cell composition in histological sections from the ovarian, peritoneal, and colonic sites. **e,** Comparative analysis of stromal cell composition in histological sections from the ovarian, peritoneal, and colonic sites.

Figure 8: Metastasis behavior of ovarian cancer cells by trajectory analysis

a-d, Present UMAP projections depicting cancer cell populations and their trajectories across three distinct tissue-ovarian, peritoneal, and colonic sites with brighter clusters indicate a longer pseudotime pathway, reflecting cells further along a developemental trajectory. **e,** Quantitative assessment of epithelial and mesenchymal score enrichment in cancer cells isolated across ovarian, peritoneal, and colonic sites. **f,** Comparative analysis of epithelial and mesenchymal scores for two specific cancer clones (f and e) to their spatial distribution within tumors, focusing on the tumor center versus the invasion front and surrounding stromal areas. **g,** Signature analysis of cancer f within the cancer cell population, identifying key molecular markers and phenotypic traits that distinguish this subtype from others. **h,** UMAP projections showing the distribution and trajectory of cancer f across ovarian, peritoneal, and colonic sites. **i,** Spatial geographical of cancer cell composition and the time spent by these cells in the ovarian invasion front and stromal regions. P-values calculated from the Mann-Whitney test, n.s.: not significant, *p <0.05, ***p <0.001, ****p <0.0001.

Figure 9: Interactions of cancer f cells within the cancer microenvironment at primary and metastatic sites.

a-c, HE-stained images display the distribution of selected FOVs utilized for cosMx analysis, complete with annotations provided by a pathologist for each FOV in ovarian, peritoneal, and colonic sites. **d-f,** Cell-interaction networks between cancer f and adjacent cell populations in selected regions of the TME, which focuses on the dynamics within tumor center and at the invasive front/stromal interfaces. **g-i**, The heatmap displays enrichment scores derived from the connectivity graph of cell clusters analyzed in each characteristic histological area, with particular emphasis on regions associated with tumour and invasion/stroma, supplementing the adjacent cell-interaction data.

Figure 10: Molecular Heterogeneity in Ovarian, Peritoneal, and Colon Tumors.

a, Correlation analysis between GeoMx clusters and the dominant cancer clones identified in the ovarian, peritoneal, and colonic sites. **b,** UMAP representations illustrate the distinct trajectories of cancer clones e and f within the invasion/stroma regions of the peritoneal site. **c,** Signature analysis comparing cancer f clone (all and only with negative scores) to the other cancer cell. **d,** Epithelial and mesenchymal scores for selected cancer cells at the peritoneal invasion/stroma interface, focusing on the molecular characteristics of cancer cells in the peritoneal. P-values from Mann-Whitney test, n.s.: not significant, *p <0.05, ***p <0.001, ****p <0.0001. **e,** Spatial reconstruction of cancer f and e clones within the invasion/stroma regions of the peritoneum, coupled with their corresponding pseudotime map and illustrating their developmental trajectory.

Figure 11: Heterogeneity in cellular landscape of cancer cell on visium data from different samples

Cancer cell from CosMx data were projected into Visium data samples showing spatially heterogeneous distribution and predominant cells characteristic of each sample. In which, the data Visium used includes 2 OCCC samples (ovarian and colonic sites) from Patient 2 provided by NTUH; 2 OCCC samples (ovarian site) from the Yutaroi data; 1 Endometrial Adenocarcinoma (Ovary) sample, 1 Invasive Lobular Carcinoma (Breast) sampel, and 1 Glioblastoma (Brain) sample from the 10X Genomics data.

Figure 12: Signature from cancer f reduced overall survival and progression-free survival in the OCCC cohort

Survival analyses of Bolton et al.'s OCCC and the TCGA-HGSOC cohorts. High expression of NEAT1 in the f cancer line was associated with overall survival in the Bolton cohort but not in the TCGA-HGSOC cohort. P-values from the Mann-Whitney test, n.s.: not significant, *p <0.05, ***p <0.001, ****p <0.0001.

Table 1. Cox regression analysis for NEAT1 among different cancer types in the TCGA PanCaner dataset.

Supplementary Figure Legends

Supplementary Figure 1: Gene Set Enrichment Analysis (GSEA) and geospatial characteristics of unsupervised hierarchical clustering subclusters

a-d, Word cloud visualization of GSEA results comparing AOIs in each subsluters to the rest. **a,** C1a vs. the rest. **b,** C1b. **c,** C2. **d,** TME. The size of the hallmark name represents the negative logarithm base 10 FDR *q*-value (denoted as -$\log_{10}$(FDRqval)). The color of the word represents normalized enrichemnt score (NES). **e-f,** Patient-wise frequencies of distribution of PanCK-pos AOIs for each subclusters in terms of geospatial annotations. **e,** Patient 1 (P1). **f,** Patient 2 (P2).

Supplementary Figure 2: Gene Set Variation Analysis (GSVA) showing differential hallmark gradients and correlation matrix

a, Heatmaps of GSVA results with hallmarks from Human MSigDB. Black rectangles were used to stress hallmarks of interest. **b,** Spearman correlation matrix of GSVA enrichment score between hallmarks for all PanCK-pos AOIs. **c-i,** GSVA results showing the extent of enrichment of the representative hallmarks in UMAP space, and violin plots based on geospatial location and unsupervised tumor cell subgroups. **c,** Glycolysis (GlyColy). **d,** Hypoxia. **e,** Inflammatory response (InFlaRe). **f,** TNF-α/NF-κB signaling. **g,** IL6/JAK/STAT3 signaling. **h,** TGF-β signaling (TGFbeta_Sig). **i,** KRAS signaling (upregulated). **j-m,** Spearman correlation matrices of GSVA enrichment scores between hallmarks by tumor cell spatial annotations. Hierarchical clustering results of hallmark correlation matrices are annotated with black rectangles

Supplementary Figure 3: Generic EMT score assessment

a, Assessment of generic EMT scores between tumor cells from different organ sites. **b-f,** Generic EMT score of tumor cells, patient-wise (P1 & P2). P-values from the Mann-Whitney test, n.s.: not significant, *: p <0.05, **: p <0.01, ***: p <0.001, ****: p <0.0001. Comparisons of the statistical significance between more than 2 groups are shown in tables below such violin plots.

Supplementary Figure 4: Tumor cell-paired TME, tumor cell subtype signatures, cell type superimposition results, and comparison between OCCC and HGSC

a-c, Sub-analyses of generic EMT scores between TME_Nest and TME_TSI. **d,** Violin plots showing functional differences in allograft rejection (AlloReject) enrichement scores between TME_Nest and TME_TSI. **e-g,** Functional differences in enrichement score between TME_C1a and TME_C1b. **h-i,** Representative enriched GO:BP terms of DEGs between tumor cell-paired TMEs. **j,** Representative enriched GO:BP terms of C1a, C1b, and C2 tumor cell signatures, respectively. **k,** Enrichment of GeoMx CTA cell type features (C1a, C1b, and C2 tumor cell features, respectively) of different molecular subtypes of ovarian tumors [18]. **l.** Unsupervised hierarchical clustering of CTA RNA expression data of OCCC and HGSC AOIs with top 20% high-covariance genes. **m,** Word cloud visualization of GSEA results comparing PanCK-pos AOIs between OCCC and HGSC tumor cells in C1, C1a, and C1b, respectively. The size of the hallmark name represents the negative logarithm base 10 FDR q-value (denoted as $-\log_{10}$(FDRqval)). The color of the word represents normalized enrichemnt score (NES). **n,** Assessment of generic EMT scores between OCCC and HGSC tumor cells in C1, C1a, and C1b, respectively. P-values from the Mann-Whitney test, **: p <0.01, ****: p <0.0001.

Supplementary Figure 5: Supplementary Visium data

Figure illustrates the spatial distribution of epithelial scores, mesenchymal scores, and key GeoMx features across different cancer types. In which, the data visium used includes 2 OCCC samples (ovarian and colonic sites) of Patient 2 from NTUH; 2 OCCC samples (ovarian site) from the Yutaroi data; and 1 Endometrial sample Adenocarcinoma Ovary (Ovary) 1 Invasive Lobular Carcinoma (Breast), and 1 Glioblastoma (Brain) sample from the 10X Genomics data.

Supplementary figure 6: Establishment of OCCC stable clones, their EMT characteristics and CAM workflow

a, Phase contrast microscopy of OCCC stable clones showing morphological changes induced by GRHL2 knockdown. Scale bars indicate 50µm. b, RT-qPCR showing GRHL2 expression in OCCC clones. JHOC9_shLuc and RMG2_shLuc serve as comparison standards for JHOC9 and RMG2 clones, respectively. P-values from Unpaired t test, **p<0.01, comparing each clone to comparison standard. **c,** RT-qPCR of EMT markers. Unpaired t tests revealed no significant differences in EMT marker expression studied between GRHL2 knockdown clones and their respective controls. **d,** Immunoblots of a single western blot showing EMT-related protein expression. Protein sizes (kDa) are noted below names. **e,** Triplicated MTS assay showing 5-day proliferation of OCCC clones. For each stable clone, proliferation is represented as the relative cell number normalized to day 1, indicated by fold changes to the initial absorbance at day 1. P-values from Unpaired t test, *p<0.05, **p<0.01, comparing GRHL2 knockdown clones to their respective controls. **f,** Workflow of the CAM-X assay. **g,** Relationship between the number of RMG2 parental cells inoculated onto the CAM and tumor growth, defined as the tumor volume change from ED11 to ED14 divided by ED11 tumor volume. In **b, c, e,** and **g,** data represents the means ±SEM.

Supplementary Figure 7. FFPE sections of the CAM tumors were profiled by using the GeoMx CTA panel. Selected ROIs were showed on the image with CTA module and H&E staining in JHOC9_shLuc (**a**) and JHOC9_GRHL2 (**b**) CAM tumors. **c,** Volcano plot showing the differentially expressed genes in PanCK positive cells of the JHOC9_shLuc vs. JHOC9_GRHL2 . The enrichment Log 2 fold change threshold was set to 1. Significance was indicated by –log10 $P < 0.05$.

Supplementary Figure 8: Supplementary CosMx data

a, Analysis of immune cell compositions within the histological regions of the ovarian, peritoneal, and colonic sites. **b,** Epithelial and mesenchymal scores for cancer cells at the ovarian invasion/stroma interface evaluating the molecular characteristics of cancer cells at this critical juncture. **c,** A hypothetical model depicting the metastatic processes of cancer e and f clones, illustrating the proposed pathways that facilitate the dissemination and establishment of these cancer cells in distant sites. **d,** Expression levels of SPP1 and LIFR signaling in cancer f clones within the peritoneal and colonic site showing the crucial autocrine loop of cancer f clone. **e,** Epithelial and mesenchymal scores for cancer cells at the peritoneal invasion/stroma interface. **f,** Quantitative assessment of epithelial and mesenchymal score enrichment in cancer e and f clones at peritoneal invasion/ stroma sites. **g,** Signature of cancer f with negative score compare to cancer f with positive score showed down regulation genes. P-value from the Mann-Whitney test, ****: $p < 0.0001$.

Supplementary tables

Supplementary tables are online available

Supplementary table 1. The number of collected and QC-passed 1800+ plex GeoMx Cancer Transcriptome Atlas of OCCC AOIs

Supplementary table 2. The geospatial distribution of AOIs.

Supplementary table 3: GO:BP terms for featuring genes of clade 1 (C1) and clade 2 (C2) from unsupervised hierarchical clustering results.

Supplementary table 4. The subgroup distribution of AOIs.

Supplementary table 5. The subgroup distribution of PanCK-pos AOIs based on geospatial distribution.

Supplementary table 6. Abbreviation of GenericEMT.Tumor score and hallmarks from Human MsigDB Collections.

Supplementary table 7. The subcluster distribution of RNA analysis PanCK-pos AOIs (with PanCK-neg/CD45-pos AOI in TME in the same ROI) and those of P1 and P2 based on their geographical distribution.

Supplementary table 8: DEG list of PanCK-paired TME comparing between either geographical annotations or adjacent tumor cell subgroups.

Supplementary table 9: GO:BP terms for DEGs of PanCK-paired TME comparing between either geographical annotations or adjacent tumor cell subgroups.

Supplementary table 10: Marker lists of GeoMx CTA cell types.

Supplementary table 11: GO:BP terms for markers of GeoMx CTA cell types.

Supplementary table 12. The number of collected and QC-passed 1800+ plex GeoMx Cancer Transcriptome Atlas RNA analysis OCCC and HGSC AOIs.

Supplementary table 13: Marker lists from HGSC-, endometrium-, and endometriosis-related publications.

Supplementary table 14: GO:BP terms for markers from HGSC-, endometrium-, and endometriosis-related publications.

Supplementary table 15: Enriched GO terms JHOC9&RMG2

Supplementary 16: Sequences of primers for quantitative reverse transcription polymerase chain reaction (RT-qPCR) and human Alu sequence-based polymerase chain reaction (hAlu-PCR).

Supplementary table 17: Post-Quality control for CosMx SMI data

Supplementary table 18: Gene marker of cosMx cell type annotation.

Supplementary table 19: Cell type composition in each organ of cosMx data

Supplementary table 20: Cancer f signature in the cancer cell population.

Supplementary table 21: Negative score of cancer f signature in the cancer cell population.

Fig. 1

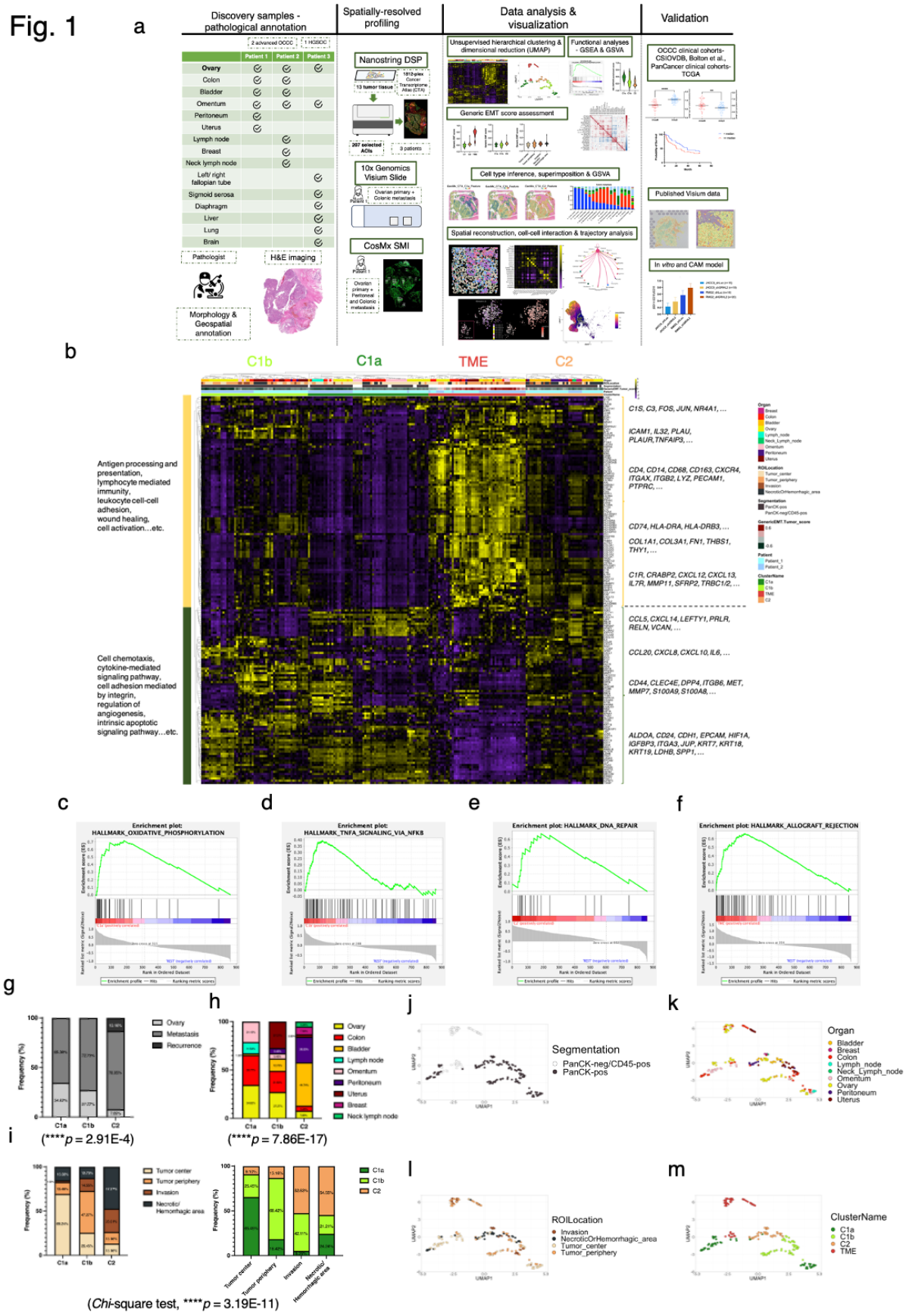
a
Discovery samples - pathological annotation
Spatially-resolved profiling
Data analysis & visualization
Validation
Nanostring DSP
10x Genomics Visium Slide
CosMx SMI
Pathologist
H&E imaging
Morphology & Geospatial annotation
Unsupervised hierarchical clustering & dimensional reduction (UMAP)
Functional analyses - GSEA & GSVA
Generic EMT score assessment
Cell type inference, superimposition & GSVA
Spatial reconstruction, cell-cell interaction & trajectory analysis
OCCC clinical cohorts- CSIOVDB, Bolton et al., PanCancer clinical cohorts- TCGA
Published Visium data
In vitro and CAM model
b
C1b
C1a
TME
C2
Antigen processing and presentation, lymphocyte mediated immunity, leukocyte cell-cell adhesion, wound healing, cell activation…etc.
Cell chemotaxis, cytokine-mediated signaling pathway, cell adhesion mediated by integrin, regulation of angiogenesis, intrinsic apoptotic signaling pathway…etc.
C1S, C3, FOS, JUN, NR4A1, …
ICAM1, IL32, PLAU, PLAUR, TNFAIP3, …
CD4, CD14, CD68, CD163, CXCR4, ITGAX, ITGB2, LYZ, PECAM1, PTPRC, …
CD74, HLA-DRA, HLA-DRB3, …
COL1A1, COL3A1, FN1, THBS1, THY1, …
C1R, CRABP2, CXCL12, CXCL13, IL7R, MMP11, SFRP2, TRBC1/2, …
CCL5, CXCL14, LEFTY1, PRLR, RELN, VCAN, …
CCL20, CXCL8, CXCL10, IL6, …
CD44, CLEC4E, DPP4, ITGB6, MET, MMP7, S100A9, S100A8, …
ALDOA, CD24, CDH1, EPCAM, HIF1A, IGFBP3, ITGA3, JUP, KRT7, KRT18, KRT19, LDHB, SPP1, …
c
Enrichment plot: HALLMARK_OXIDATIVE_PHOSPHORYLATION
d
Enrichment plot: HALLMARK_TNFA_SIGNALING_VIA_NFKB
e
Enrichment plot: HALLMARK_DNA_REPAIR
f
Enrichment plot: HALLMARK_ALLOGRAFT_REJECTION
g
Ovary
Metastasis
Recurrence
Frequency (%)
C1a
C1b
C2
(****p = 2.91E-4)
h
Ovary
Colon
Bladder
Lymph node
Omentum
Peritoneum
Uterus
Breast
Neck lymph node
(****p = 7.86E-17)
j
Segmentation
PanCK-neg/CD45-pos
PanCK-pos
UMAP1
UMAP2
k
Organ
Bladder
Breast
Colon
Lymph_node
Neck_Lymph_node
Omentum
Ovary
Peritoneum
Uterus
i
Tumor center
Tumor periphery
Invasion
Necrotic/ Hemorrhagic area
(Chi-square test, ****p = 3.19E-11)
l
ROILocation
Invasion
NecroticOrHemorrhagic_area
Tumor_center
Tumor_periphery
m
ClusterName
C1a
C1b
C2
TME

Fig. 2

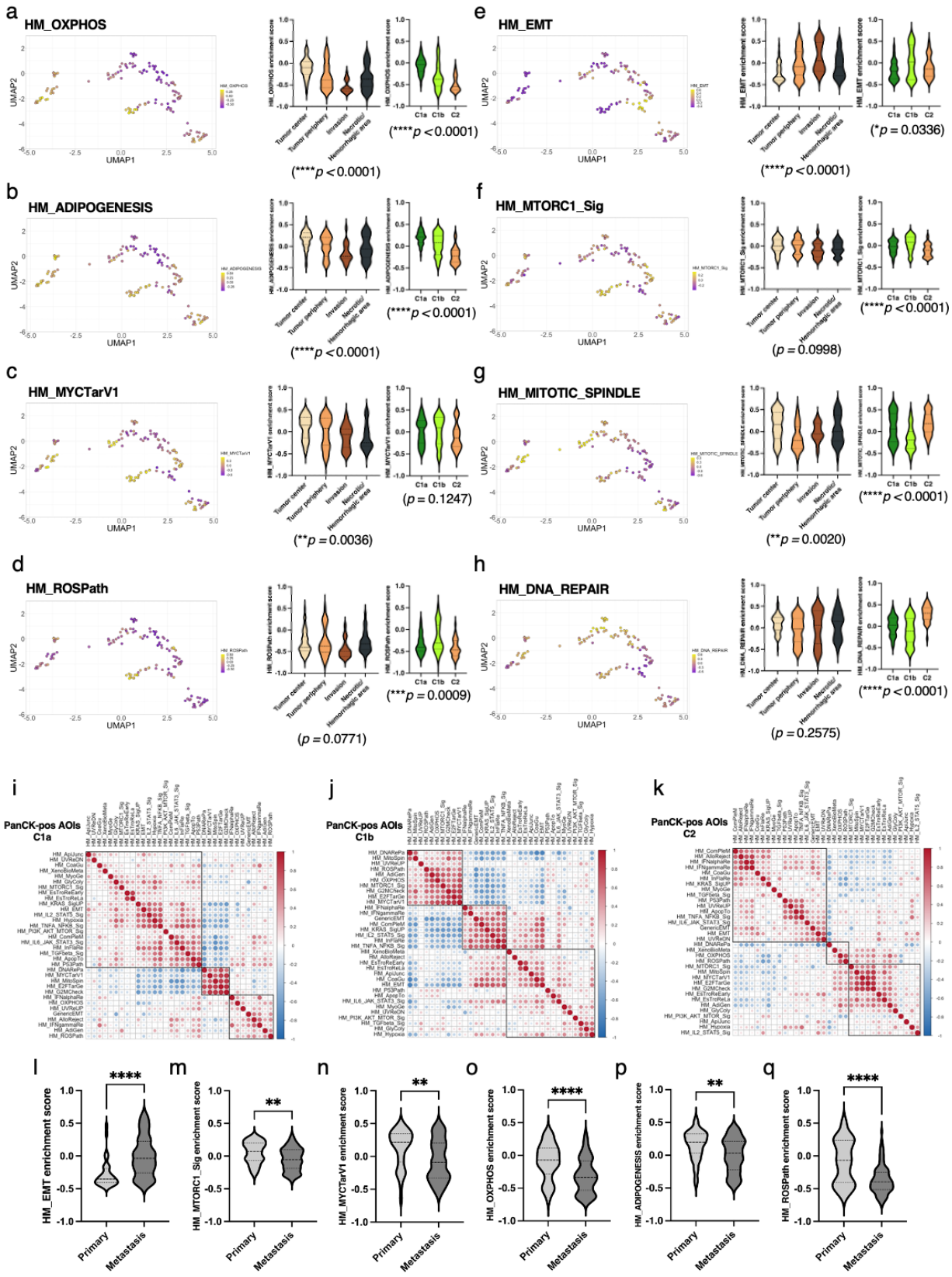
a
HM_OXPHOS
(****p < 0.0001)
(****p < 0.0001)
b
HM_ADIPOGENESIS
(****p < 0.0001)
(****p < 0.0001)
c
HM_MYCTarV1
(p = 0.1247)
(**p = 0.0036)
d
HM_ROSPath
(***p = 0.0009)
(p = 0.0771)
e
HM_EMT
(*p = 0.0336)
(****p < 0.0001)
f
HM_MTORC1_Sig
(****p < 0.0001)
(p = 0.0998)
g
HM_MITOTIC_SPINDLE
(****p < 0.0001)
(**p = 0.0020)
h
HM_DNA_REPAIR
(****p < 0.0001)
(p = 0.2575)
UMAP1
UMAP2
Tumor center
Tumor periphery
Invasion
Necrotic/ Hemorrhagic area
C1a
C1b
C2
i
PanCK-pos AOIs C1a
j
PanCK-pos AOIs C1b
k
PanCK-pos AOIs C2
l
HM_EMT enrichment score
****
m
HM_MTORC1_Sig enrichment score
**
n
HM_MYCTarV1 enrichment score
**
o
HM_OXPHOS enrichment score
****
p
HM_ADIPOGENESIS enrichment score
**
q
HM_ROSPath enrichment score
****
Primary
Metastasis

Fig. 3

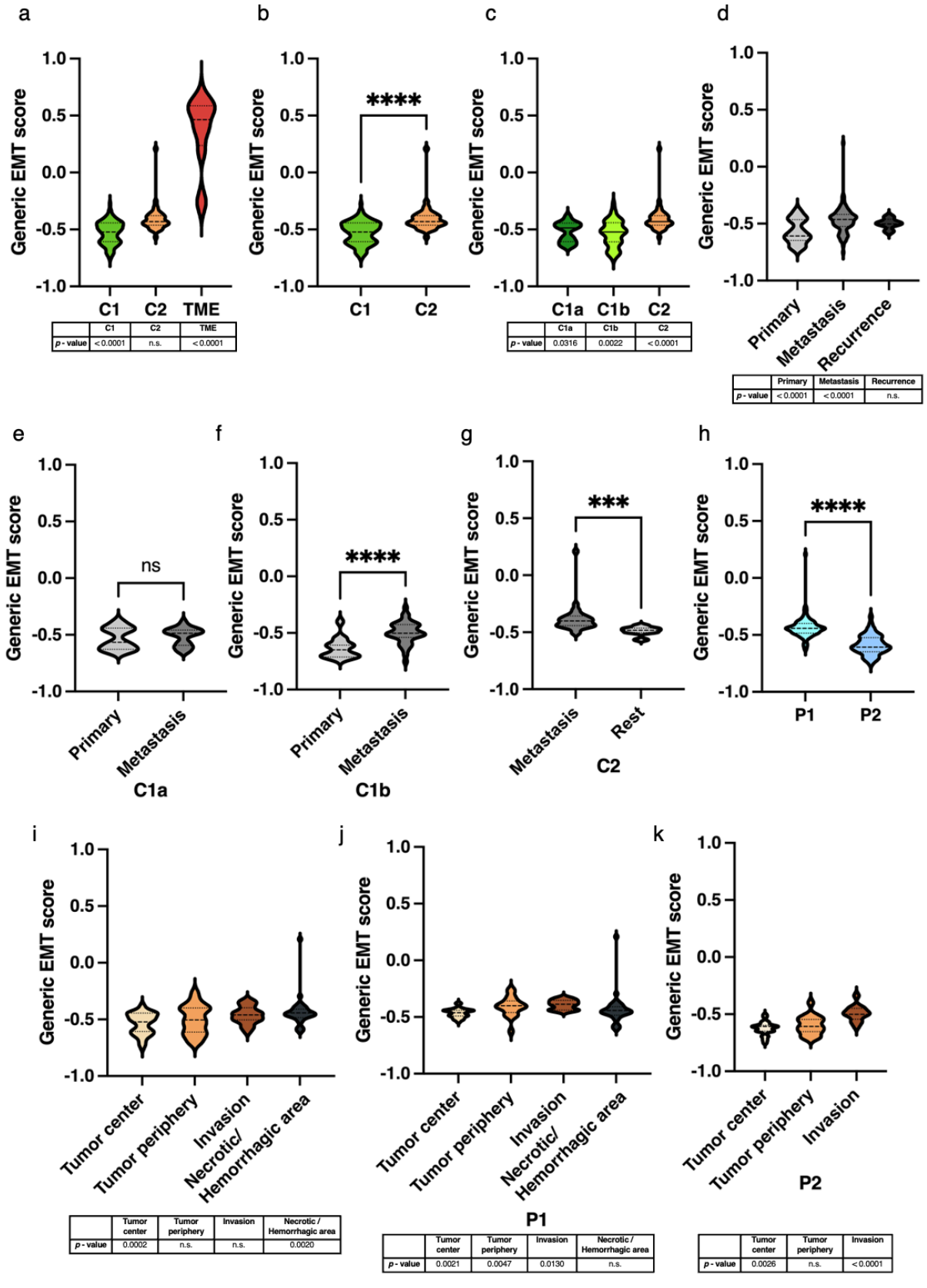

	C1	C2	TME
p - value	< 0.0001	n.s.	< 0.0001

	C1a	C1b	C2
p - value	0.0316	0.0022	< 0.0001

	Primary	Metastasis	Recurrence
p - value	< 0.0001	< 0.0001	n.s.

	Tumor center	Tumor periphery	Invasion	Necrotic / Hemorrhagic area
p - value	0.0002	n.s.	n.s.	0.0020

P1

	Tumor center	Tumor periphery	Invasion	Necrotic / Hemorrhagic area
p - value	0.0021	0.0047	0.0130	n.s.

P2

	Tumor center	Tumor periphery	Invasion
p - value	0.0026	n.s.	< 0.0001

Fig. 4

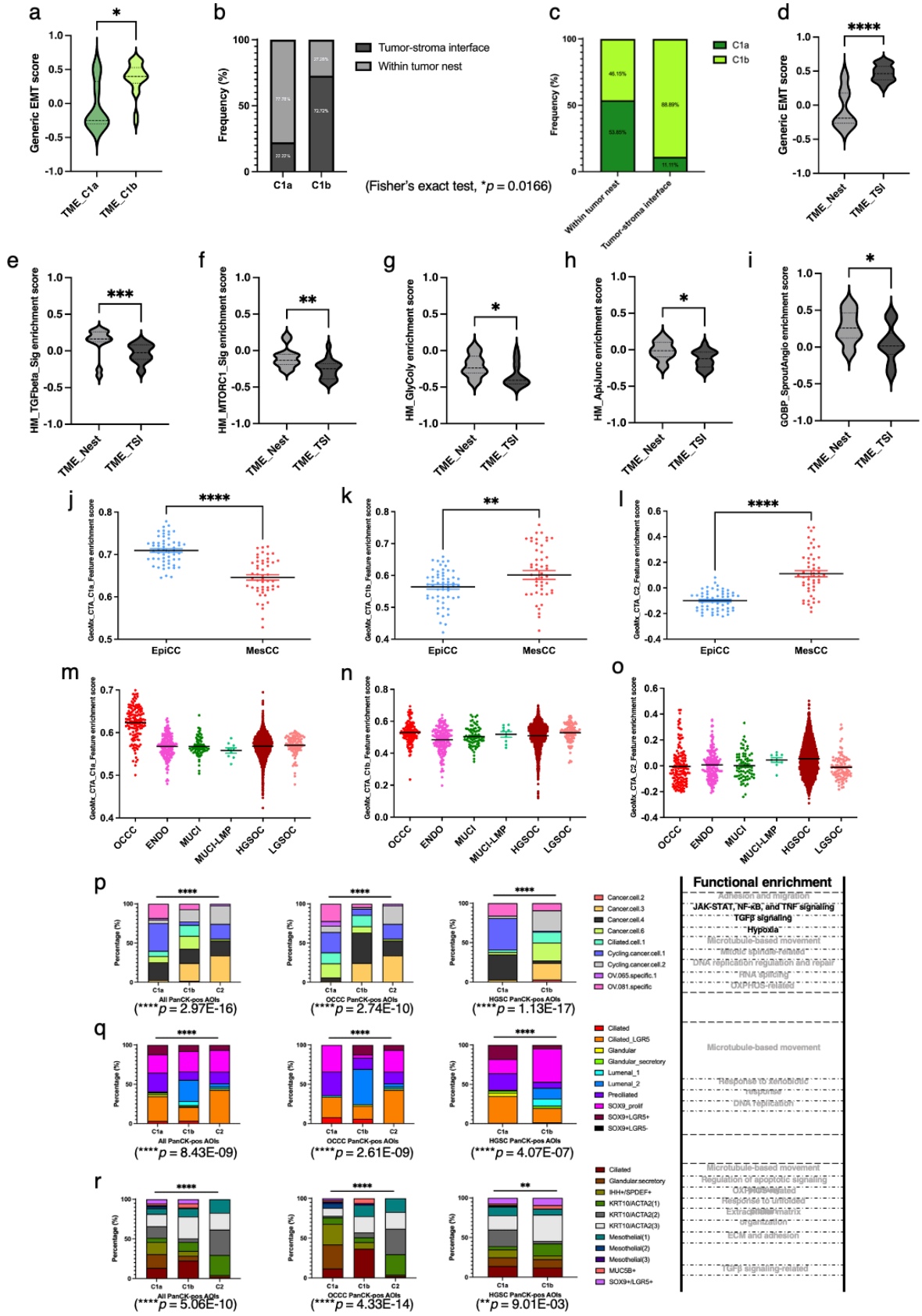
a
Generic EMT score
TME_C1a
TME_C1b
b
Frequency (%)
Tumor-stroma interface
Within tumor nest
C1a
C1b
(Fisher's exact test, *p = 0.0166)
c
Frequency (%)
C1a
C1b
Within tumor nest
Tumor-stroma interface
d
Generic EMT score
TME_Nest
TME_TSI
e
HM_TGFbeta_Sig enrichment score
f
HM_MTORC1_Sig enrichment score
g
HM_GlyColy enrichment score
h
HM_Apj.Junc enrichment score
i
GOBP_SproutAngio enrichment score
j
GeoMx_CTA_C1a_Feature enrichment score
EpiCC
MesCC
k
GeoMx_CTA_C1b_Feature enrichment score
l
GeoMx_CTA_C2_Feature enrichment score
m
GeoMx_CTA_C1a_Feature enrichment score
OCCC
ENDO
MUCI
MUCI-LMP
HGSOC
LGSOC
n
GeoMx_CTA_C1b_Feature enrichment score
o
GeoMx_CTA_C2_Feature enrichment score
p
Percentage (%)
All PanCK-pos AOIs
(****p = 2.97E-16)
OCCC PanCK-pos AOIs
(****p = 2.74E-10)
HGSC PanCK-pos AOIs
(****p = 1.13E-17)
Cancer.cell.2
Cancer.cell.3
Cancer.cell.4
Cancer.cell.6
Ciliated.cell.1
Cycling.cancer.cell.1
Cycling.cancer.cell.2
OV.065.specific.1
OV.081.specific
q
(****p = 8.43E-09)
(****p = 2.61E-09)
(****p = 4.07E-07)
Ciliated
Ciliated_LGR5
Glandular
Glandular_secretory
Lumenal_1
Lumenal_2
Preciliated
SOX9_prolif
SOX9+LGR5+
SOX9+LGR5-
r
(****p = 5.06E-10)
(****p = 4.33E-14)
(**p = 9.01E-03)
Ciliated
Glandular.secretory
IHH+/SPDEF+
KRT10/ACTA2(1)
KRT10/ACTA2(2)
KRT10/ACTA2(3)
Mesothelia(1)
Mesothelia(2)
Mesothelia(3)
MUC5B+
SOX9+/LGR5+
Functional enrichment
JAK-STAT, NF-κB, and TNF signaling
TGFβ signaling
Hypoxia
Microtubule-based movement
DNA replication
Microtubule-based movement
Response to antibiotic
DNA replication
Microtubule-based movement
Regulation of apoptotic signaling
ECM and adhesion
TGFβ signaling-related

Fig. 5

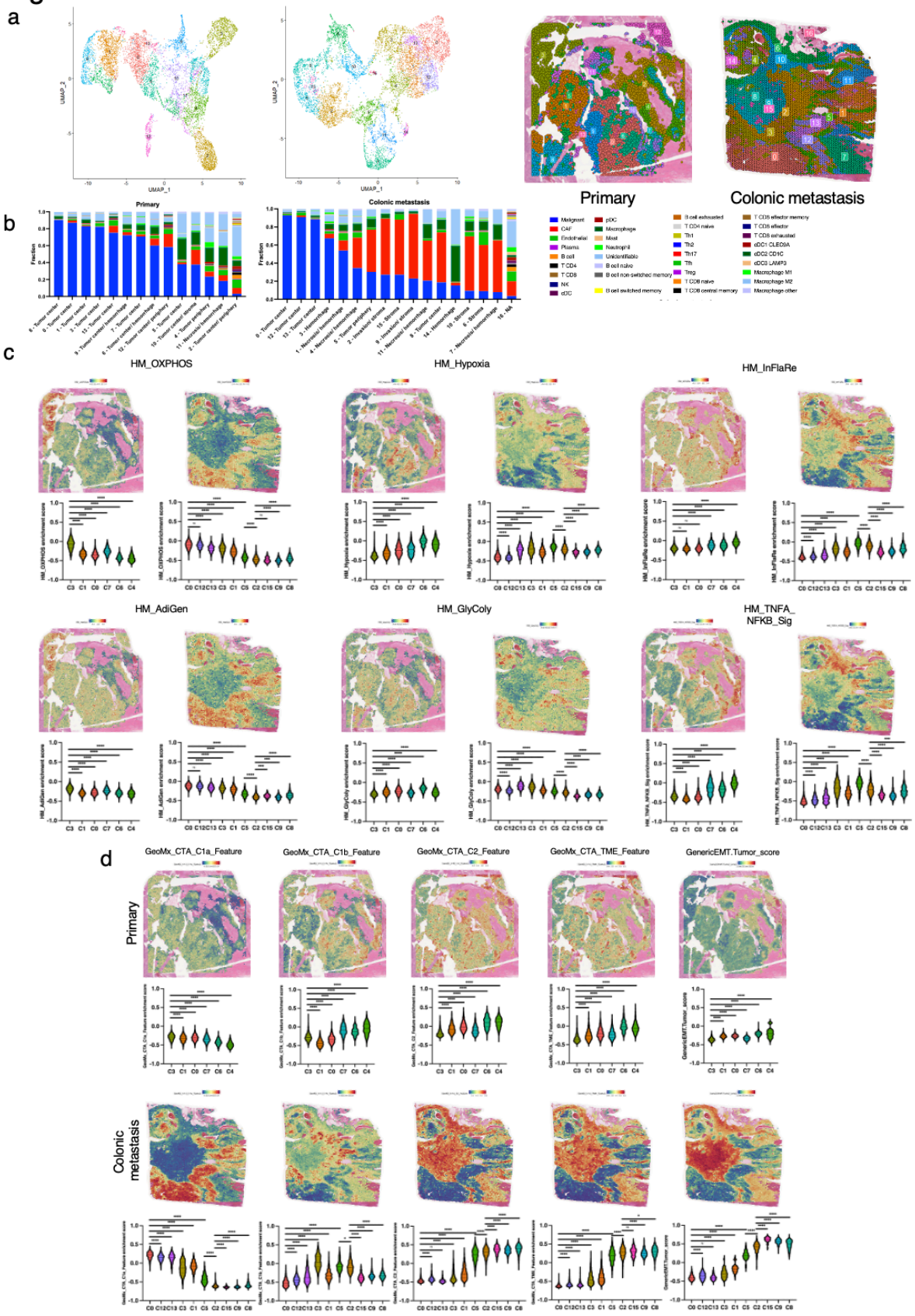
a
UMAP_1
UMAP_2
Primary
Colonic metastasis
b
Fraction
c
HM_OXPHOS
HM_Hypoxia
HM_InFlaRe
HM_AdiGen
HM_GlyColy
HM_TNFA_
NFKB_Sig
d
GeoMx_CTA_C1a_Feature
GeoMx_CTA_C1b_Feature
GeoMx_CTA_C2_Feature
GeoMx_CTA_TME_Feature
GenericEMT.Tumor_score
Primary
Colonic
metastasis

Fig. 6

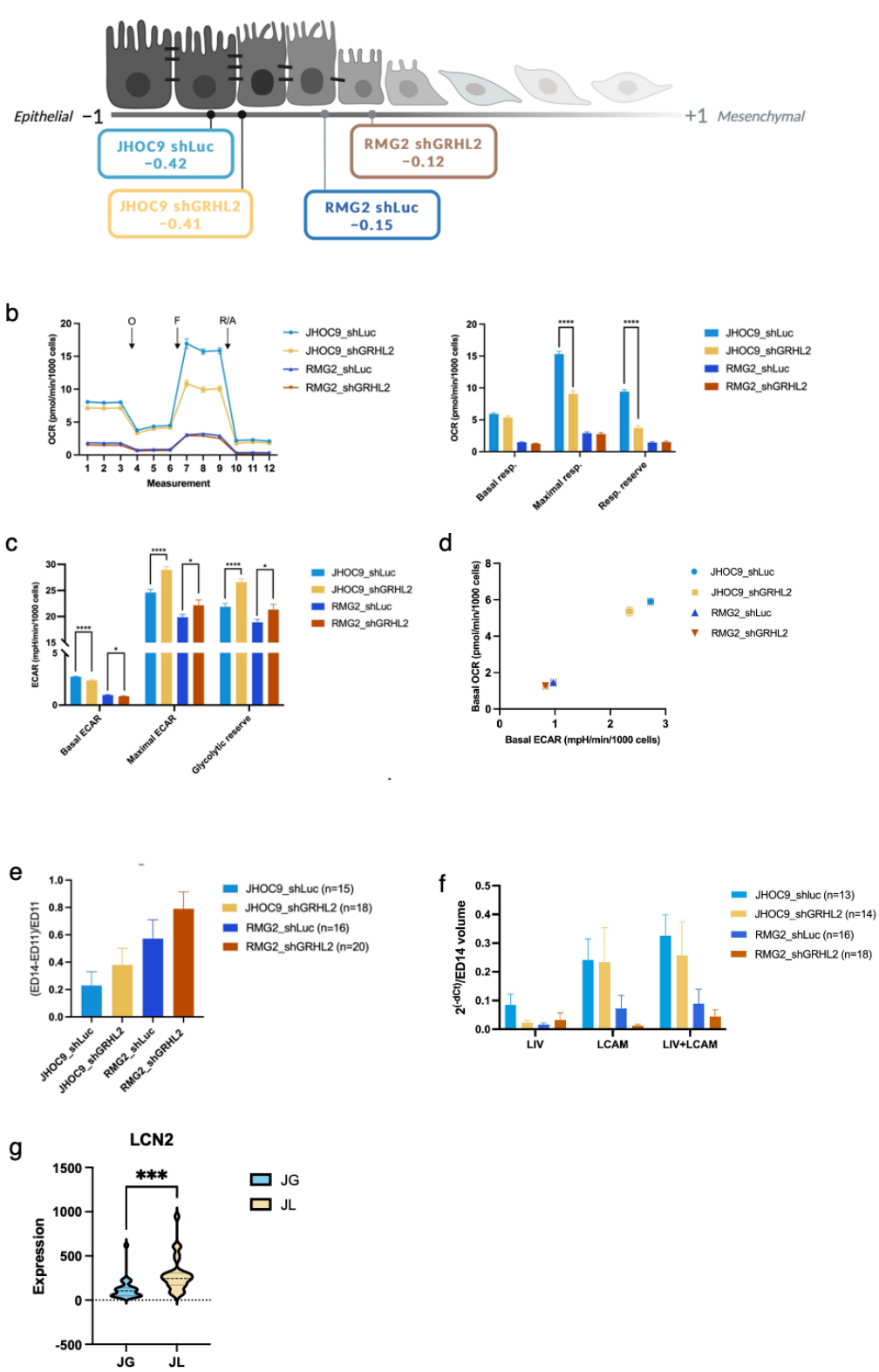
a
Epithelial −1
+1 Mesenchymal
JHOC9 shLuc −0.42
JHOC9 shGRHL2 −0.41
RMG2 shLuc −0.15
RMG2 shGRHL2 −0.12
b
OCR (pmol/min/1000 cells)
Measurement
O
F
R/A
JHOC9_shLuc
JHOC9_shGRHL2
RMG2_shLuc
RMG2_shGRHL2
Basal resp.
Maximal resp.
Resp. reserve
c
ECAR (mpH/min/1000 cells)
Basal ECAR
Maximal ECAR
Glycolytic reserve
d
Basal OCR (pmol/min/1000 cells)
Basal ECAR (mpH/min/1000 cells)
e
(ED14-ED11)/ED11
JHOC9_shLuc (n=15)
JHOC9_shGRHL2 (n=18)
RMG2_shLuc (n=16)
RMG2_shGRHL2 (n=20)
f
2^(-dCt)/ED14 volume
JHOC9_shluc (n=13)
JHOC9_shGRHL2 (n=14)
RMG2_shLuc (n=16)
RMG2_shGRHL2 (n=18)
LIV
LCAM
LIV+LCAM
g
LCN2
Expression
JG
JL

Fig. 7

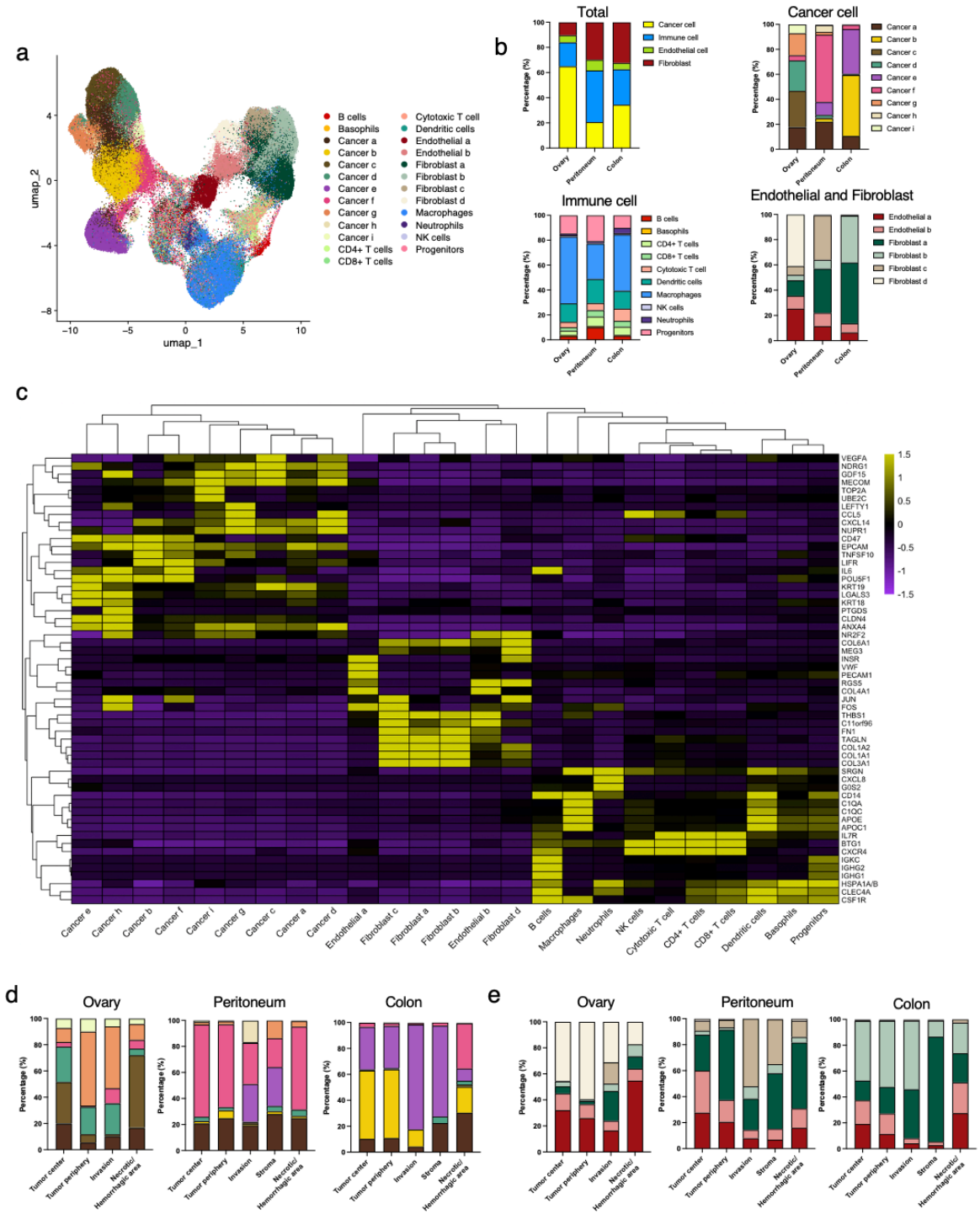
a
umap_1
umap_2
B cells
Basophils
Cancer a
Cancer b
Cancer c
Cancer d
Cancer e
Cancer f
Cancer g
Cancer h
Cancer i
CD4+ T cells
CD8+ T cells
Cytotoxic T cell
Dendritic cells
Endothelial a
Endothelial b
Fibroblast a
Fibroblast b
Fibroblast c
Fibroblast d
Macrophages
Neutrophils
NK cells
Progenitors
b
Total
Cancer cell
Immune cell
Endothelial cell
Fibroblast
Cancer cell
Immune cell
Endothelial and Fibroblast
Percentage (%)
Ovary
Peritoneum
Colon
c
VEGFA
NDRG1
GDF15
MECOM
TOP2A
UBE2C
LEFTY1
CCL5
CXCL14
NUPR1
CD47
EPCAM
TNFSF10
LIFR
IL6
POU5F1
KRT19
LGALS3
KRT18
PTGDS
CLDN4
ANXA4
NR2F2
COL6A1
MEG3
INSR
VWF
PECAM1
RGS5
COL4A1
JUN
FOS
THBS1
C1orf96
FN1
TAGLN
COL1A2
COL1A1
COL3A1
SRGN
CXCL8
G0S2
CD14
C1QA
C1QC
APOE
APOC1
IL7R
BTG1
CXCR4
IGKC
IGHG2
IGHG1
HSPA1A/B
CLEC4A
CSF1R
d
e
Tumor center
Tumor periphery
Invasion
Stroma
Necrotic/ Hemorrhagic area

Fig. 8

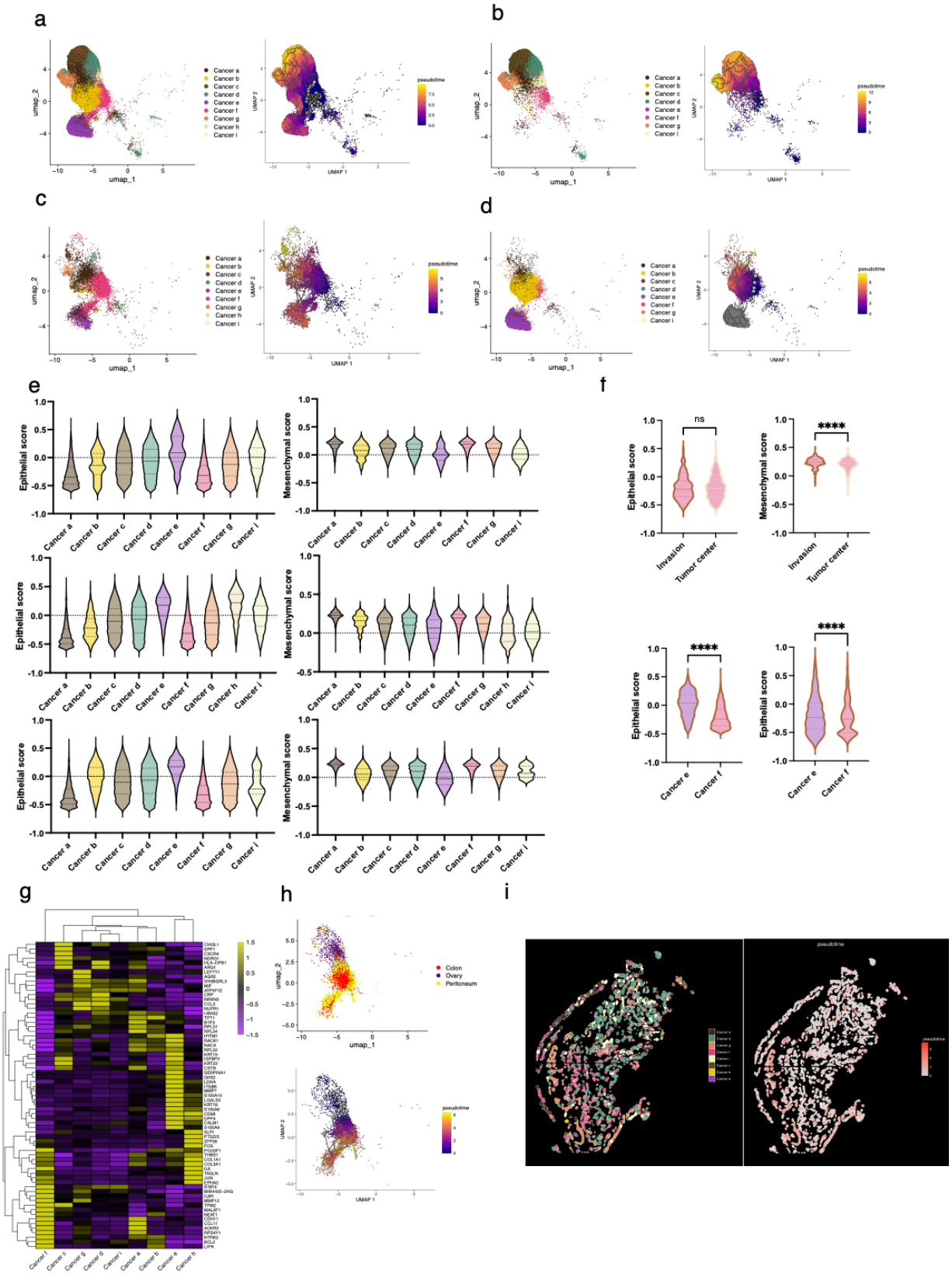
a
b
c
d
e
f
g
h
i
umap_1
umap_2
UMAP 1
UMAP 2
pseudotime
Cancer a
Cancer b
Cancer c
Cancer d
Cancer e
Cancer f
Cancer g
Cancer h
Cancer i
Epithelial score
Mesenchymal score
ns
****
Invasion
Tumor center
Colon
Ovary
Peritoneum

Fig. 9

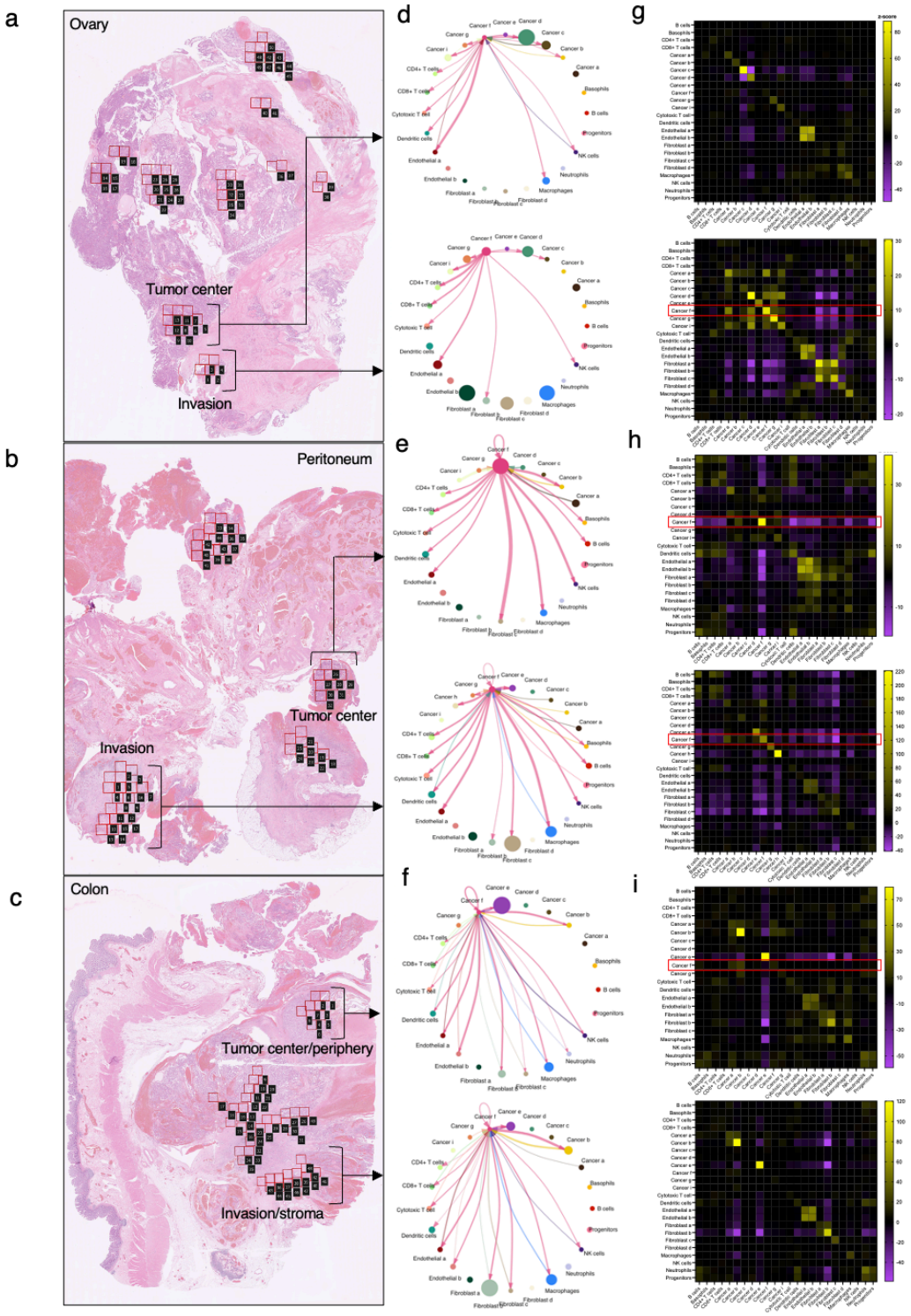
a
Ovary
Tumor center
Invasion
b
Peritoneum
Tumor center
Invasion
c
Colon
Tumor center/periphery
Invasion/stroma
d
e
f
g
h
i

Fig. 10

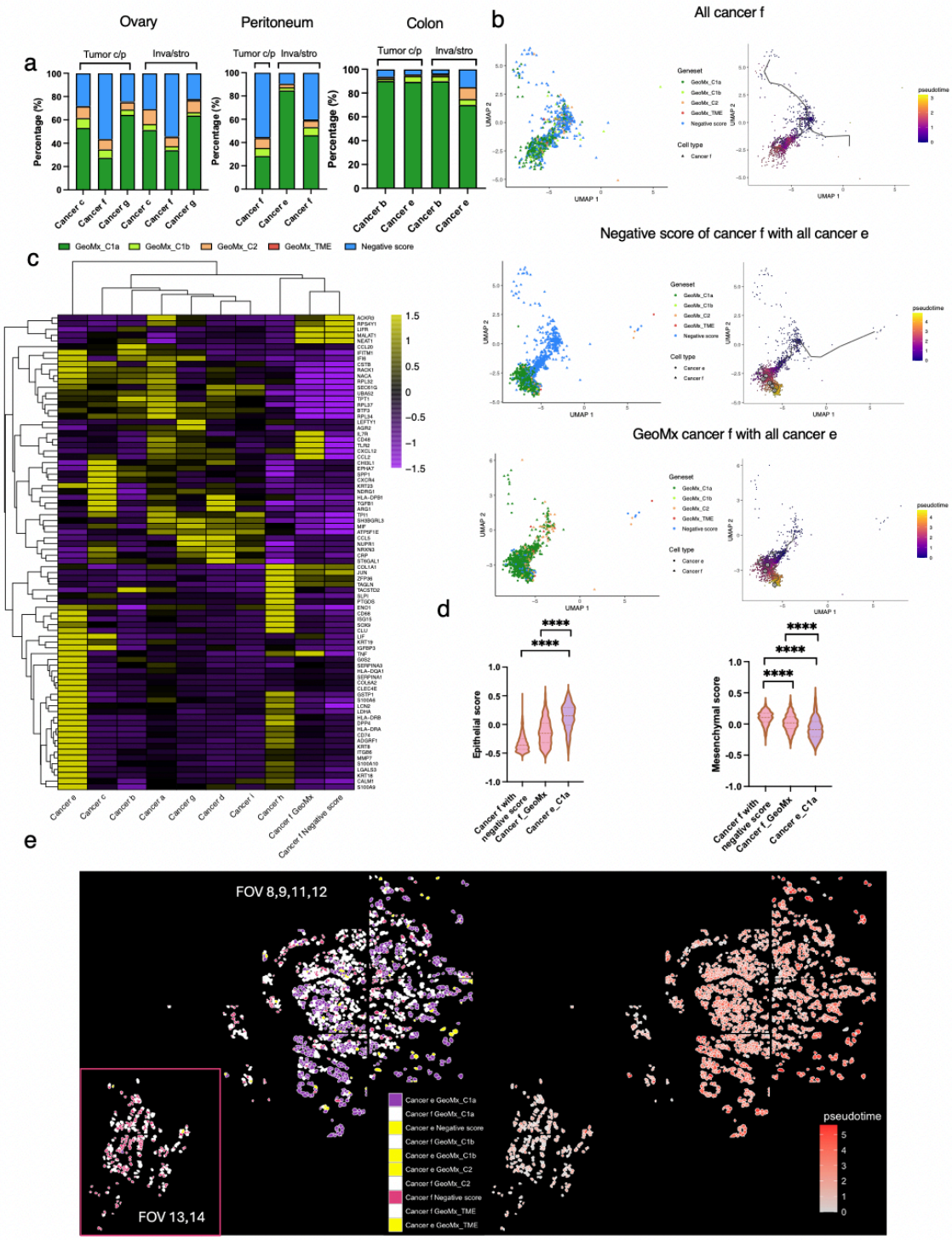
a
Ovary
Peritoneum
Colon
Tumor c/p
Inva/stro
Percentage (%)
Cancer c
Cancer f
Cancer g
Cancer e
Cancer b
GeoMx_C1a
GeoMx_C1b
GeoMx_C2
GeoMx_TME
Negative score
b
All cancer f
Negative score of cancer f with all cancer e
GeoMx cancer f with all cancer e
UMAP 1
UMAP 2
pseudotime
c
d
Epithelial score
Mesenchymal score
Cancer f with negative score
Cancer f_GeoMx
Cancer e_C1a
****
e
FOV 8,9,11,12
FOV 13,14
Cancer e GeoMx_C1a
Cancer f GeoMx_C1a
Cancer e Negative score
Cancer f GeoMx_C1b
Cancer e GeoMx_C1b
Cancer e GeoMx_C2
Cancer f GeoMx_C2
Cancer f Negative score
Cancer f GeoMx_TME
Cancer e GeoMx_TME
pseudotime

Fig. 11

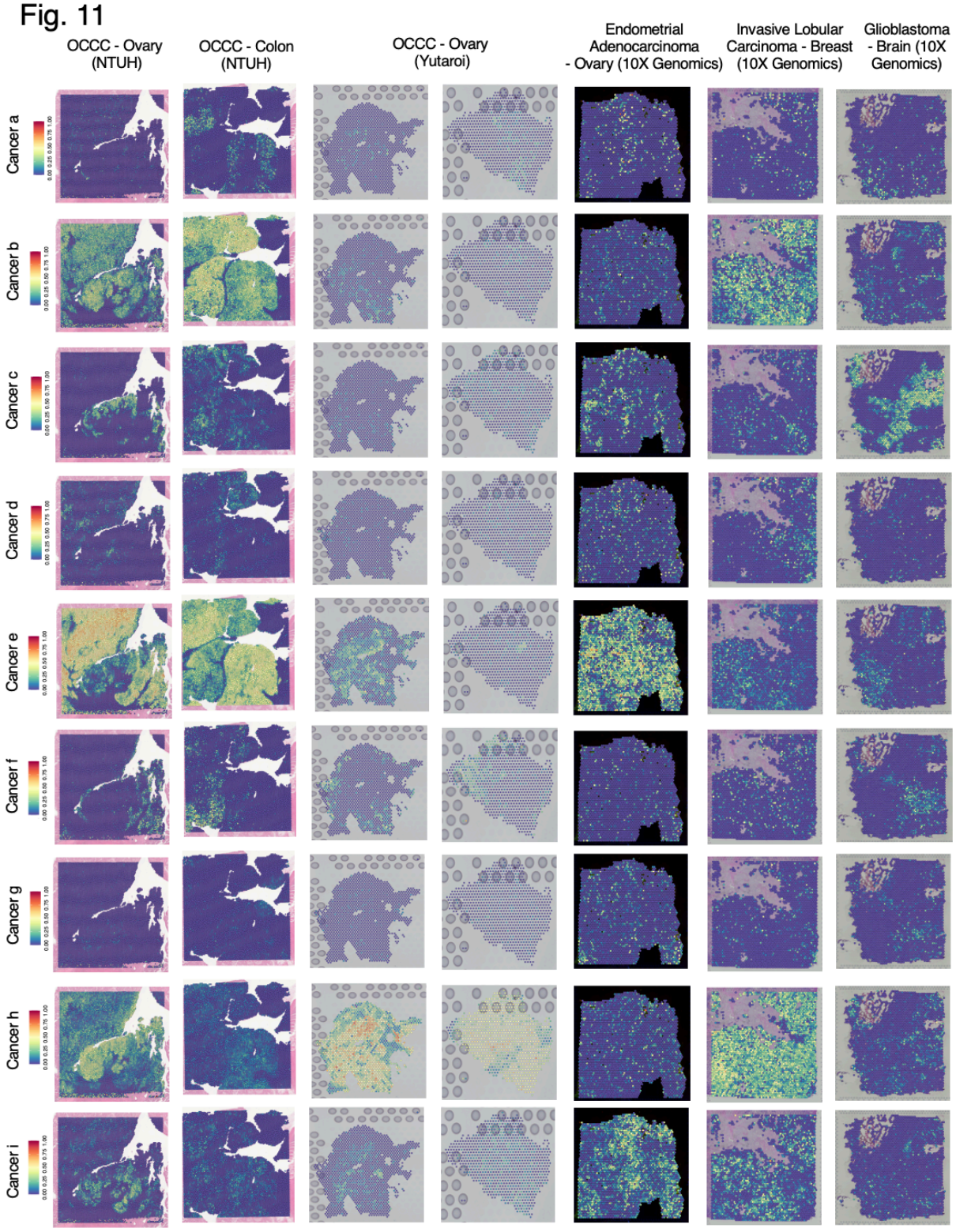
OCCC - Ovary (NTUH)
OCCC - Colon (NTUH)
OCCC - Ovary (Yutaroi)
Endometrial Adenocarcinoma - Ovary (10X Genomics)
Invasive Lobular Carcinoma - Breast (10X Genomics)
Glioblastoma - Brain (10X Genomics)
Cancer a
Cancer b
Cancer c
Cancer d
Cancer e
Cancer f
Cancer g
Cancer h
Cancer i

Fig. 12

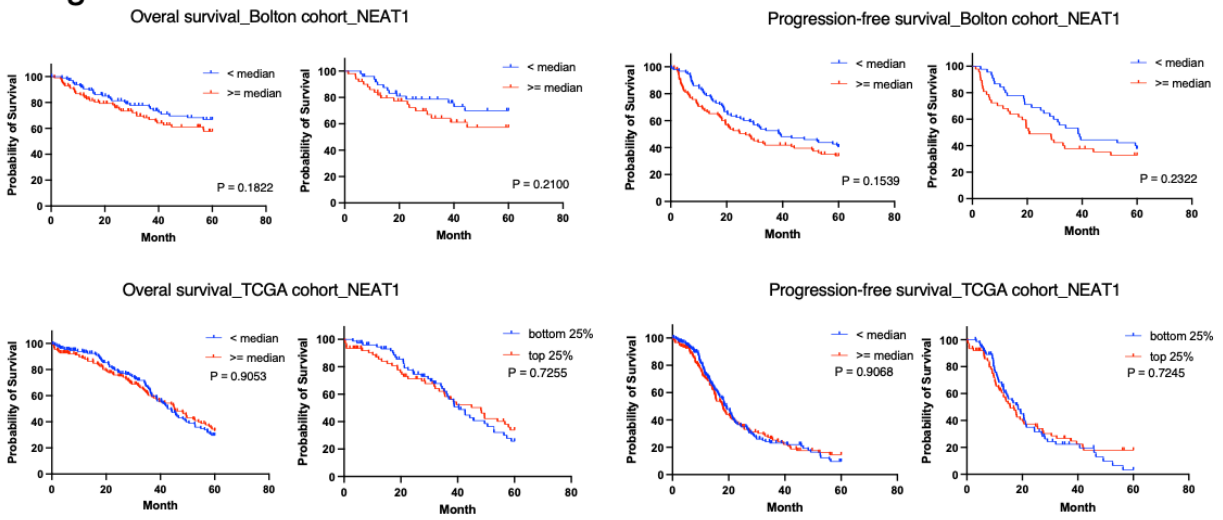

Tabel 1. Cox regression analysis for NEAT1 among different cancer types in the TCGA PanCaner dataset

Disease	Sample	OS.Cox.Reg	OS.Cox.p	PFS.Cox.Reg	PFS.Cox.p
ACC	79	-0.12416	0.372342	-0.13812	0.235638
BLCA	**407**	**-0.16557**	**0.010891**	**-0.17681**	**0.00869**
BRCA	1092	-0.02281	0.728982	-0.04084	0.539822
CESC	304	0.011675	0.926608	0.082961	0.49964
CHOL	36	-0.0655	0.833222	-0.03372	0.902614
COADREAD	376	0.059987	0.580106	0.226145	0.022629
DLBC	48	-0.00819	0.981614	0.332438	0.36598
ESCA	184	-0.01	0.931937	-0.16374	0.127359
GBMLGG	**666**	**0.373759**	**7.57E-14**	**0.338892**	**1.54E-13**
HNSC	519	-0.06452	0.252566	0.003337	0.954128
KICH	65	-0.38282	0.298648	-0.3369	0.31148
KIRC	**533**	**0.159397**	**0.002319**	-0.04783	0.374411
KIRP	289	-0.02159	0.850569	0.001065	0.991603
LAML	161	0.029193	0.788209	0	1
LIHC	**370**	**-0.16932**	**0.02904**	-0.02549	0.71085
LUAD	506	-0.07086	0.200197	-0.03015	0.563227
LUSC	495	-0.0138	0.789635	0.082551	0.191302
MESO	86	-0.09171	0.514309	-0.01088	0.944619
OV	302	0.002049	0.971014	-0.03748	0.467598
PAAD	178	0.032711	0.664131	-0.00604	0.932184
PCPG	179	0.283667	0.416296	0.126052	0.500649
PRAD	497	0.081234	0.761683	**0.225939**	**0.008925**
SARC	259	-0.0723	0.311028	-0.00908	0.882699
SKCM	103	0.117559	0.297856	0.085717	0.40569
STAD	409	-0.01388	0.845556	0.041729	0.588001
TGCT	**134**	**0.944871**	**0.099616**	-0.07843	0.634106
THCA	501	-0.19361	0.430432	0.129205	0.339657
THYM	**119**	**0.879377**	**0.01268**	0.232836	0.22207
UCEC	**175**	**0.318342**	**0.019909**	0.154256	0.186807
UCS	57	0.124598	0.40646	0.063077	0.661721
UVM	80	0.110632	0.415881	0.113791	0.325299

S. Fig. 1

a

C1a vs REST

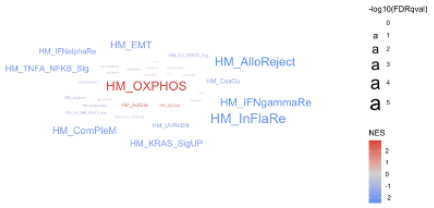

Significantly more enriched: OXPHOS
Significantly less enriched: AlloReject, IFNgammaRe, InFlaRe, TNFA_NFKB_Sig, KRAS_SigUP, ComPleM, IFNalphaRe, EMT

b

C1b vs REST

Significantly more enriched:
TNFA_NFKB_Sig, ApopTo, EsTroReEarly

c

C2 vs REST

Significantly more enriched: DNARePa, E2FTarGe

d

TME vs REST

Significantly more enriched: AlloReject, IFNgammaRe, KRAS_SigUP, EMT, ComPleM
Significantly less enriched: OXPHOS, EsTroReEarly, MYCTarV1, E2FTarGe, EsTroReLa

e

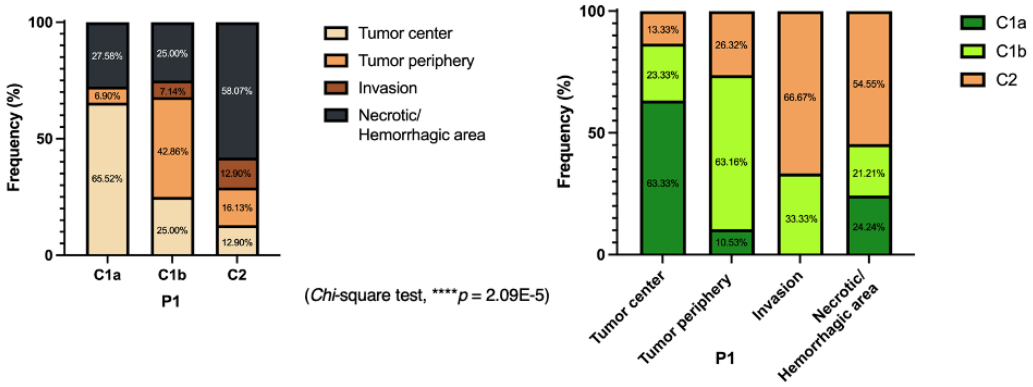

f

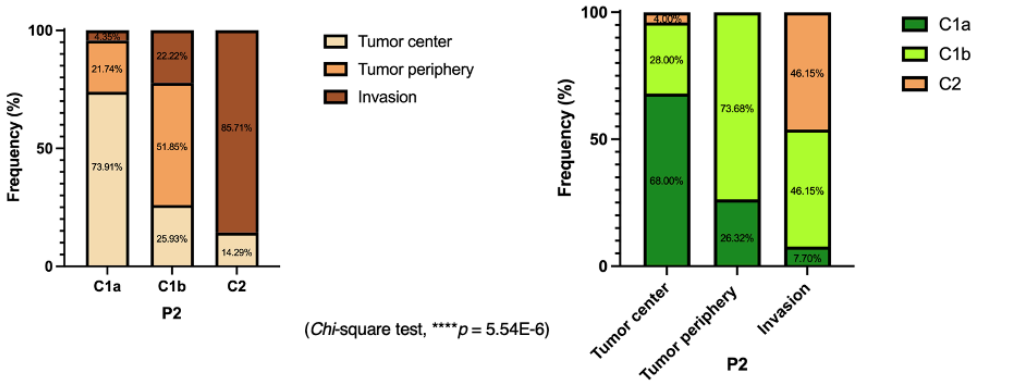

S. Fig. 2

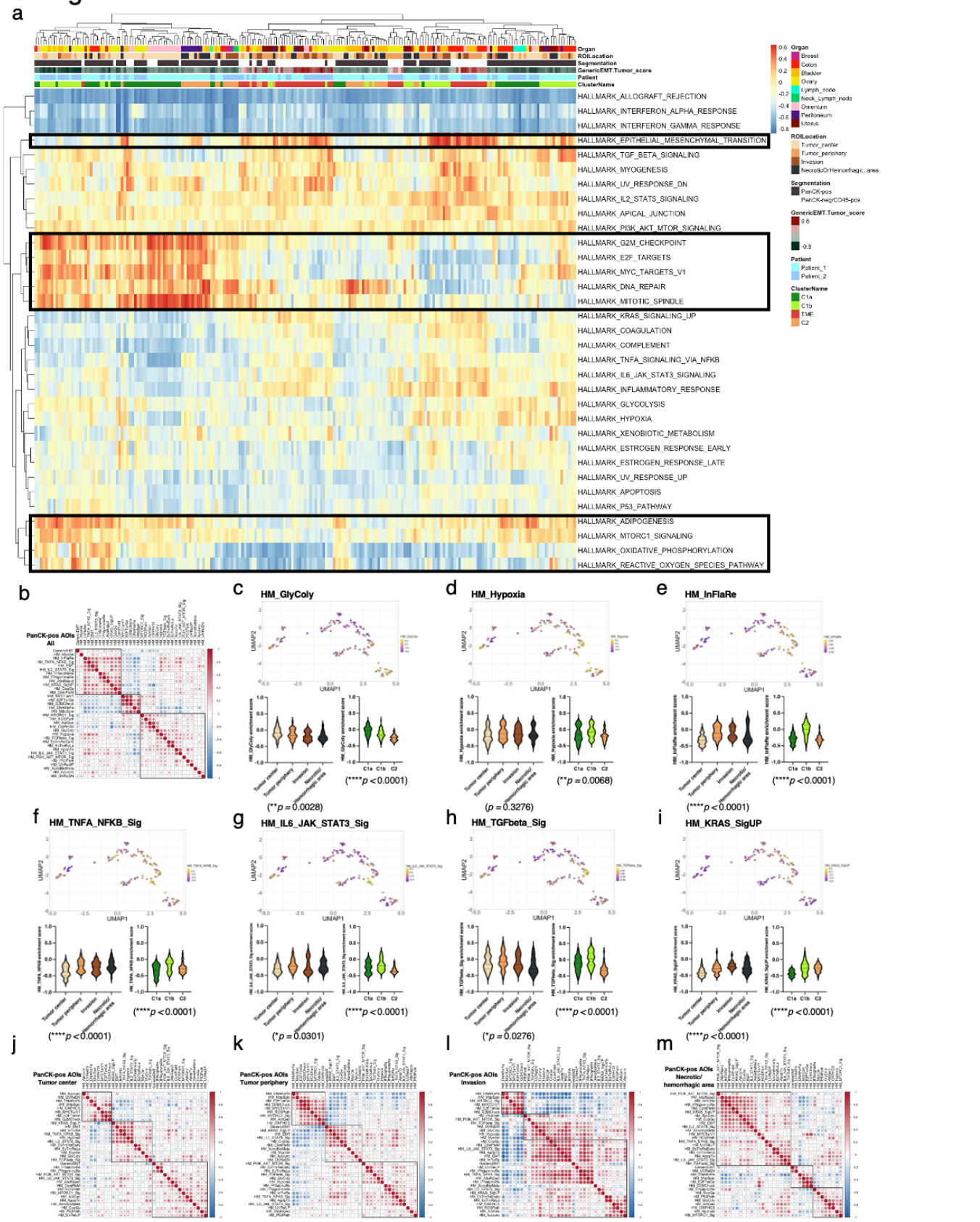
a
Organ
ROILocation
Segmentation
GenericEMT.Tumor_score
Patient
ClusterName
HALLMARK_ALLOGRAFT_REJECTION
HALLMARK_INTERFERON_ALPHA_RESPONSE
HALLMARK_INTERFERON_GAMMA_RESPONSE
HALLMARK_EPITHELIAL_MESENCHYMAL_TRANSITION
HALLMARK_TGF_BETA_SIGNALING
HALLMARK_MYOGENESIS
HALLMARK_UV_RESPONSE_DN
HALLMARK_IL2_STAT5_SIGNALING
HALLMARK_APICAL_JUNCTION
HALLMARK_PI3K_AKT_MTOR_SIGNALING
HALLMARK_G2M_CHECKPOINT
HALLMARK_E2F_TARGETS
HALLMARK_MYC_TARGETS_V1
HALLMARK_DNA_REPAIR
HALLMARK_MITOTIC_SPINDLE
HALLMARK_KRAS_SIGNALING_UP
HALLMARK_COAGULATION
HALLMARK_COMPLEMENT
HALLMARK_TNFA_SIGNALING_VIA_NFKB
HALLMARK_IL6_JAK_STAT3_SIGNALING
HALLMARK_INFLAMMATORY_RESPONSE
HALLMARK_GLYCOLYSIS
HALLMARK_HYPOXIA
HALLMARK_XENOBIOTIC_METABOLISM
HALLMARK_ESTROGEN_RESPONSE_EARLY
HALLMARK_ESTROGEN_RESPONSE_LATE
HALLMARK_UV_RESPONSE_UP
HALLMARK_APOPTOSIS
HALLMARK_P53_PATHWAY
HALLMARK_ADIPOGENESIS
HALLMARK_MTORC1_SIGNALING
HALLMARK_OXIDATIVE_PHOSPHORYLATION
HALLMARK_REACTIVE_OXYGEN_SPECIES_PATHWAY
Organ
Breast
Colon
Bladder
Ovary
Lymph_node
Neck_Lymph_node
Omentum
Peritoneum
Uterus
ROILocation
Tumor_center
Tumor_periphery
Invasion
NecroticOrHemorrhagic_area
Segmentation
PanCK-pos
PanCK-neg/CD45-pos
GenericEMT.Tumor_score
Patient
Patient_1
Patient_2
ClusterName
C1a
C1b
TME
C2
b
PanCK-pos AOIs
All
c
HM_GlyColy
(****p < 0.0001)
d
HM_Hypoxia
(**p = 0.0068)
e
HM_InFlaRe
(****p < 0.0001)
f
HM_TNFA_NFKB_Sig
(**p = 0.0028)
(****p < 0.0001)
g
HM_IL6_JAK_STAT3_Sig
(****p < 0.0001)
(*p = 0.0301)
h
HM_TGFbeta_Sig
(p = 0.3276)
(****p < 0.0001)
(*p = 0.0276)
i
HM_KRAS_SigUP
(****p < 0.0001)
(****p < 0.0001)
j
PanCK-pos AOIs
Tumor center
k
PanCK-pos AOIs
Tumor periphery
l
PanCK-pos AOIs
Invasion
m
PanCK-pos AOIs
Necrotic/
hemorrhagic area

S. Fig. 3

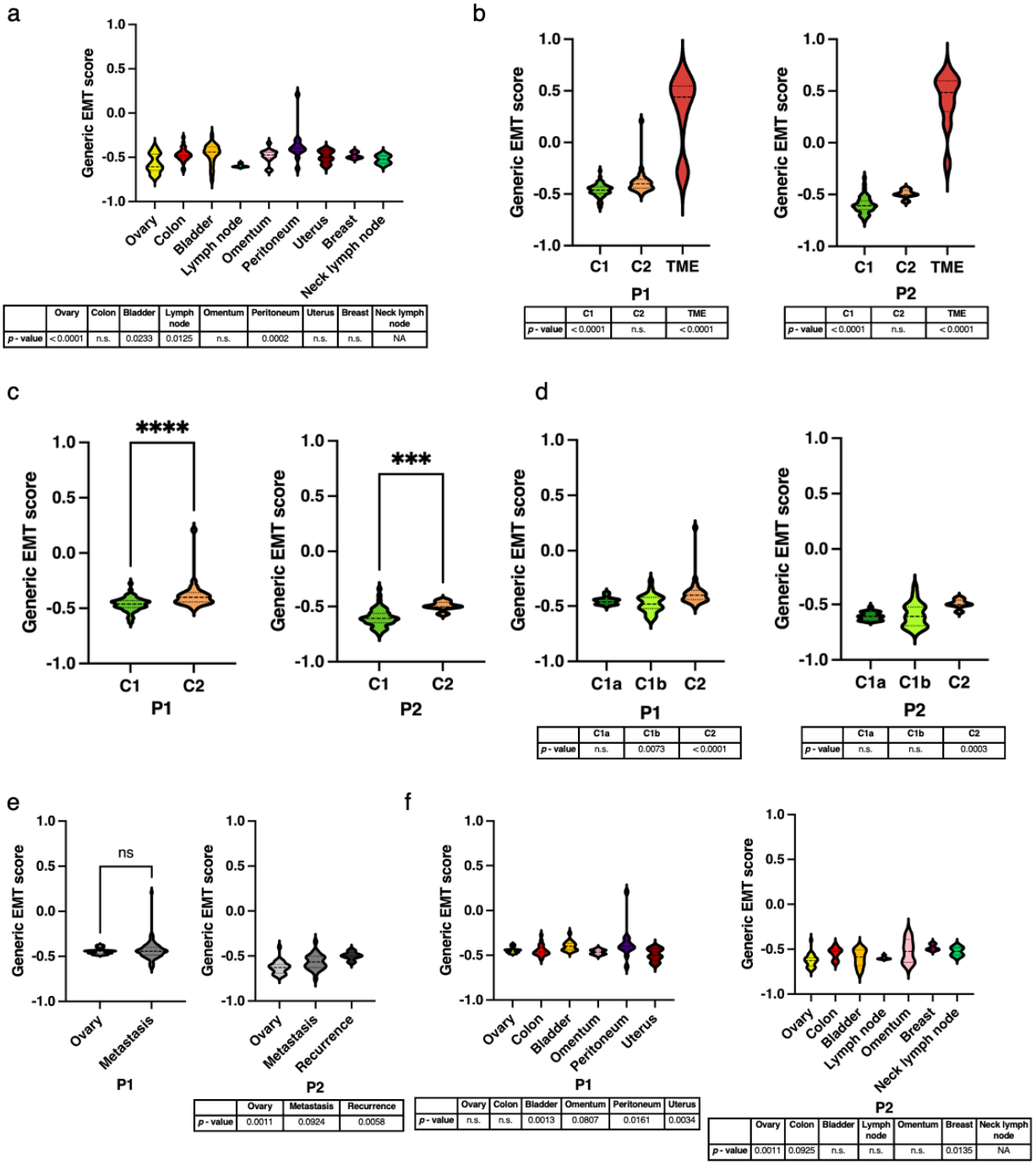

	Ovary	Colon	Bladder	Lymph node	Omentum	Peritoneum	Uterus	Breast	Neck lymph node
p - value	< 0.0001	n.s.	0.0233	0.0125	n.s.	0.0002	n.s.	n.s.	NA

	C1	C2	TME
p - value	< 0.0001	n.s.	< 0.0001

	C1	C2	TME
p - value	< 0.0001	n.s.	< 0.0001

	C1a	C1b	C2
p - value	n.s.	0.0073	< 0.0001

	C1a	C1b	C2
p - value	n.s.	n.s.	0.0003

	Ovary	Metastasis	Recurrence
p - value	0.0011	0.0924	0.0058

	Ovary	Colon	Bladder	Omentum	Peritoneum	Uterus
p - value	n.s.	n.s.	0.0013	0.0807	0.0161	0.0034

	Ovary	Colon	Bladder	Lymph node	Omentum	Breast	Neck lymph node
p - value	0.0011	0.0925	n.s.	n.s.	n.s.	0.0135	NA

S. Fig. 4

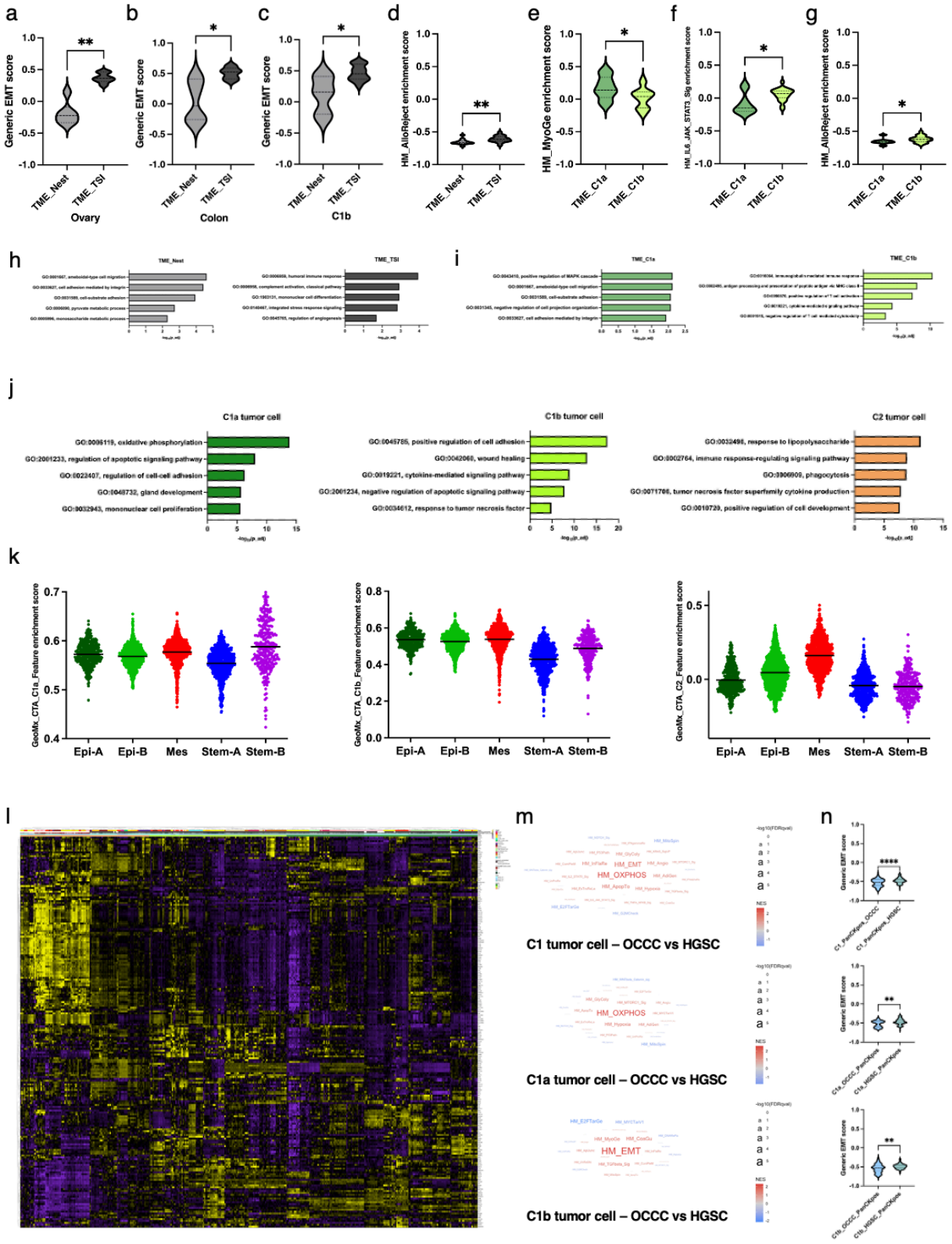
a
b
c
d
e
f
g
Generic EMT score
HM_AlloReject enrichment score
HM_MyoGe enrichment score
HM_IL6_JAK_STAT3_Sig enrichment score
TME_Nest
TME_TSI
TME_C1a
TME_C1b
Ovary
Colon
C1b
h
i
TME_Nest
TME_TSI
TME_C1a
TME_C1b
j
C1a tumor cell
C1b tumor cell
C2 tumor cell
GO:0006119, oxidative phosphorylation
GO:2001233, regulation of apoptotic signaling pathway
GO:0022407, regulation of cell-cell adhesion
GO:0048732, gland development
GO:0032943, mononuclear cell proliferation
GO:0045785, positive regulation of cell adhesion
GO:0042060, wound healing
GO:0019221, cytokine-mediated signaling pathway
GO:2001234, negative regulation of apoptotic signaling pathway
GO:0034612, response to tumor necrosis factor
GO:0032496, response to lipopolysaccharide
GO:0002764, immune response-regulating signaling pathway
GO:0006909, phagocytosis
GO:0071706, tumor necrosis factor superfamily cytokine production
GO:0010729, positive regulation of cell development
k
GeoMx_CTA_C1a_Feature enrichment score
GeoMx_CTA_C1b_Feature enrichment score
GeoMx_CTA_C2_Feature enrichment score
Epi-A
Epi-B
Mes
Stem-A
Stem-B
l
m
HM_EMT
HM_OXPHOS
C1 tumor cell – OCCC vs HGSC
C1a tumor cell – OCCC vs HGSC
C1b tumor cell – OCCC vs HGSC
n
Generic EMT score

S. Fig. 5

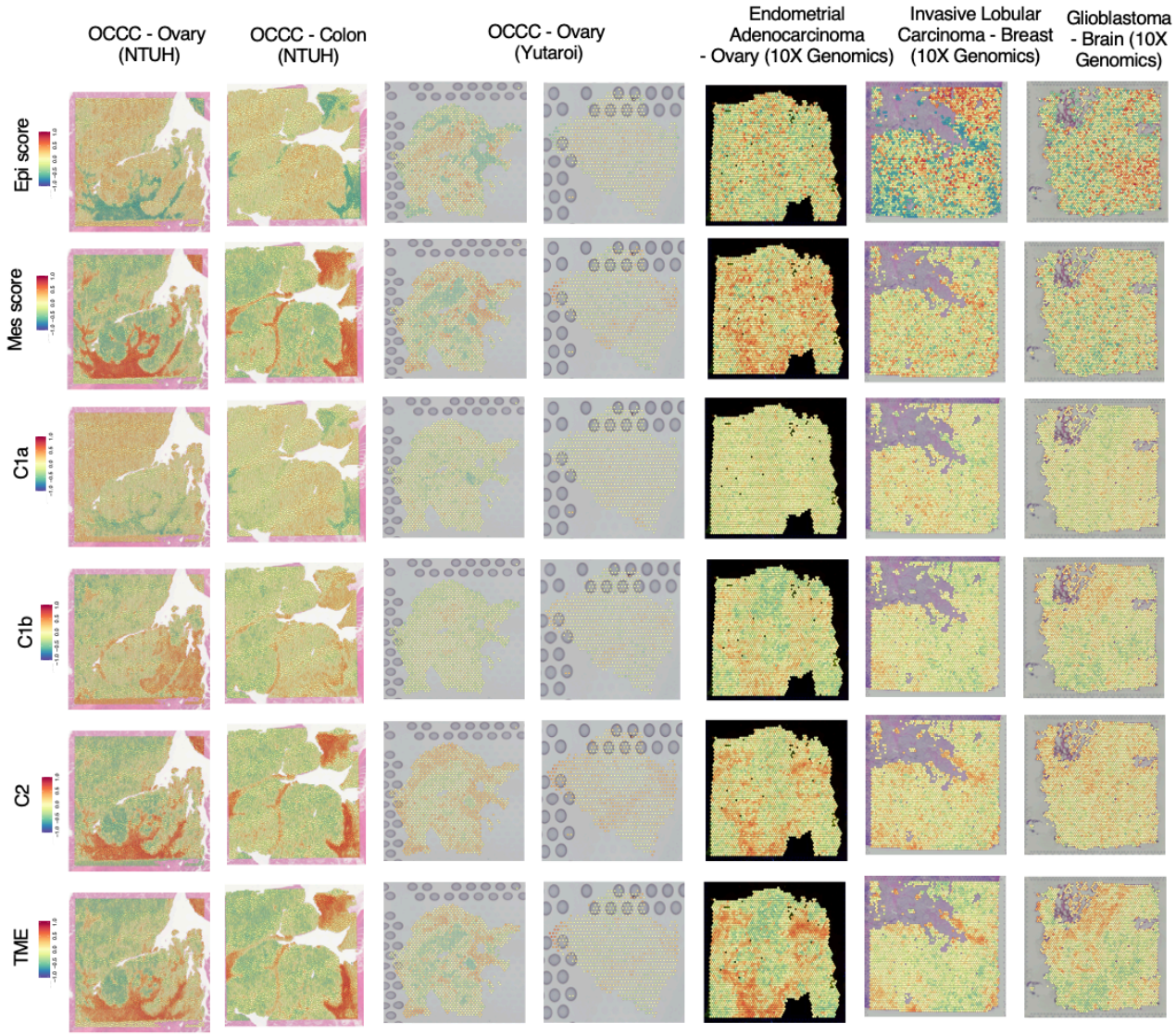
OCCC - Ovary (NTUH)
OCCC - Colon (NTUH)
OCCC - Ovary (Yutaroi)
Endometrial Adenocarcinoma - Ovary (10X Genomics)
Invasive Lobular Carcinoma - Breast (10X Genomics)
Glioblastoma - Brain (10X Genomics)
Epi score
Mes score
C1a
C1b
C2
TME

S. Fig. 6

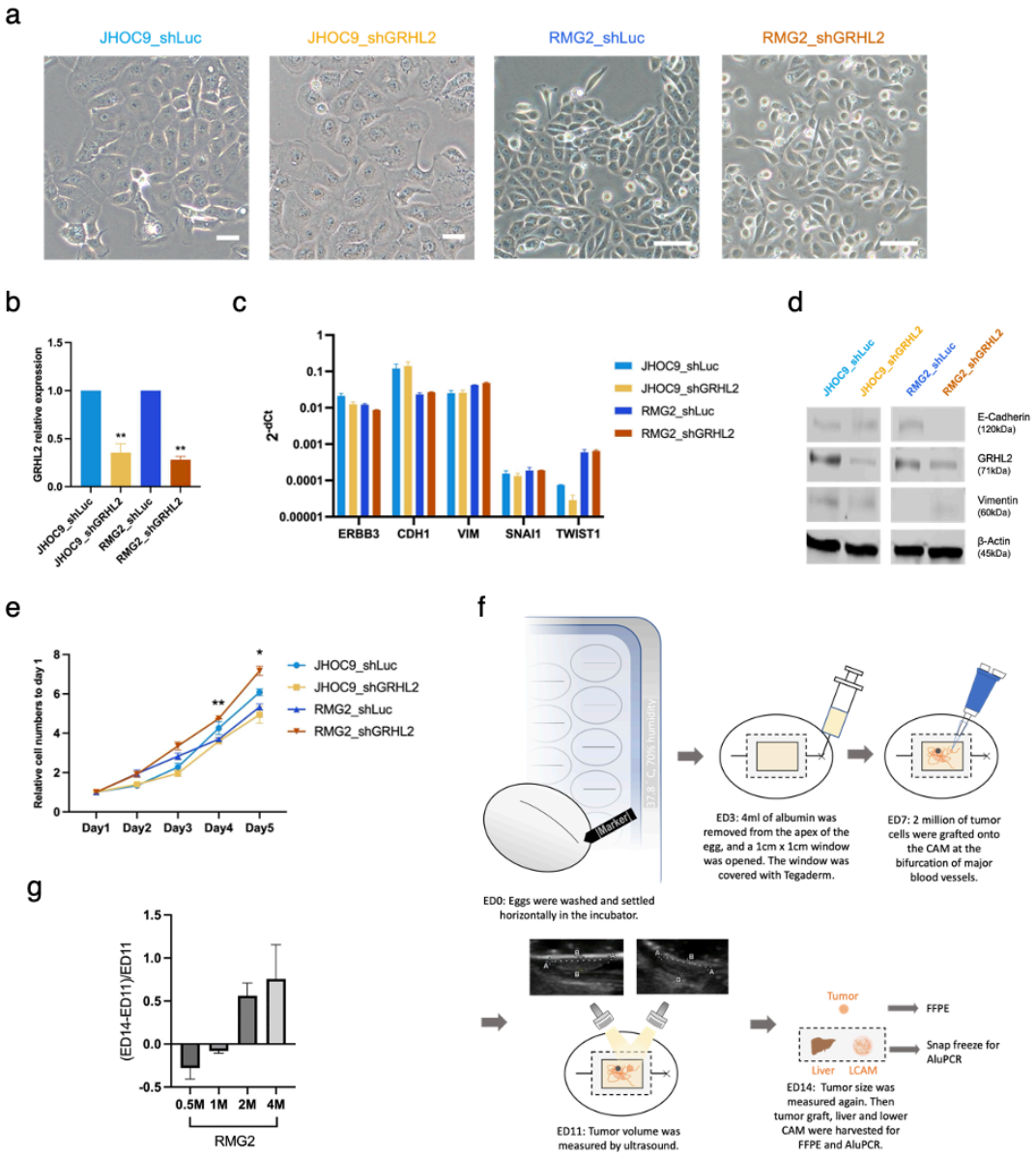
a
JHOC9_shLuc
JHOC9_shGRHL2
RMG2_shLuc
RMG2_shGRHL2
b
GRHL2 relative expression
1.5
1.0
0.5
0.0
**
**
JHOC9_shLuc
JHOC9_shGRHL2
RMG2_shLuc
RMG2_shGRHL2
c
2^-dCt
1
0.1
0.01
0.001
0.0001
0.00001
ERBB3
CDH1
VIM
SNAI1
TWIST1
JHOC9_shLuc
JHOC9_shGRHL2
RMG2_shLuc
RMG2_shGRHL2
d
JHOC9_shLuc
JHOC9_shGRHL2
RMG2_shLuc
RMG2_shGRHL2
E-Cadherin (120kDa)
GRHL2 (71kDa)
Vimentin (60kDa)
β-Actin (45kDa)
e
Relative cell numbers to day 1
8
6
4
2
0
**
*
Day1
Day2
Day3
Day4
Day5
JHOC9_shLuc
JHOC9_shGRHL2
RMG2_shLuc
RMG2_shGRHL2
f
Matrigel
ED0: Eggs were washed and settled horizontally in the incubator.
ED3: 4ml of albumin was removed from the apex of the egg, and a 1cm x 1cm window was opened. The window was covered with Tegaderm.
ED7: 2 million of tumor cells were grafted onto the CAM at the bifurcation of major blood vessels.
ED11: Tumor volume was measured by ultrasound.
Tumor
FFPE
Liver
LCAM
Snap freeze for AluPCR
ED14: Tumor size was measured again. Then tumor graft, liver and lower CAM were harvested for FFPE and AluPCR.
g
(ED14-ED11)/ED11
1.5
1.0
0.5
0.0
-0.5
0.5M
1M
2M
4M
RMG2

S. Fig. 7

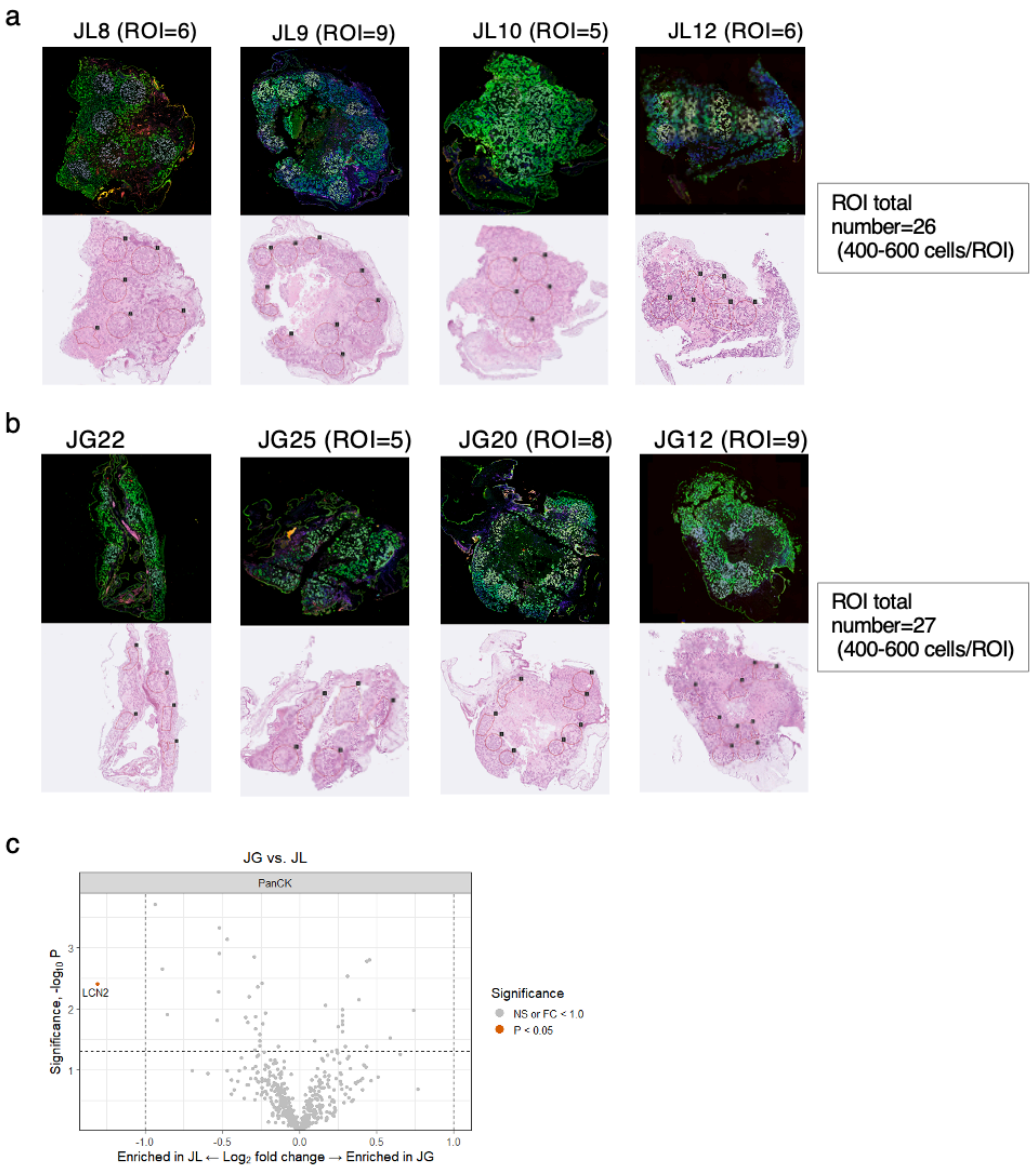
a
JL8 (ROI=6)
JL9 (ROI=9)
JL10 (ROI=5)
JL12 (ROI=6)
ROI total number=26 (400-600 cells/ROI)
b
JG22
JG25 (ROI=5)
JG20 (ROI=8)
JG12 (ROI=9)
ROI total number=27 (400-600 cells/ROI)
c
JG vs. JL
PanCK
LCN2
Significance, -log10 P
Enriched in JL ← Log2 fold change → Enriched in JG
Significance
NS or FC < 1.0
P < 0.05

S. Fig. 8

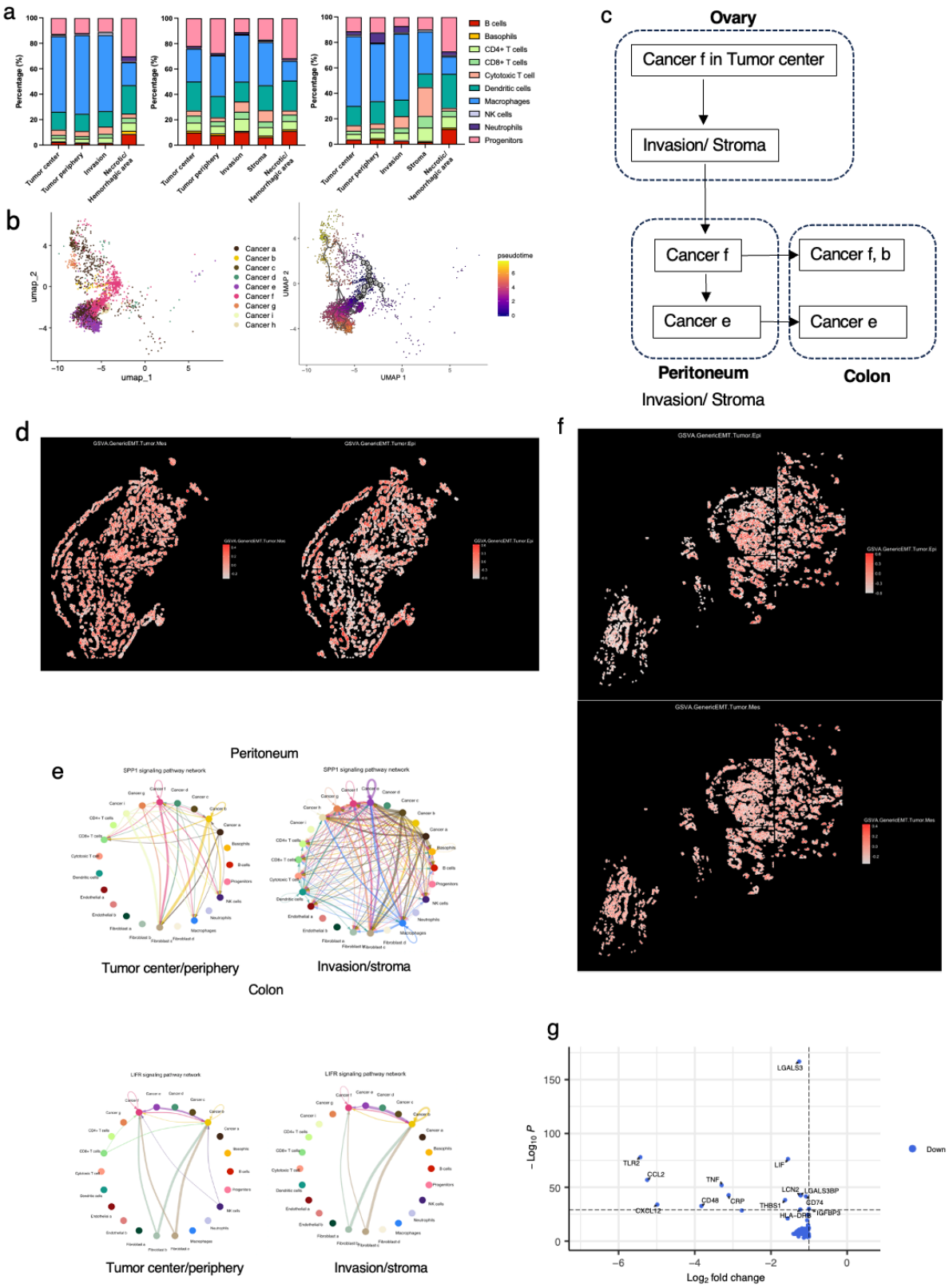
a
Percentage (%)
Tumor center
Tumor periphery
Invasion
Stroma
Necrotic/ Hemorrhagic area
B cells
Basophils
CD4+ T cells
CD8+ T cells
Cytotoxic T cell
Dendritic cells
Macrophages
NK cells
Neutrophils
Progenitors
b
umap_1
umap_2
Cancer a
Cancer b
Cancer c
Cancer d
Cancer e
Cancer f
Cancer g
Cancer i
Cancer h
UMAP 1
UMAP 2
pseudotime
c
Ovary
Cancer f in Tumor center
Invasion/ Stroma
Cancer f
Cancer e
Cancer f, b
Cancer e
Peritoneum
Colon
Invasion/ Stroma
d
GSVA.GenericEMT.Tumor.Mes
GSVA.GenericEMT.Tumor.Epi
f
GSVA.GenericEMT.Tumor.Epi
GSVA.GenericEMT.Tumor.Mes
e
Peritoneum
SPP1 signaling pathway network
Tumor center/periphery
Invasion/stroma
Colon
LIFR signaling pathway network
Tumor center/periphery
Invasion/stroma
g
LGALS3
TLR2
CCL2
LIF
TNF
CD48
CRP
CXCL12
LCN2
LGALS3BP
CD74
THBS1
HLA-DRB
IGFBP3
Down
$-\mathrm{Log}_{10}\,P$
Log_2 fold change